

INAUGURAL - DISSERTATION  
zur  
Erlangung der Doktorwürde  
der  
Naturwissenschaftlich-Mathematischen Gesamtfakultät  
der  
Ruprecht-Karls-Universität  
Heidelberg

vorgelegt von  
Dipl.-Math. Carmen R. Ellsäßer  
aus Heidelberg

Tag der mündlichen Prüfung: 30.10.2008



# SIMULATIONS OF A NEURON NETWORK MODEL IN THE OLFACTORY SYSTEM

1. Gutachter: Prof. Dr. Dr. h.c. mult. Willi Jäger
2. Gutachter: Prof. Dr. Peter Bastian





# ABSTRACT

In this work a model for the neuron network in the olfactory bulb is developed. The model includes mitral and granule cells, modeled as point neurons with integrate-and-fire dynamics. The activity of the network model is simulated and numerically analyzed using so-called equation-free techniques. These techniques allow to investigate the macroscopic, coarse behavior of high dimensional systems without deriving closed low-dimensional equations. The equation-free simulation tools are adapted to the needs of investigating the coarse behavior of the olfactory bulb network model here: equation-free Newton's method, parameter studies and methods for traveling waves are introduced. By interpreting the equation-free time-stepping scheme as an one-step method it is proven that the numerical solution converges to the analytical solution as the length of the time step tends to zero.

Point neurons are sometimes not sufficient, i.e. the spatial expansion of a neuron has to be considered to compare simulation results to results of imaging experiments. To simulate the spatiotemporal activity of neurons we consider a finite-element approach based on the Hodgkin-Huxley mechanism using adaptive grid control in space and time. For the adaptive grid control a-posteriori error estimators are developed for passive signal propagation equations using a standard duality based approach.

The presented simulation and analysis tools allow to investigate interesting biological questions. Namely, how the time course of neuron dynamics and inhibitory activity influences the dynamics of the neurons in the olfactory bulb. Using equation-free simulations for the point neuron model the influence of network connectivity parameters on lateral inhibition and contrast enhancement properties of the network are investigated. For odor discrimination tasks experimental results are reproduced and long-term investigations show hysteresis effects, which stabilize the network output with regard to small changes in the input. For these investigations the equation-free approach is combined with numerical bifurcation analysis techniques. Finally, it is possible to determine when traveling waves occur in the network and we are able to give explanations why traveling waves are only seen in teleosts like zebrafish, not in mammals by using equation-free methods for traveling waves on an discrete point neuron model.



# ZUSAMMENFASSUNG

In dieser Arbeit wird ein Modell für das Neuronennetzwerk im olfaktorischen Bulbus entwickelt. Das Modell beinhaltet Mitral- und Körnerzellen, die als Punktneuronen mit “Integrate-and-Fire” Dynamik modelliert werden. Die Aktivität des Netzwerkmodells wird mit so genannten “Equation-free” Techniken simuliert und numerisch analysiert. “Equation-free” Techniken sind Simulationswerkzeuge um das *coarse* Verhalten von hochdimensionalen Systemen zu untersuchen, ohne dafür geschlossene niederdimensionale Gleichungen herleiten zu müssen. Diese Techniken werden für die Untersuchung des Netzwerkmodells vom olfaktorischen Bulbus weiterentwickelt: “Equation-free” Newton Verfahren, Parameterstudien und Methoden zur Untersuchung von Traveling Waves werden eingeführt. Indem das “Equation-free” Zeitschrittverfahren als Einschrittverfahren interpretiert wird, ist es möglich ein Konvergenztheorem zu beweisen.

Punktneuronen sind u.U. nicht ausreichend wenn z.B. Simulationsergebnisse mit Imagingexperimenten verglichen werden sollen. Hier muss die räumliche Ausdehnung der Neuronen berücksichtigt werden. Um die Aktivität einzelner Neuronen zu simulieren wird ein Finite-Elemente Ansatz basierend auf dem Hodgkin-Huxley Mechanismus beschrieben. Bei diesem Ansatz wird adaptive Gittersteuerung in Ort und Zeit benutzt. Dafür werden a-posteriori Fehlerschätzer für passive Signalausbreitung in Nervenzellen entwickelt.

Die hier präsentierten Simulations- und Analysewerkzeuge ermöglichen es interessante biologische Fragestellungen zu untersuchen. Der Einfluß des zeitlichen Ablaufs von Neuronendynamik und inhibitorischer Aktivität auf die Nervenzelldynamik im olfaktorischen Bulbus werden untersucht. Mittels der “Equation-free” Simulationsmethodik für das Punktneuronenmodell kann der Einfluß von Netzwerkparametern auf die laterale Inhibition und auf Kontrastverstärkungsverhalten untersucht werden. Für Geruchsunterscheidungsaufgaben können experimentelle Ergebnisse reproduziert und Langzeituntersuchungen durchgeführt werden. Letztere zeigen Hystereseeffekte, die zu einer Stabilisierung des Netzwerkoutputs für kleine Inputstörungen führen. Für diese Untersuchung wird der “Equation-free” Ansatz mit Techniken der numerischen Bifurkationsanalyse kombiniert. Schließlich kann angegeben werden, wann Traveling Waves im diskreten Netzwerkmodell entstehen, und es ist möglich eine Erklärung zu geben, warum Wellen in Experimenten mit Knochenfischen entstehen, nicht aber bei Experimenten mit Säugetieren.



# ACKNOWLEDGMENTS

First of all, I would like to express my gratitude to Prof. Willi Jäger for his willingness to supervise this research project and for his constant support and encouragement. Furthermore, I would like to thank Prof. Peter Bastian for his confidence and ongoing support as second supervisor of this thesis.

Without the financial support of the German Research Foundation (DFG) through the International Graduiertenkolleg 710 “Complex processes: Modeling, Simulation and Optimization” this thesis would not have been possible.

I want to thank Prof. Jens Starke for pointing my research interest towards the olfactory system and his support throughout this thesis. Many thanks go to Dr. Olaf Ippisch and Dr. Stefan Lang for fruitful discussions concerning the simulations of neurons with spatial expansion.

I am deeply indebted to Prof. Jens Midtgaard for explaining biology to a mathematician. Many thanks go to Prof. Thomas Kuner for suggesting odor discrimination tasks as interesting biological questions for simulations. Martin Wiechert helped me a lot to get first insides to the biology of the olfactory system, thanks for that. Thanks goes to Prof. Yannis Kevrekidis who introduced me to the concept of equation-free simulation techniques.

I thank Dr. Igor Doktorski, Dr. Franziska Matthäus, Dr. Annika Wedemeier and Dr. Frederic Weller for proofreading this thesis. (Of course they are not responsible for the remaining mistakes.)

Thanks goes to all my colleagues from AMJ for friendly and encouraging atmosphere at the institute. Many thanks go to the members of the Simulation of Large Systems Department at the University of Stuttgart for a warm welcome during a research stay in their group. A special thanks to Christian Engwer and Sreejith Pulloor Kuttanikkad who answered my numerous questions concerning DUNE and therefore helped me a lot. I would like to thank the members of IGK 710 for the discussions and support – scientific and non-scientific.

Vielen Dank an Patricia Rusu und Susanne Till für anhaltende interdisziplinäre Kommunikation und Unterstützung. Holger Faust danke ich für's Dasein und dafür, dass er mich gelegentlich ins wirkliche Leben zurück geholt hat. Besonderer Dank geht an meine Familie, vor allem an meine Eltern, die mich während meines Studiums und der Promotionszeit immer unterstützt haben.



*Wer nicht traurig sein kann  
hat im Leben nicht getanzt.*  
H. GRÖNEMEYER





# Contents

<b>1</b>	<b>INTRODUCTION</b>	<b>1</b>
<b>2</b>	<b>THE NEURON NETWORK OF THE OLFATORY BULB</b>	<b>7</b>
2.1	THE OLFATORY SYSTEM . . . . .	7
2.2	MAIN BUILDING BLOCKS OF THE OLFATORY BULB NETWORK . . . . .	9
2.2.1	CELL TYPES INCLUDED IN THE MODEL . . . . .	9
2.2.2	MORPHOLOGY OF MITRAL CELLS . . . . .	11
2.2.3	MORPHOLOGY OF GRANULE CELLS . . . . .	11
2.2.4	PASSIVE PROPERTIES OF THE MITRAL AND GRANULE CELLS . . .	11
2.3	THE MITRAL-GRANULE CELL NETWORK . . . . .	12
2.3.1	SYNAPSES . . . . .	13
2.3.2	NETWORK INPUT AND OUTPUT . . . . .	14
2.4	NEURON DYNAMICS . . . . .	14
2.4.1	SPIKE RESPONSE MODEL . . . . .	15
2.4.2	HODGKIN-HUXLEY MODEL . . . . .	16
2.5	OLFATORY BULB NETWORK MODEL . . . . .	18
2.6	ABILITIES OF THE NETWORK . . . . .	20
2.6.1	LATERAL INHIBITION AND CONTRAST ENHANCEMENT . . . . .	20
2.6.2	ODOR DISCRIMINATION . . . . .	20
2.6.3	TRAVELING WAVES . . . . .	21
2.7	EARLIER SIMULATION APPROACHES . . . . .	21
2.8	CONCLUSIONS OF CHAPTER 2 . . . . .	22
<b>3</b>	<b>ADAPTIVE COMPUTATIONS FOR BRANCHED NERVE EQUATIONS</b>	<b>23</b>
3.1	PASSIVE SIGNAL PROPAGATION FOR NEURONS . . . . .	24
3.2	FINITE-ELEMENT DISCRETIZATION ON NON-EQUIDISTANT GRIDS . . . . .	26
3.3	LOCAL GRID REFINEMENT . . . . .	27
3.4	A-POSTERIORI ESTIMATES & ADAPTIVE GRID CONTROL . . . . .	28
3.4.1	SPATIAL GRID CONTROL . . . . .	29
3.4.2	TIME STEP SIZE CONTROL . . . . .	33

3.5	CONCLUSIONS OF CHAPTER 3	33
<b>4</b>	<b>EQUATION-FREE SIMULATIONS: INTRODUCTION AND THEORY</b>	<b>37</b>
4.1	BASIC DEFINITIONS	38
4.2	OVERVIEW OF EXISTING METHODS	40
4.3	EQUATION-FREE SIMULATIONS IN TIME	41
4.3.1	COARSE TIME-STEPPER	42
4.3.2	COARSE PROJECTIVE INTEGRATION	43
4.4	CONVERGENCE OF EQUATION-FREE SIMULATIONS	44
4.5	EQUATION-FREE NEWTON'S METHOD	49
4.6	DEPENDENCIES ON INDEPENDENT PARAMETERS	50
4.7	EQUATION-FREE METHODS FOR TRAVELING WAVES	51
4.7.1	TRAVELING WAVE VARIABLE	52
4.7.2	EQUATION-FREE TEMPLATE FITTING	53
4.8	NUMERICAL BIFURCATION ANALYSIS	54
4.8.1	SADDLE-NODE BIFURCATION	55
4.8.2	HYSTERESIS	57
4.8.3	CUSP BIFURCATION	58
4.8.4	PSEUDO-ARCLENGTH CONTINUATION	59
4.9	CONCLUSIONS OF CHAPTER 4	60
<b>5</b>	<b>ADAPTIVE COMPUTATIONS FOR MITRAL CELLS</b>	<b>63</b>
5.1	ADAPTIVE COMPUTATION IN SPACE	64
5.2	TIME STEP SIZE CONTROL	66
5.3	INFLUENCE OF INHIBITORY SYNAPSES	67
5.4	CONCLUSIONS OF CHAPTER 5	69
<b>6</b>	<b>LATERAL INHIBITION AND CONTRAST ENHANCEMENT</b>	<b>71</b>
6.1	EQUATION-FREE SIMULATION OF SPIKING DYNAMICS	71
6.1.1	LIMITS OF THE EQUATION-FREE TECHNIQUE	75
6.2	LATERAL INHIBITION	77
6.3	CONTRAST ENHANCEMENT	78
6.3.1	EQUATION-FREE INVESTIGATIONS OF CONTRAST ENHANCEMENT	79
6.4	CONCLUSIONS OF CHAPTER 6	81
<b>7</b>	<b>ODOR DISCRIMINATION</b>	<b>83</b>
7.1	DISCRIMINATION TIME	84
7.2	EQUATION-FREE CONTINUATION OF SPIKING RATE DIFFERENCES	89
7.3	BIOLOGICAL INTERPRETATION	92
7.4	CONCLUSIONS OF CHAPTER 7	92

<b>8 TRAVELING WAVES</b>	<b>95</b>
8.1 INFLUENCE OF BOUNDARIES . . . . .	96
8.2 INFLUENCE OF NETWORK PARAMETERS . . . . .	97
8.2.1 EQUATION-FREE INVESTIGATION OF TRAVELING WAVES . . . . .	98
8.2.2 BIOLOGICAL INTERPRETATION . . . . .	100
8.3 CONCLUSIONS OF CHAPTER 8 . . . . .	101
<b>9 CONCLUSIONS AND OUTLOOK</b>	<b>103</b>
<b>A LIST OF SYMBOLS &amp; PARAMETERS</b>	<b>107</b>
A.1 PARAMETERS USED IN ADAPTIVE SIMULATIONS . . . . .	109
A.2 PARAMETERS USED IN EQUATION-FREE SIMULATIONS . . . . .	109
<b>C LIST OF FIGURES</b>	<b>110</b>
<b>D BIBLIOGRAPHY</b>	<b>112</b>



# Chapter 1

## INTRODUCTION

*There is no certainty in science where not one  
of the mathematical sciences can be applied.*

LEONARDO DA VINCI

Sensory systems, i.e. the part of the nervous system responsible for processing sensory information, consist of receptors, neural pathways and the parts of the brain involved in sensory perception [84]. In the commonly recognized sensory systems like vision, hearing, somatic sensation, taste, and olfaction the sensory pathways underlie several main principles. Receptors detect the stimuli in terms of type or location, intensity, and duration. After the detection of the stimuli, the information is processed in networks of neurons which detect, discriminate, and convert large numbers of different inputs. In the human olfactory system, for example, there are about 200 to 350 different types of olfactory receptors but we are able to smell between 4,000 and 10,000 different odors [59]. One of the main principles in all sensory systems is to minimize the number of needed receptors, while still being able to detect all stimuli that will be present during the life time of an organism. The common way of achieving this is to apply a quite small number of receptors and use downstream neural mechanisms to process the incoming signal. For instance, contrast enhancement is considered as a general property of all sensory systems [112, 124]. This results in the ability to discriminate inputs that are close together in input space [55], see Figure 1.1.

As an example for sensory processing the olfactory system is considered in this work. On one hand, it is recognized as being an important model system for brain function [102, 106]. On the other hand, olfaction is of central importance for most species, as was pointed out by the Nobel Assembly when the Nobel Prize in Physiology or Medicine was awarded to Richard Axel and Linda Buck in 2004 for their discoveries of “odor receptors and the organization of the olfactory system” [20].

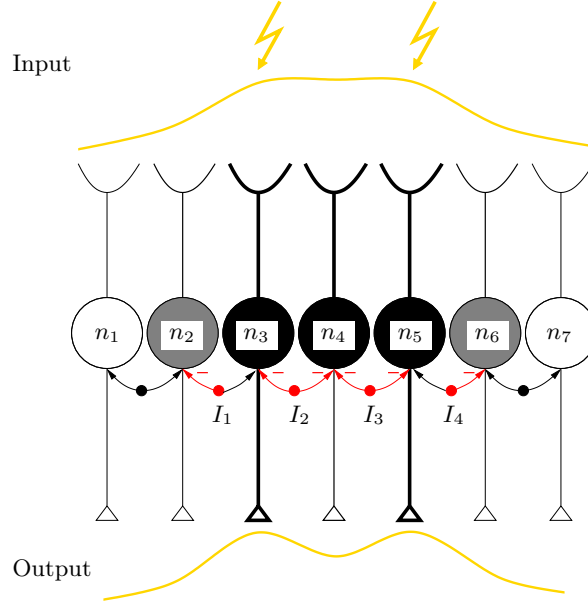


Figure 1.1: *Inhibition in a network of neurons causes contrast enhancement: a typical effect in sensory systems. Neurons  $n_3$ ,  $n_4$  and  $n_5$  are strongly excited (dark grey), neurons  $n_2$  and  $n_6$  are weakly excited (light grey) from the input profile, which represents input from two nearby stimuli. For simplicity, it is assumed that only strong excitation mediates inhibition (red arrows). Neuron  $n_2$  and  $n_6$  are inhibited by  $I_1$  and  $I_4$ ;  $n_4$  is inhibited by  $I_2$  and  $I_3$ , while  $n_3$  and  $n_5$  are only inhibited by  $I_2$  or  $I_3$ . This leads to a sharpened output profile.*

As a model system the olfactory system is attractive due to the easy control of the sensory input, the experimental accessibility in animal studies and the relatively well defined input for the network of neurons responsible for processing the sensory information. In recent years a large body of experimental data has been accumulated for species ranging from insects to humans. These point to some similarities in olfactory signal processing [44, 45, 68]. The neuron network responsible for signal processing in olfaction is located in the so-called olfactory bulb. The olfactory bulb network consists of several different types of neurons that convey olfactory information to higher order olfactory structures and to other brain systems. The activity is introduced to the network from receptor neurons and results in spatiotemporal structures uniquely determined for each odor. Also much is known about the dynamics of the olfactory bulb network, less is known about its connectivity properties. Hence, the modeling, simulation and analysis of the dynamics of such networks with respect to changing connectivity parameters is the main aim of this work.

To get a deeper understanding of the biological phenomena involved in sensory processing we develop a mathematical model of the olfactory bulb neuron network, and use

sophisticated simulation and analysis techniques to investigate its behavior. Early works of Freeman [43] suggested that the spatiotemporal activity patterns of the olfactory bulb can be interpreted within the framework of dynamical systems theory. It turns out that this is indeed possible by using equation-free methods, such as developed in [48, 61, 62]. These techniques allow to analyze the coarse behavior of systems described on a microscopic, fine level, without deriving closed equations for the macroscopic dynamic. An example for this situation is the model of the neuron network in the olfactory bulb. The microscopic equations are for example a discretization of coupled Hodgkin-Huxley equations or an integrate-and-fire network of point neurons. Principal and independent component analysis of calcium-sensitive dye imaging experiments in the olfactory bulb of rats show that the network activity can be described with a small number of variables [95]. We show that coarse descriptions of the network dynamics are possible by interpreting the PCA/ICA variables as coarse quantities.

**T**his work consists of three main theoretical parts. First, we develop a model of the neuron network involved in sensory processing in the olfactory pathway. Based on published biological data we introduce a model with point neurons. For their dynamics we use the so-called Spike Response model, an integrate-and-fire model with refractoriness and external input. This approach allows to simulate and analyze relatively large neuron networks. We implement the model using the high-level programming language MATLAB [114].

Admittedly, point neurons are not sufficient for all applications. Therefore, we show in the second main part of this work a possibility to perform simulations of neuron dynamics for neurons where the spatial expansion is taken into account. We introduce error based adaptive grid control in space and time for these applications. To be able to apply adaptive grid control, we develop a-posteriori error estimators for the dynamics of branched nerve equations using standard energy estimates.

The third part addresses so-called equation-free simulation and analysis techniques which enables us to apply numerical bifurcation analysis for the olfactory network model. We show, to our knowledge for the first time, under which conditions the equation-free time-stepping is convergent and introduce several generalizations which are necessary for the application in investigations of network models, i.e. equation-free Newton's method, parameter studies and equation-free methods for investigating the dynamics of traveling waves. "Equation-free" maybe a misleading term: it does not mean that no model equations are involved in the simulations. It means, that model equations are available on a fine, microscopic level. These equations in general are formulated in a high dimensional space. One assumes that the dynamics of the whole system is described only by coarse macroscopic variables in a low dimensional space. Instead of deriving closed equations on this low-dimensional space, one only evaluates the coarse variables numerically. This motivates

the term “equation-free” simulation tools as it was introduced from I.G. Kevrekidis and coworkers [62].

These three parts are finally brought together for simulations and numerical analysis of the behavior of single cells and the whole network. First, we look at single cells with spatial expansion and investigate the influence of synaptic activity on the dynamics of the cell. Second, we investigate a network of point neurons: we validate our network model by comparing it to known results in the context of lateral inhibition, odor discrimination and traveling waves. By investigating the time course of the network dynamics by using results from PCA/ICA of experimental data, we can, on one hand, show that equation-free computations are reasonably applicable to simulate and analyze the behavior of our neuron network model of the olfactory bulb network. On the other hand, we can use this setting to show the limits of the equation-free method.

The equation-free method allows to perform parameter studies, i.e. we are able to investigate how the connection parameters of the olfactory bulb network influence its dynamics. In simulations of lateral inhibition and contrast enhancement it turns out, that the parameter with the most influence is the so-called radius of interaction. It describes how large the spatial distance between two neurons can be in order to still form connections. In the context of odor discrimination we perform a numerical bifurcation analysis of the system. We are able to detect hysteresis and adaptation processes. For traveling waves we can give a hypothesis why they are only detected experimentally in the olfactory system of zebrafish but not in mammals.

**A**s the main results of this work we can highlight the following points:

- We perform successful parameter studies of the network dynamics in the olfactory bulb using a network model with a large number of neurons and realistic network parameters.
- Numerical solutions of the model reflect experimental results.
- Additionally, we are able to give explanations for biological results, i.e. for traveling waves simulated on a grid model of point neurons, which could not be found in experiments yet.

These points are achieved by combining biological knowledge and mathematical modeling to simulations and numerical analysis.



We conclude this introduction with short summaries of each chapter of this thesis.

## CHAPTER 2: THE NEURON NETWORK OF THE OLFACTORY BULB

In this chapter we give the biological background of the neuron network of the olfactory bulb (OB) underlying our network model. With this knowledge we are able to state a model of point neurons with Spike Response model (SRM) dynamics. In addition, a model for neuron dynamics based on the Hodgkin-Huxley equations coupled to the cable equation is introduced in order to simulate the behavior of single cells of the OB network as their spatial expansion is taken into account. This chapter ends with a description of the abilities of the network and a summary of earlier simulation approaches as they can be found in the literature.

## CHAPTER 3: ADAPTIVE COMPUTATIONS FOR NERVE EQUATIONS

To get realistic insights into the dynamics of neurons by simulations, it might be not sufficient to consider networks of point neurons. In the frame-work of finite-element methods one is able to simulate the dynamics of neurons with spatial expansion based on the Hodgkin-Huxley model. In this context, we introduce error based control for adaptive grids in space and time. Error estimators used for this approach are developed here.

## CHAPTER 4: EQUATION-FREE SIMULATIONS: INTRODUCTION & THEORY

In order to not only simulate but also analyze the behavior of neuron networks with respect to changes in the connection parameters we apply equation-free simulation techniques. In Chapter 4, we adapt them to the needs of the analysis of the OB network behavior and give an overview of the literature available in this field. Additionally, we interpret the equation-free methods as one-step methods and prove a convergence theorem.

## CHAPTER 5: ADAPTIVE COMPUTATIONS FOR MITRAL CELLS

This chapter is devoted to the simulation of a single mitral cell with spatial expansion using adaptive computations. First, we investigate the performance properties of the adaptive methods introduced in Chapter 3. Second, we look how synapses on the secondary dendrites of mitral cells, one of the main cell types in the OB, influence the signal processing in the cells.

## CHAPTER 6: LATERAL INHIBITION AND CONTRAST ENHANCEMENT

We use the equation-free methods developed in Chapter 4 to simulate the SRM network of the OB introduced in Chapter 2. First we test these approach with regard to

its performance properties for simulating the time course of the spiking dynamics of the olfactory bulb network model. Then we validate our SRM-network of the OB by showing that it reproduces experimental results of lateral inhibition qualitatively. We investigate how these properties are influenced by the connection parameters in the network. Finally, we investigate contrast enhancement properties of the network with equation-free analysis techniques.

## CHAPTER 7: ODOR DISCRIMINATION

In this chapter we investigate the ability of the network model to distinguish binary mixtures of odors, depending on the ratio of the mixtures. It turns out that experimental results can be reproduced qualitatively. Furthermore, we can predict different discrimination abilities depending on the connection parameters. We see that hysteresis and adaptation effects occur in the network in the case of systems where the stimulus, i.e. the input, changes during the long-term simulations.

## CHAPTER 8: TRAVELING WAVES

In experiments with zebrafish, one can find traveling-wave-like dynamics of the olfactory bulb neuron network. We investigate in this chapter under which conditions traveling waves emerge in our point neuron network model and how their appearance is influenced by the structure and the connectivity of the network. It turns out that, on one hand, the shape of the boundaries of the network has influence on the shape of the waves. On the other hand, we can show that the radius of interaction is the main parameter which influences the traveling waves. Biological interpretation of these results conclude this chapter.

## CHAPTER 9: CONCLUSIONS AND OUTLOOK

We close this thesis with drawing the main conclusions with regard to our findings, on one hand, for the used simulation and analysis techniques, and on the other hand we interpret, where it is possible, our results biologically and suggest new experimental settings where they could be tested.

## Chapter 2

# THE NEURON NETWORK OF THE OLFACTORY BULB

*Smell is a potent wizard that  
transports you across thousand of miles  
and all the years you have lived.*

HELEN KELLER

In this chapter we give the basic biological facts of the neuron network of the olfactory bulb (OB), underlying our model for the mitral and granule cell network: a model of point neurons with Spike Response dynamics. In addition, neuron dynamics modeled by the Hodgkin-Huxley equations coupled to the cable equation is introduced in order to simulate the behavior of single cells of the OB network. This chapter ends with a description of the abilities of the OB network and a summary of earlier simulation approaches as they can be found in the literature.

---

### 2.1 THE OLFACTORY SYSTEM

In the last two decades the olfactory system, and especially the network of neurons in the olfactory bulb (see Figure 2.1), has become a model neuronal system. It is worth investigating not only for its unique interests but also for the general principles and shared mechanisms that may lead to a deeper understanding of the main principles of brain functions [106]. The olfactory system is an attractive model system from the biological point of view, due to its easy control of the sensory input and the experimental accessibility

in animal studies. From the view point of a modeler, it is interesting because of the relatively small number of neurons in the network and the relatively well defined input for the network. Less is known about the network connectivity in the olfactory bulb network, and modeling and simulation can help to make predictions. Hence, it is interesting to investigate the olfactory system with interdisciplinary approaches connecting biological knowledge and mathematical modeling, simulation, and analysis techniques to get a deeper understanding of its functionality.

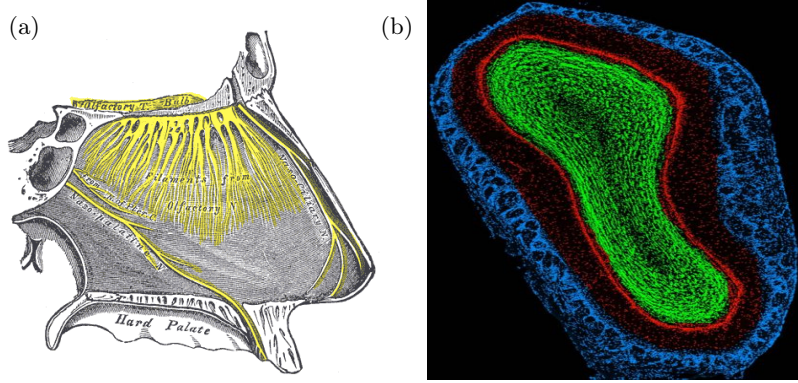


Figure 2.1: *The olfactory bulb (OB). (a) Nerves of the septum of the human nose, right side. The olfactory bulb is visible at the upper left. Reproduction of a lithograph plate from the 20th U.S. edition of Gray's Anatomy of the Human Body, originally published in 1918 [53]. (b) A coronal section through the main olfactory bulb of an adult male mouse [120]. The colors indicate the three main anatomical layers: blue - glomerular layer, red - external plexiform layer and mitral cell layer, green - internal plexiform and granule cell layer. The scale of this picture is ventral to dorsal about 2mm.*

In the olfactory system, see Figure 2.1 (a), odor molecules are transduced by the olfactory receptor neurons (ORNs), which are first-order neurons located in the olfactory epithelium within the nasal cavity [112]. There are between 70 different types of ORNs in zebrafish [8] and 200-350 different types in mammals [86], where every type is able to detect a certain type of odor molecules [40]. A mathematical model for the calcium oscillations in the cilia of ORNs was developed in [94]. The different types of ORNs are distributed unsorted across the olfactory epithelium. ORN axons form the olfactory nerve and synaptically terminate in the olfactory bulb (OB). The region where these axons project is called the glomerular layer of the OB. Axons from the same receptor type converge into the same glomerulus [106]. That means a sorting process takes place during the axonal growth from the epithelium to the OB. This process was modeled and analyzed in [57]. In the olfactory bulb itself one finds a network of several different types of neurons that conveys olfactory information to higher order olfactory structures and to other brain systems, see Figure 2.1 (b). The activity introduced to the network by the glomeruli results in spa-

tiotemporal structures uniquely determined for each odor. The modeling, simulation and analysis of the dynamics of this network is the main aim of this work. We will describe the morphology of the OB network in detail in the next sections.

**I**n this chapter we introduce a biologically detailed model of the olfactory bulb. In Section 2.2 the main building blocks of the network are introduced and their connection properties are stated in Section 2.3. Section 2.4 gives an overview about models for the neuron dynamics, including the classical Hodgkin-Huxley model and an integrate-and-fire model: the Spike Response model. Section 2.5 gives the main results of this chapter: we introduce our model for the neuron network of the olfactory bulb. In Section 2.6 we give an overview about the abilities of the neuron network, including contrast enhancement, odor discrimination and its capability to generate traveling waves. We conclude this chapter with an overview over earlier simulation approaches for the neuron network in the olfactory bulb in Section 2.7.

## 2.2 MAIN BUILDING BLOCKS OF THE OLFACTORY BULB NETWORK

**I**n this section we describe the main building blocks of the neuron network in the olfactory bulb (OB). The given data, if not mentioned otherwise, are taken from rats. The olfactory bulb has a characteristic laminar organization. The major neuron types in the OB are mitral cells (MCs), tufted cells, periglomerular (PG) cells, granule cells (GCs), and short-axon cells. These cells are arranged in layers [90, 107], see Figure 2.2. The first layer is the glomerular layer (GL), where mainly PG cells and some short axon cells occur. The input from the ORNs is given to the network here. The axons of the ORNs converge into glomeruli and form synaptic connections to the mitral cells. The next layer is the external plexiform layer (EPL) where one finds the tufted cells. In the following mitral cell layer (MCL) the somata of the mitral cells are located and some granule cells can be found here, too. But the layer where most of the granule cells are found is the granule cell layer (GCL). The internal plexiform layer (IPL) is located in between the MCL and the GCL, separating these two layers.

### 2.2.1 CELL TYPES INCLUDED IN THE MODEL

**W**e will see that the mitral and granule cells are the fundamental building blocks of the OB network. We can neglect the short-axon cells because they are presented in small numbers compared with other cell types. That means their role may be small and it is almost nothing known about their physiology [30]. The PG cells are involved in lateral

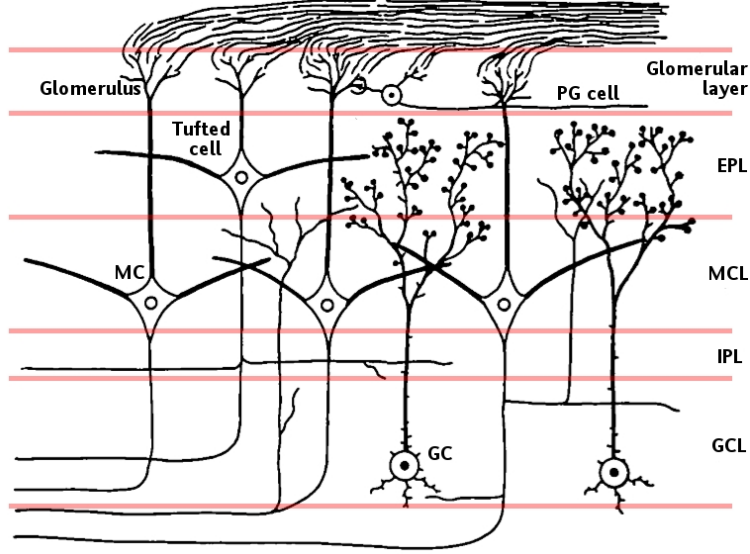


Figure 2.2: *Scheme of the olfactory bulb network, formed by mitral cells (MCs), tufted cells, periglomerular (PG) cells, and granule cells (GCs). These are arranged in layers, from top to bottom: glomerular layer (GL), where the axons of the ORNs converge into glomeruli and form synaptic connections to the mitral cells, the external plexiform layer (EPL), and the mitral cell layer (MCL). The last two layers are the internal plexiform layer (IPL) and the granule cell layer (GCL). This scheme is based on a figure from [90].*

inhibition at the level of the glomeruli [59]. Less is known about their physiology than about mitral and granule cells. In evolutionary terms PG cells appeared late, i.e. they are not presented at all in fish and are most numerous in mammals [35]. This suggests that PG cells provide a refinement of the bulb's fundamental computations which are supposed to be performed by the mitral, tufted and granule cells. Hence, we do not include them in our model.

Mitral and tufted cells are both output neurons of the bulb. The main differences are in size, orthodromic response properties, axonal projection patterns to central olfactory areas, distribution of secondary dendrites, and local axon collaterals. The differences in distribution of secondary dendrites, together with the different dendrite branching patterns of granule cell subtypes cause less communication between mitral and tufted cell populations than within them. This yields differences in axonal projection patterns and hence a functional separation of mitral and tufted cell populations [30]. Therefore, it can be assumed that tufted cells do not have to be modeled explicitly to gain basic insights into the olfactory bulb functions [82]. Hence, the cell types included in our model are mitral and granule cells.

### 2.2.2 MORPHOLOGY OF MITRAL CELLS

Based on the descriptions found in the literature we give the main properties of mitral cells in this subsection. For an overview, a schematic picture of a mitral cell is shown in Figure 2.3 (a). The somata of the cells have a transversal diameter of about  $20\mu m$  and a vertical diameter of about  $30\mu m$  [106]. The cell somata lie in the mitral cell layer of the olfactory bulb. They have primary and secondary dendrites and an axon [89]. The primary dendrites extend more or less radially across the plexiform layer and enter the glomerular formations in the superficial layer of the OB [35]. In the glomerular formation they branch repeatedly. The distance from the origin of the cell bodies to the point where they enter the glomerulie is about  $200\mu m$  to  $300\mu m$  [106]. The five to seven secondary dendrites pass obliquely through the external plexiform layer, becoming more closely parallel to the layer of mitral cells. These dendrites branch occasionally and can be seen to become thinner. They have a length between  $500\mu m$  and  $1000\mu m$  [89] with a diameter of  $1\mu m$  to  $6\mu m$  [106]. In mammals the length of these dendrites comes up to 25% to 33% of the bulb's circumference [107]. The axon of the mitral cells consists of the axon hill and the mitral segment with a length of about  $15 - 20\mu m$ . Then it suddenly narrows and becomes myelinated.

In Chapter 5 we will focus on the simulation of the dynamics of single mitral cells. The mitral cells form synapses with granule cells. We will especially investigate how synaptic activity on the mitral cell's dendrites influences the dynamics of the cell.

### 2.2.3 MORPHOLOGY OF GRANULE CELLS

We describe the morphology of the second cell type we consider, the granule cells, based on published data here. See Figure 2.3 (b) for a schematic picture of a granule cell. The perikarya of the granule cells, i.e. the part of the cell containing the nucleus, is round to fusiform and very small. Its average diameter is  $6\mu m$  to  $10\mu m$  [90]. A long, stout processes arise from the perikarya, beginning thick and is invariably directed towards the mitral cell and external plexiform layers with a constant diameter of  $1\mu m$  to  $3\mu m$  and a length of  $50\mu m$  to  $200\mu m$  [81, 106]. At the level of the mitral cells it branches repeatedly and then ramifies among the mitral cell dendrites in the external plexiform layer [90, 107]. On the dendrites of the granule cells one finds spine-like appendages. From the deep side of the perikarya one to four dendrites extend towards the deepest layers of the bulb.

Granule cells appear to be electronically short [17, 106]; thus depolarization of any part of the cell spreads relatively effectively to all parts of the cell. Granule cells can produce spikes in response to activation by mitral cells.

### 2.2.4 PASSIVE PROPERTIES OF THE MITRAL AND GRANULE CELLS

In [17] one finds the passive properties of the MCs and the GCs of the mammalian OB.

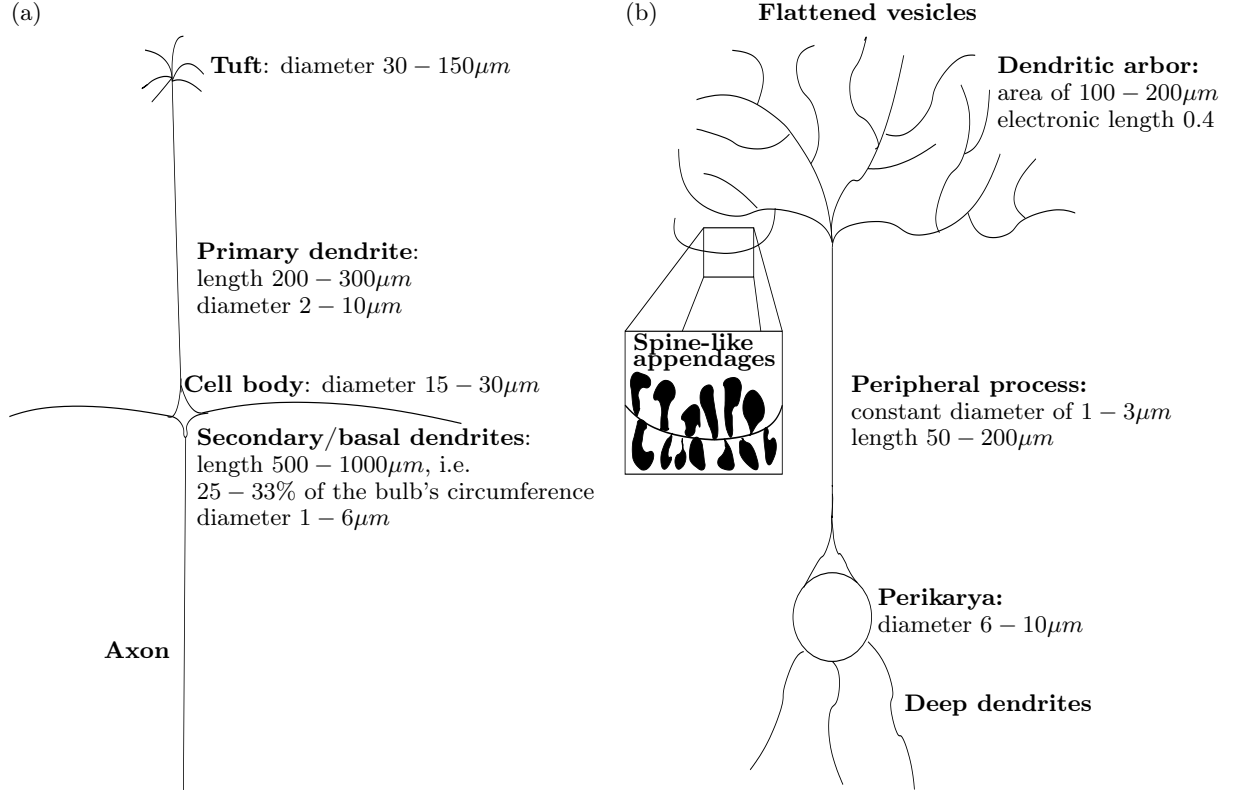


Figure 2.3: *Main building blocks of the OB network. (a) Mitral cell receives the input to OB network at its tuft, and signal processing is performed at the secondary dendrites. The axons project the network output to deeper brain regions. Mitral cells are reciprocally connected through granule cells, shown in (b). Granule cells are a type of inhibitory nerve cells without axon.*

They are reproduced in the following table.

	MC	GC
Membrane Capacity	$1.0 \frac{\mu F}{cm^2}$	$1.0 \frac{\mu F}{cm^2}$
Membrane Resistance	$100 k\Omega cm^2$	$120 k\Omega cm^2$
Axial Resistance	$200 \Omega cm$	$50 \Omega cm$

### 2.3 THE MITRAL-GRANULE CELL NETWORK

In this section we state the known connection properties of the network formed in the OB by mitral and granule cells. In total we have in mammals approximately  $5 \times 10^4$  mitral and  $5 \times 10^6$  granule cells [30]. In zebrafish we have about 600 to 700 MCs and about 5000 to 6000 GCs [107].



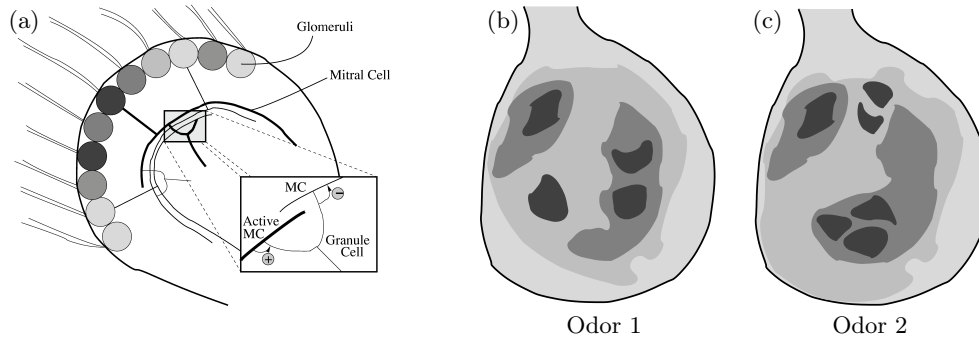


Figure 2.4: *Organization and activity of the OB. (a) Schematic figure of the olfactory bulb with the inhibitory connections between mitral (MC) and granule cells. Shading in grey shows the level of activity of a glomerulus. (b) and (c) show schematically how the activity of the olfactory network results in an odor map. Shading indicates again the activity. For two different odors it is possible that there are parts where the map is similar, while others are clearly distinguishable.*

The mitral-granule cell network is very dense, as the following consideration shows [107]: about 25 mitral cells, with approximately 150 secondary dendrites, project into a single glomerulus. If the secondary dendrites extend radially outward equally there is one dendrite per 2.4 degrees. This means the distance between two dendrites in a distance from  $2mm$  of the center is about  $80\mu m$ . Hence, each granule cell could be connected to dendrites of several mitral cells from each glomerulus.

Mitral cell dendrites of mammals extend up to one-third of the length of the olfactory bulb and can, therefore, form synapses with many granule cells and influence the reaction to the input of distant glomeruli [107]. This process may be dependent on dendritic excitability, because simple cable properties cannot account for passive transmissions of information at such a distance [112].

This situation is quite different in teleosts like, for example, in zebrafish [46]. They have two types of mitral cells: unidendritic and multidendritic. The latter are comparable to the MCs of mammals with respect to the scope of their dendrites. But these cells are in the minority (about 31% of the MCs of a zebrafish). The majority are unidendritic MCs which have a tuft at the end of their single dendrite with a diameter of about  $20\mu m$ . This comes to a scope of only 10% of the OB [22]. We will see in Chapter 8 that this anatomical difference between mammals and teleosts may give an explanation why traveling-waves-like dynamics appears only in experiments with zebrafish, not with mammals.

### 2.3.1 SYNAPSES

In the network of the OB there exist only synapses between granule and mitral cells, not

between cells of the same type [91]. The synapses are reciprocal and can be found on all secondary dendrites of the mitral cells. In the olfactory bulb we have  $10^4$  synapses per mitral cells. Secondary mitral cell dendrites are characterized by a high synaptic density, while primary dendrites have only few or no synapses [89, 104]. The synapses between granule and mitral cells have GABA<sub>A</sub> receptors, while the mitral-granule cell synapses have AMPA and NMDA receptors [32]. The density of these synaptic interactions suggests their fundamental importance to the functionality of the bulb [107].

### 2.3.2 NETWORK INPUT AND OUTPUT

The input to the network is given from the glomeruli. About 25 mitral cells receive input from a single glomerulus [107]. Mitral cells associated with the same glomerulus receive similar afferent input from olfactory receptor neuron axons and show more similar activity patterns than mitral cells associated with different glomeruli [7]. This picture may be different if intraglomerular inhibition is strong. However, since not much is known about the activity on the glomerular level, we do not include the intraglomerular inhibition in our model. Our model receives input from the glomeruli assuming that the intraglomerular inhibition is included in the input signal. The knowledge of the spatial and temporal characteristics of lateral inhibition and lateral excitation on the mitral and granule cell level is critical for determining how the olfactory bulb circuits shape the fast and slow patterns (see Figure 2.4, right part) of odor-evoked activity seen in the mitral cell network [118] and is, therefore, included in the model.

The spiking activity of the MCs form the output of the OB network. The GCs are responsible for the signal processing within the network. They do not contribute to the output [107]. Nevertheless, in imaging experiments with voltage-sensitive dyes the dynamics of the GCs are depicted as well [44], hence we will investigate their spiking activity in cases where we compare the results to such experiments, too.

## 2.4 NEURON DYNAMICS

The spatiotemporal dynamics of the single neurons forming the neuron network is explored in this section. There exist several models for the neuron dynamics in the literature: different integrate-and-fire models and reaction-diffusion models like the models of Hodgkin and Huxley [56] or of Fitz-Hugh and Nagumo [83]. We will use the Spike Response model [50], which is described in Section 2.4.1 for our network model with point neurons.

All integrate-and-fire models are simplifications. If one wants to simulate neurons with their spatial expansion, the standard model is the one of Hodgkin and Huxley. It describes how action potentials in neurons are initiated and propagated [56]. It is a set of nonlinear ordinary differential equations that approximates the electrical characteristics of excitable cells coupled to the cable equation modeling signal propagation. Alan Lloyd Hodgkin and

Andrew Huxley described the model in 1952 to explain the ionic mechanisms underlying the initiation and propagation of action potentials in the squid giant axon. They received the 1963 Nobel Prize in Physiology or Medicine for this work. In Chapter 5, we simulate the dynamics of single mitral cells with spatial expansion using the model of Hodgkin and Huxley, introduced in Section 2.4.2.

The Spike Response model (SRM) is a generalization of the leaky integrate-and-fire model [50]. In the SRM the dynamics of the neurons depends among others on the time since the last output spike. The model describes the membrane potential at time  $t$  and uses a threshold condition to determine when a spike occurs. The explicit dependence of the membrane potential upon the last output spike allows to interpret the refractoriness of a neuron as a reduced responsiveness after an output spike which results in an increase in threshold after firing. Simple phenomenological spiking neuron models like the SRM are highly popular for studies of neural coding, memory, and network dynamics. It is not difficult to implement them and they need less computation time and memory than more sophisticated neuron models, hence, larger networks of neurons can be simulated, see e.g. the review [39].

### 2.4.1 SPIKE RESPONSE MODEL

**T**he Spike Response model (SRM) is a model for point neurons including refractoriness and external input. The introduction of this model follows [41, 50]. The numerical values of the model parameters used in simulations can be found in Appendix A.2. The dynamics of SRM networks takes place in discrete time steps. The neurons are considered as point neurons, numbered with  $i \in \{1, \dots, n\}$ , and characterized by a spiking variable  $S_i(t) \in \{0, 1\}$  and the membrane potential  $h_i(t) \in \mathbb{R}$ . The time the signal needs to travel across the dendrites from neuron  $i$  to neuron  $j$  is modeled by a delay  $\Delta_{ij}^{den}$ . The strength of the interactions between single neurons, i.e. the synaptic strength, is described by the matrix  $J \in \mathbb{R}^{n \times n}$ . A positive entry  $J_{ij}$  stands for an excitatory synapse between neuron  $i$  and neuron  $j$ , while a negative entry represents an inhibitory synapse.

The dynamics of the model is based on firing events of single neurons, so-called spikes. Spikes are stereotyped events which are assumed to be fully characterized by the firing time. The spike width equals a basic time step  $\Delta t$ . If a spike occurs at neuron  $i$  at time  $t$  the spiking variable  $S_i(t)$  is equal one, otherwise it is zero. Neuron  $i$  will trigger a spike if its membrane potential crosses a threshold  $\theta$  from below. This behavior is modeled by the so-called threshold condition

$$S_i(t + \Delta t) = \begin{cases} 1, & \text{if } h_i(t) \geq \theta, \frac{dh_i}{dt}(t) > 0, \\ 0, & \text{else.} \end{cases} \quad (2.1)$$

The membrane potential is modeled with four terms in the SRM

$$h_i(t) = h_i^{syn}(t) + h_i^{s-inh}(t) + h_i^{ext}(t) + h_i^{ref}(t). \quad (2.2)$$

We have a look at the four components of the membrane potential (2.2) starting with the synaptic contribution

$$h_i^{syn}(t) = \sum_{j=1}^N J_{ij} \sum_{\tau=0}^{\infty} \epsilon(\tau) S_j(t - \tau - \Delta_{ij}^{den}), \quad (2.3)$$

with  $\epsilon(\tau) = \frac{\tau}{\tau_\epsilon^2} \exp(-\frac{\tau}{\tau_\epsilon})$  and the synaptic parameter  $\tau_\epsilon$ . Here, the influence of the spiking activity of neuron  $j$  on neuron  $i$  is modeled by the sum of previous activities of neuron  $j$  weighted by the synaptic strength  $J_{ij}$ . The summands themselves are weighted by the function  $\epsilon(\tau)$ , which decreases the influence of the synaptic activity as it lies back in time. This way of modeling the synaptic contribution allows to integrate over the last pre-synaptic activities, as it is also done in neurons [51].

The self-inhibitory contribution  $h_i^{s-inh}(t)$  is responsible for setting the neuron potential back to its resting potential after firing. It reads

$$h_i^{s-inh}(t) = \sum_{\tau=0}^{\tau_{max}} \eta(\tau) S_i(t - \tau - \Delta_i^{s-inh}),$$

with a delay  $\Delta_i^{s-inh}$  after which the self-inhibition is activated and  $\eta(\tau) = \eta_{inh} \exp(-\frac{\tau}{\tau_\eta})$ ,  $\eta_{inh} < 0$ . As in the case of the synaptic contribution, the spiking activity of the past influences the self-inhibition. The influence is again decreased as the spiking activity lies back in time. Hence, not only the last spiking events of a neuron but all events in  $[t - \tau_{max}, t]$  influence its state. This effect can also be found experimentally [51].

Additionally, some external input  $h_i^{ext}(t)$  can be included and the refractoriness of the neuron is taken into account by

$$h_i^{ref}(t) = \begin{cases} -R, & \text{if } t_i^f \leq t \leq t_i^f + \tau_{ref}, R \gg 1 \\ 0, & \text{else.} \end{cases}$$

$t_i^f$  stands for the firing time, when the last spike was triggered for neuron  $i$ ,  $\tau_{ref}$  is the refractory time of the neurons and  $R$  is the amount the membrane potential is decreased after a spike occurred.

A spiking neuron locking theorem can be proven for the SRM [52]. It shows when coherent oscillations are asymptotically stable in a spatially homogeneous network of spiking neurons. This was generalized for a model of the locust olfactory system, the antennal lobe, in [110].

### 2.4.2 HODGKIN-HUXLEY MODEL

Besides the point neurons, where the dynamics is modeled by the SRM we consider also neurons that are resolved in space. We give here a basic description of the dynamics happening at the membrane of a nerve cell. For more details we refer, for example, to

the book [36]. It is known that neuronal signals travel along the cell membrane in the form of a local voltage difference across the membrane. In the resting state of a neuron the cytoplasm, i.e. the cellular fluid inside the neuron, contains an ionic composition that makes the cell interior slightly negative in potential with respect to the outside. The difference is about  $-50mV$ . As an action potential is triggered the potential difference is raised to about  $-30mV$  to  $-20mV$  at some site of the membrane and the following sequence of events occurs:

1. Sodium channels open, letting  $Na^+$  ions enter the cell interior. This causes the membrane potential to depolarize further.
2. After a slight delay, the potassium channels open, letting  $K^+$  leave the cell. This restores the original polarization of the membrane, and further causes an overshoot of the negative rest potential.
3. The sodium channels close in response to the decrease in the potential difference.
4. Adjacent to a position that has experienced these events, the potential difference exceeds the threshold level necessary to set step one in motion. This process repeats, leading to spatial conduction of the spike-like signal. The action potential can thus be transported down the length of the axon without attenuation or change in shape, i.e. it forms a traveling wave.

Alan Lloyd Hodgkin and Andrew Huxley described a model for this process underlying the initiation and propagation of action potentials in the squid giant axon [56]. We will state their model here, for more details see e.g. [19, 36]. Let  $\Omega \subset \mathbb{R}$  be an interval modeling a piece of an axon of a neuron and  $T = [0, T_{end}]$  a time interval of interest. We have the membrane potential  $v : \Omega \times T \rightarrow \mathbb{R}$  and the concentrations  $c_k : \Omega \times T \rightarrow \mathbb{R}$  for  $k \in C = \{Na, K, L\}$ .  $c_{Na}$  and  $c_K$  denote the sodium and potassium concentrations, while  $c_L$  gives rise to a leakage current. Then the system of the Hodgkin-Huxley equations coupled to the cable equation reads

$$C_M \frac{\partial v}{\partial t} = \frac{\partial}{\partial x} \left( D_m \frac{\partial v}{\partial x} \right) - \sum_{k \in C} I_k(v, c_k) - I_s(v, t), \quad (2.4)$$

$$\frac{\partial c_k}{\partial t} = \alpha_k(v)(1 - c_k) - \beta_k(v)c_k, \quad \forall k \in C. \quad (2.5)$$

The system (2.4-2.5) consists of a parabolic partial differential equation, the cable equation coupled to a reaction system. The currents  $I_k$  and  $I_s$  are given by

$$I_{Na}(v, c) = g_{Na} c_{Na}^3 c_L (v - v_{Na}), \quad (2.6)$$

$$I_K(v, c) = g_K c_K^4 (v - v_K), \quad (2.7)$$

$$I_L(v, c) = g_L (v - v_L) \quad (2.8)$$

and

$$I_s(v, t) = g_{syn}(t)(v - v_{syn}). \quad (2.9)$$

The current (2.9) models the synaptic input and is not part of the original Hodgkin-Huxley system. Nevertheless, we use this part to model the activity in networks of neurons [14]. The functions  $\alpha_k$  and  $\beta_k$  in the reaction system are given by

$$\begin{aligned} \alpha_{Na}(v) &= 0.1 \frac{-v+25}{\exp((-v+25)/10)-1} & \beta_{Na}(v) &= 4 \exp(-v/28) \\ \alpha_K(v) &= 0.01 \frac{-v+10}{\exp((-v+10)/10)-1} & \beta_{Na}(v) &= 0.125 \exp(-v/80) \\ \alpha_L(v) &= 0.07 \exp(-v/20) & \beta_L(v) &= \frac{1}{\exp((-v+30)/10)+1}. \end{aligned}$$

In the system (2.4-2.5) the potential  $v$ , currents  $I_k$ , and time  $t$  are measured in  $mV$ ,  $\mu A$  and  $ms$  respectively.  $C_M$  denotes the capacity of the neuron membrane.  $D_m$  is given by  $1/R_i$  where  $R_i$  is the intracellular resistivity. The constants  $g_{Na}$  and  $g_K$  are maximal conductances of the membrane for these ions, while  $g_L$  is the leak conductance that corresponds to the passive membrane resistivity  $R_M$ .  $v_{Na}$ ,  $v_K$ , and  $v_L$  denote that part of the resting potential that is due to the concentrations of sodium, potassium, and all other mobile species.  $g_{syn}(t)$  is the time-dependent conductance given by a function that is specific for an individual synapse type, and  $v_{syn}$  is the reversal potential for the synapse.

The model given here describes the active propagation of the action potential along the axon of the neuron. In the dendritic part passive signal propagation is often sufficient, which is modeled by the cable equation above without the reaction part involving the concentrations  $c_k$ ,  $k \in C$ .

## 2.5 OLFACTORY BULB NETWORK MODEL

After the considerations of the biological basics and the dynamics of single neurons, we are able to state our model for the neuron network in the OB. The values for the parameters used in simulations are stated in Appendix A.2.

We model the network as a planar, two-dimensional network with an uniform distribution of  $n_m$  mitral cells. This makes sense, since the mitral cells are arranged in almost a monolayer [107]. We arrange  $n_g$  granule cells in the same manner in a plane. For the positions of the granule cells, analyses of inter-cell distances show that there were no consistent variations in the bulb [86]. For the dynamics of the single mitral and granule cells we use the Spike Response model introduced in Section 2.4.1. The distance between the MCs and the GCs are mapped to the model by delays in the signal traveling times.

The MCs get input from the glomeruli they form synapses with. To model this in the point neuron case, the external input  $h_{ext}(t)$  of the MCs is set to non-zero values, compare Equation (2.2).

The connectivity of the neurons in the model network has to be modeled in order to map the synaptic structure of the OB network. We assume that the probability of a mitral

cell forming a synapse at a given point depends only on the radial distance from the soma and not on the direction [30]. This is an approximation since the dendrites project in definite directions from the soma. But dendrites of the GCs branch repeatedly, so this approximation appears reasonable. The probability of forming a synapse is zero outside a certain radius determined by the length of the mitral cell secondary dendrites. We call this maximal radius  $r_{exc}$ , the radius of excitation, since MCs excite the GCs they form synapses with. It is chosen as a parameter in our model.

As mentioned above, the secondary dendrites of the mitral cells and the granule cell peripheral dendrites are reciprocally connected by spike-triggered synapses. This is modeled with the connection matrix  $J = (J_{ij}) \in \mathbb{R}^{n_m+n_g} \times \mathbb{R}^{n_m+n_g}$ , compare Equation (2.3), where  $n_m$  is the number of MCs and  $n_g$  is the number of GCs. We define  $J$  as

$$J_{ij} = \begin{cases} J_{exc}, & \text{MC } i \text{ and GC } j, d_{ij} < r_{exc} \\ -J_{inh} \exp(-\frac{10d_{ij}}{r_{inh}}), & \text{GC } i \text{ and MC } j, d_{ij} < r_{exc} \\ 0 & \text{else.} \end{cases} \quad (2.10)$$

with positive constants  $r_{inh}$ ,  $J_{inh}$ , and  $J_{exc}$ , and  $d_{ij}$  denoting the euclidean distance between neuron  $i$  and neuron  $j$ . The strength of the inhibitory synapses in the OB, i.e. between GCs and MCs, is about  $2.5nS$  [71]. To our knowledge nothing is known about the strength of the exhibitory synapses of the system. The ideas behind choosing  $J$  in the way described in Equation (2.10) are:

- Inside the radius of excitation  $r_{exc}$  each MC and each GC are assumed to form an excitatory synapse. The strength of theses synapses does not depend on the distance to the soma, i.e. equals  $J_{exc}$ .
- The excitatory synapses always come in pairs with inhibitory synapses. For the signal coming back from the GCs to the MCs, cable theory has to be taken into account, since passive signal propagation occurs on the dendrites. We model this by an exponential decay of the synaptic strength defined by the strength of the inhibitory synapses  $J_{inh}$ . The radius  $r_{inh}$  determines the strength of the signal decay due to the conductivity of the MC's secondary dendrites.

In our simulations we will investigate the network behavior depending on the connection parameters  $r_{exc}$ ,  $r_{inh}$ ,  $J_{exc}$ , and  $J_{inh}$ . We conclude this section by a short summary of the OB network model in Statement 2.5.1.

**STATEMENT 2.5.1 (MODEL OF THE OLFACTORY BULB NETWORK)** *We model the olfactory network including  $n_m$  mitral cells and  $n_g$  granule cells as point neurons with Spike Response dynamic described with Equations (2.1) and (2.2). The connectivity of the network with its reciprocal connections between the different cell types is modeled by*

the choice of the synaptic strength matrix  $J = (J_{ij}) \in \mathbb{R}^{n_m+n_g} \times \mathbb{R}^{n_m+n_g}$  described in Equation (2.10). Since not much is known about the connections properties in the OB network, this model depends on the following connection parameters: the radii of interaction  $r_{exc}$  and  $r_{inh}$  and the strength of the synapses  $J_{exc}$  and  $J_{inh}$ .

## 2.6 ABILITIES OF THE NETWORK

Distributed patterns of activity in response to chemical stimuli are transmitted to the OB via the axons of olfactory sensory neurons which terminate in the glomeruli of its input layer. The OB is believed to filter and transform these incoming sensory data, performing normalization, contrast enhancement, and similar operations before conveying the processed olfactory information to several different secondary structures via mitral cells [26]. In this section we give a short overview of the processing of olfactory signals in the OB.

### 2.6.1 LATERAL INHIBITION AND CONTRAST ENHANCEMENT

The term contrast enhancement was first introduced for horizontal cells in the retina [112]. They mediate lateral inhibition and thereby sharpen the contour of the image transmitted to the brain [63]. In the OB stimulus information is represented in the network by patterns of activity across many neurons. A mitral cell responds to excitations from the glomeruli on a time scale of hundreds of milliseconds [118]. Tuning profiles of mitral cells change over time, becoming progressively more different from the initial profile [44]. The correlation of different tuning profiles of the network compared to the initial one decreases steeply for about 800ms and more slowly thereafter. Late tuning profiles are not simply sharpened versions of the initial ones, but easier distinguishable odor maps. This process is called contrast enhancement and can be found in the OB [7, 27, 80, 101, 112, 117, 124].

It is assumed that the lateral inhibition, a well known principle in neural systems conveying sensory information is responsible for the contrast enhancement properties of the OB. In Chapter 6 we test our model and show that it is able to reproduce lateral inhibition and contrast enhancement, and we investigate how changes in the connectivity parameters of the network influence its lateral inhibition and contrast enhancement properties.

### 2.6.2 ODOR DISCRIMINATION

Behavior experiments show that rats need more time to distinguish binary odor mixtures the more similar the mixtures are [1]. We reproduce this result with our model and investigate how the connection parameters of the network influence its abilities to perform odor discrimination tasks in Chapter 7.



### 2.6.3 TRAVELING WAVES

Besides the well known phenomena of contrast enhancement and odor discrimination other phenomena are found in experiments. In [44] imaging experiments with voltage-sensitive dyes show traveling-wave-like structures in the dynamics of the olfactory bulb of zebrafish. These experiments measure the activity of the membranes of the cells. The experiments show, that traveling waves emerge in the olfactory bulb of zebrafish in oscillatory manner and that the propagation velocity and direction is nearly odor independent. In Chapter 8 we investigate which network connectivity properties are needed for the existence of traveling waves, and show how the shape of the network boundaries influences the shape of the traveling waves.

## 2.7 EARLIER SIMULATION APPROACHES

At the end of this chapter we give a short overview of simulation approaches for the olfactory bulb network as they can be found in the literature. For more details we refer to the review articles by Cleland and Linster [26] or de Souza and Antunes [31].

There are several publications dealing with the modeling and simulation of single cells. To our knowledge, the most detailed model presently available, a compartmental model for mitral and granule cells, was introduced in [17]. Based on published geometrical data, the passive electrical properties were explored by comparing the model output with intracellular potential from hyperpolarizing current injection experiments. The active channels were modeled based on the Hodgkin-Huxley formalism.

Another class of publications are dealing with models describing the whole network in the OB. In [27] non-topological contrast enhancement was investigated with a simple compartment model for small networks (10 glomeruli with one PG cell and one MC connected to each glomerulus). In [37] a mathematical model for describing dynamic phenomena in the olfactory bulb is presented. In a very simple network with point neurons (11 MCs and 11 GCs) the nature of attractors and the bifurcation sequences in terms of the lateral connections strength in the MC layer are studied numerically. A model for MCs and GCs as point neurons was developed in [69, 70]. Here, the olfactory bulb and the olfactory cortex are modeled in a feedback loop. The model of the olfactory bulb consist of 50 MCs and 50 GCs. This model was modified by [85], where an oscillatory model of the OB is given. In [110] a model of the antennal lobe (AL) of locusts is introduced. The AL is the equivalent to the OB in insects. Using the SRM a network with 200 cells was simulated.

In [28, 29, 30] a biologically realistic model of the mammalian OB with mitral and granule cells connected by dendrodendritic synapses was introduced. This model is one of the most detailed, realistic, and thoroughly investigated models of the mammalian olfactory bulb published. The single cells were modeled by four-compartment models which are simplifications of the models introduced in [17]. The task of synchronization of firing

patterns were discussed using this model. In networks with 25 to 100 mitral cells and 144 to 14,400 granule cells, several strategies were applied to reduce the complexity of the model to be able to perform numerical simulations. One possibility is to reduce the number of synapses and consider only a few hundred synapses per mitral cell. Another possibility is to look at a single glomerulus only. The number of cells that have to be taken into account are reduced by a factor of about 1,000, and if only one glomerulus is simulated the problem of outside inputs in the network is removed (except for background activity). A further strategy is to simulate only one mitral cell per glomerulus. The idea this strategy is based on is that mitral cells innervating the same glomerulus tend to have synchronized firing [104]. We will follow this strategy sometimes in the case of simulations with point neurons.

In this work we simulate large networks with up to 900 mitral and 8100 granule cells. This enables us to investigate the effects of network interactions more realistic than in small networks. Additionally, we are able to investigate the network dynamics with respect to changing connection parameters. Since not much about the connection properties is detectable in experiments this approach allows to get insights in the functionality of the olfactory bulb.

## 2.8 CONCLUSIONS OF CHAPTER 2: NEURON NETWORK OF THE OLFACTORY BULB

In this chapter, we introduced a model for the neuron network of the olfactory bulb. It is based on Spike Response dynamics for point neurons. The structure of the SRM is adapted to the biological facts known about the OB network. Choosing a model with point neurons allows us to simulate relatively large networks and get insights how the dynamics of the network depends on its connectivity.

Even if a lot is known about the morphology of the cells in the network, less is established about their connectivity. At this point we can use numerical simulation and analysis to investigate which parameter ranges for the connectivity parameters are feasible. The connectivity parameters are the radii of interaction  $r_{exc}$  and  $r_{inh}$  and the synaptic strength  $J_{exc}$  and  $J_{inh}$ .

## Chapter 3

# ADAPTIVE COMPUTATIONS FOR BRANCHED NERVE EQUATIONS

*From error to error one discovers  
the entire truth.*

SIGMUND FREUD

To get realistic insights in the dynamics of neuron networks by simulations, it might be not sufficient to consider networks of point neurons. In the framework of finite-element methods one is able to simulate the dynamics of neurons considering their spatial expansion based on the Hodgkin-Huxley model. For passive signal propagation, we develop error-based control for adaptive grids in space and time. Error estimators used for this approach are derived by applying standard energy estimate methods in this chapter.

---

In order to simulate the dynamics of large networks of neurons with their spatial expansion with high accuracy, we use an accurate and efficient numerical method to solve the Hodgkin-Huxley equations coupled to the cable equation, see Equation (2.4-2.5). This method was developed in the Simulation of Large Systems Department at the University of Stuttgart. It is based on a vertex-centered finite-element discretization in space and second order operator splitting methods in time. It is implemented in NeuroDUNE, a module of the toolbox DUNE (Distributed and Unified Numerics Environment) [11, 12, 13], which was developed at the Universities of Stuttgart, Freiburg, Münster, Heidelberg and at the FU Berlin.

NeuroDUNE solves signal propagation equations as they occur in the Hodgkin-Huxley model for neuron dynamics numerically on an adaptive grid [14, 67]. The partial differential equations of the Hodgkin-Huxley model are defined on a continuous part of space and a continuous time-interval. To solve them numerically space, time, and the model itself have to be discretized. This is done by error estimator based grid control, in order to discretize the space by a non-equidistant grid refined only where it is necessary, coarsened where it is possible. The chosen time-stepping scheme is Forward-Euler or Crank-Nicholson on non-equidistant time intervals, and the model is discretized by a finite-element method [38].

To be able to apply adaptive grid control in space and time, we develop a-posteriori error estimates, i.e. measures for the computation error based only on the numerical solution itself. Furthermore, we use these estimates to refine our spatial and time grids, if it is necessary, and use a coarse grid wherever it is possible. This approach makes sense, since the activity of neurons is local, i.e. around synapses or propagating action potentials, and there are areas where no activity takes place. It turns out that with this strategy we are, on one hand, able to control the computational error of the simulations and, on the other hand, we are able to speed up the simulations. This will be shown in Chapter 5.

**T**his chapter is organized as follows: In the next section the considered geometry and model equations are introduced. In Section 3.2 it is shown how the model equations are discretized to be able to solve them numerically. This is done on non-equidistant grids, which are the results of local grid refinement. The main principles of the approach of local grid refinement are introduced in Section 3.3. To be able to determine where and when the grids have to be refined and when they can be coarsened, one needs measures for the inaccuracies done on a given grid and during a certain time step. These measures, i.e. a-posteriori error estimates for the considered model equations, are developed, and an implementation for an adaptive grid control is presented in Section 3.4.

### 3.1 PASSIVE SIGNAL PROPAGATION FOR NEURONS

**I**n this section we shortly review the considered problems. We examine the equation for passive signal propagation on  $\Omega \subset \mathbb{R}^3$  with given initial and boundary values (for details see e.g. [19] and Section 2.4.2), which read

$$\begin{aligned} C_m \partial_t v - \partial_x (D_m \partial_x v) + g(x, t) v &= f(x, t) \quad \text{in } \Omega \times [0, T] \\ v(x, t) &= v^D(x), \quad x \in \Gamma_D \subset \partial\Omega, \\ -(D_m \frac{\partial v}{\partial x}) \nu &= J(x, t), \quad x \in \Gamma_N = \partial\Omega \setminus \Gamma_D, \\ v(x, 0) &= v^0(x). \end{aligned} \tag{3.1}$$

Hereby,  $v$  denotes the potential of the membrane,  $D_m$  is given as  $\frac{1}{R_i}$ , where  $R_i$  is the

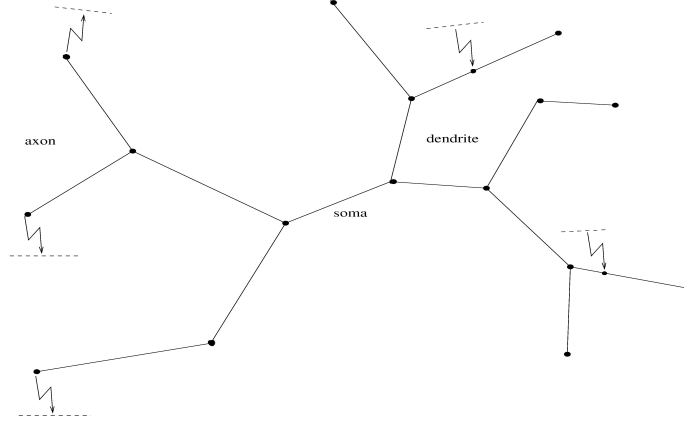


Figure 3.1: *Simulation area representing the geometry of a neuron with synaptic in- and output. Black dots indicate the nodes of the coarsest possible discretization. Note that a grid point is located at each intersection, at the synapses and at the boundary points of the area of the neuron  $\Omega$ .*

intracellular resistivity and  $C_m$  represents the membrane capacity. The functions  $g$  and  $f$  are given by

$$g(x, t) = g_L + g_s(x, t), \quad f(x, t) = g_s(x, t)v_s + g_L v_L$$

where  $g_s(x, t)$  stands for the synaptic input,  $g_L$  is the leakage constant and  $v_s, v_L$  are rest potentials.  $\Omega \subset \mathbb{R}^3$  denotes the domain of the considered neuron, which is for numerical simulations described by a graph, i.e. vertices  $V$  and edges  $E \subset V \times V$  with exactly one path from one vertex to any other (see Figure 3.1 for an example). For the process of numerically solving Equation (3.1), the derivatives with respect to  $x$ ,  $\partial_x$ , are approximated by finite differences in the direction of the single edges of the graph, i.e. separate on each discretization element, after the finite-element discretization as described in Section 3.2. The single edges can be seen as discrete structures combined with boundary conditions. Analytically, we embed the one dimensional manifold describing the neuron structure in  $\mathbb{R}^3$  and interpret the derivatives with respect to  $x$  as directional derivatives along the edges. On the boundary  $\partial\Omega = \Gamma_D \cup \Gamma_N$  we have Dirichlet boundary points on  $\Gamma_D$  and Neuman points on  $\Gamma_N$ .  $[0, T]$  is the time interval of interest.  $\partial_t$  denotes the time derivative.

Passive signal propagation as described in Equation (3.1) is based on the Hodgkin-Huxley equations (2.4-2.5) by omitting the reaction part involving the concentrations  $c_k$ ,  $k \in \{Na, K, L\}$ . It is often sufficient to investigate the dynamics of the dendritic part of a neuron where passive signal propagation takes place. If one considers parts of a neuron with active signal propagation, the complete Hodgkin-Huxley equations coupled with the cable equation (2.4-2.5) have to be used. All ideas presented here can be generalized for that case. The finite-volume discretization and the time stepping scheme for the complete

Hodgkin-Huxley model implemented in NeuroDUNE are introduced in [14]. A second order operator splitting method for the reaction and the diffusion part of the Hodgkin-Huxley equations is introduced there.

### 3.2 FINITE-ELEMENT DISCRETIZATION ON NON-EQUIDISTANT GRIDS

To solve Equation (3.1) numerically, it has to be discretized. The basis of the discrete formulation is a variational formulation of Equation (3.1). Let  $H_0^1(\Omega) = \{u \in H^1(\Omega) : u(x) = 0 \forall x \in \Gamma_D\}$  denote the Sobolev space of functions that are zero at the Dirichlet boundary points. Then the variational formulation of (3.1) reads:

$$(C_m \partial_t v, w) + a(v, w) = l(w; t) \quad \forall w \in H_0^1(\Omega), t > 0, v|_{t=0} = v^0, \quad (3.2)$$

with  $(v, w) = \int_{\Omega} uv \, dx$  denoting the  $L_2$ -inner product and

$$a(v, w) = (D_m \partial_x v, \partial_x w) + (gv, w), \quad (3.3)$$

$$l(w; t) = (f, w) - \sum_{x \in \Gamma_N} J(x)w(x). \quad (3.4)$$

Here, we assumed homogeneous Dirichlet boundary conditions  $v^D = 0$ . Non-homogenous Dirichlet boundary conditions can be considered as well (see any text book on the finite-element method, e. g. [38]).

Following the “method of lines” approach [54] we discretize (3.2) in space by choosing a finite-dimensional subspace  $S_h \subset H_0^1(\Omega)$ , e.g. piecewise linear and continuous functions. The computational grid used for  $S_h$  does not have to be equidistant. The resulting problem is a set of ordinary differential equations (ODEs) or differential-algebraic equations (DAEs). Hence, we get

$$(C_m \partial_t v_h, w) + a(v_h, w) = l(w; t) \quad \forall w \in S_h, t > 0, (v_h)|_{t=0} = I_h v^0, \quad (3.5)$$

with  $I_h$  denoting the nodal interpolation. The function  $v_h(x, t)$  is continuous in time but discrete in space. Choosing a basis  $\Phi_h = \{\phi_1, \dots, \phi_{n_h}\}$  of  $S_h$  we can write  $v_h(x, t) = \sum_{i=1}^{n_h} V_i(t) \phi_i(x)$ . Inserting this into (3.5) results in a system of ordinary differential equations for the coefficient functions  $V_i(t)$ .

Finally, we discretize the time interval  $[0, T]$  into possibly non-equidistant intervals

$$0 = t^0 < t^1 < \dots < t^k < \dots < t^N = T, \quad \tau^k = t^k - t^{k-1},$$

and replace  $\partial_t v_h$  with a difference quotient. This results in a sequence of fully discrete problems for  $v_h^k \in S_h$ :

$$v_h^0 = I_h v^0, \quad (3.6)$$

$$\frac{1}{\tau^k} (C_m v_h^k, w) + a(v_h^k, w) = l(w; t) + \frac{1}{\tau^k} (C_m v_h^{k-1}, w), \quad (3.7)$$

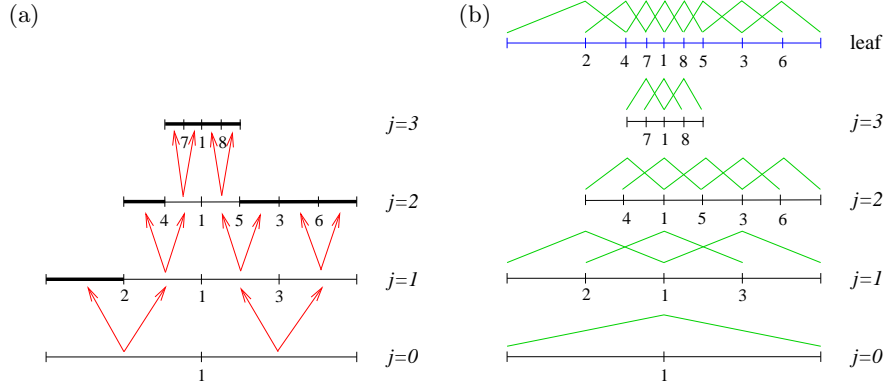


Figure 3.2: *Hierarchical grid refinement for a domain  $\Omega = (0, 1)$ . (a) The grid is constructed as follows: start with an intentionally coarse grid (level  $j = 0$ ). Then, subdivide each element into two elements of half size each, resulting in the grid on level  $j = 1$ . On this level, only three of the four elements are refined (level  $j = 2$ ), and then another two out of six elements are refined to obtain grid level  $j = 3$ . The leaf grid is indicated by bold lines. (b) shows the global nodal basis function for the different levels of the refined grid.*

for all  $w \in S_h$  and  $k > 0$ . This is equivalent to the implicit Euler method for the system of ordinary equations. Inserting a basis representation  $v_h^k(x) = \sum_{i=1}^{n_h} V_i^k \phi_i(x)$  into (3.7) results in a system of linear equations for the vector of coefficients  $V^k$ . This method is second order in space and first order in time even on non-equidistant spatial grids [14].

### 3.3 LOCAL GRID REFINEMENT

An important step in the adaptive computations for nerve equations is constructing a non-equidistant grid. This is done by hierarchical grid generation. Figure 3.2 illustrates this process which is introduced briefly here. For more details see e.g. [15] and references within. The initial grid is intentionally coarse. In the case of the discretization of neurons only the branching points, the synapses and the boundary points need to be resolved. In the example shown in Figure 3.2 the initial grid consists of two line elements and three nodes, and we then recursively subdivide individual elements into smaller elements, which leads to a tree structure. The elements on a given grid level  $j$  form a subdomain of  $\Omega$ . The finest grid in the grid hierarchy is called leaf grid. It is formed by all elements which are the leaves of their refinement tree. In Figure 3.2 the elements of the leaf grid are indicated by bold lines.

After the grid is formed one defines the finite dimensional subspace  $S_h$  of  $H_0^1(\Omega)$  on

the leaf grid formed by  $n_h$  elements  $\Omega_i$ ,  $1 \leq i \leq n_h$ . The  $\Omega_i$  are defined as

$$\Omega_i = \{x_i\} \cup \{(x_a, x_b) | a = i \vee b = i\}, \quad (3.8)$$

i.e. the region formed by all intervals incident to node  $i$  and including the node itself. For this discretization we approximate the potential  $v(x, t)$  to get the discrete problem (3.6-3.7) by linear basis functions

$$v_h(x, t) = \sum_{i=1}^{n_h} V_i(t) \phi_i(x), \quad (3.9)$$

with

$$\phi_i(x) = \begin{cases} 1 - \frac{\|x - x_i\|}{\|x_a - x_b\|} & x \in [x_a, x_b] \subset \Omega_i \\ 0 & \text{else} \end{cases}, \quad 1 \leq i \leq n_h, \quad (3.10)$$

where  $\|\cdot\|$  denotes the euclidean distance in  $\mathbb{R}^3$ . In Figure 3.2 (b) the linear basis functions corresponding to the grid hierarchy in Figure 3.2 (a) are shown to illustrate this approach. This leads to Statement 3.3.1.

**STATEMENT 3.3.1 (NON-UNIFORM DISCRETIZATIONS)** *Simulating the dynamics of neurons with their spatial expansion described by the passive signal propagation equation, see Equation (3.1), can be done by using finite-element discretization techniques. These techniques allow to use non-uniform grids and time steps.*

### 3.4 A-POSTERIORI ESTIMATES & ADAPTIVE GRID CONTROL

As result of the discretization in space and time as described in Sections 3.2 and 3.3 one obtains the discrete problem (3.6-3.7) which describes the behavior of the neuron dynamics on non-equidistant finite grids. During these approximations inaccuracies occur, i.e. there is a difference between the unknown analytical solution of Equation (3.1) and the numerical solution of Equation (3.7) for given initial and boundary values. This error depends on the structure of the problem, the grids, the discretization method and the time stepping scheme chosen. For a given problem, it is a-priori not known how large this error is. However, we want to control the error by refining the grids wherever it is necessary and to speed up the computations by coarsen them whenever it is possible. Therefore, we search for measures for the error based on the numerical solution on a given discretization of the domain  $\Omega$  and during a certain time step. Because we only evaluate the numerical solution, these measures are called a-posteriori error estimates [4, 9, 92].



### 3.4.1 SPATIAL GRID CONTROL

We control the spatial and the time grid independently. Therefore, we introduce a measure for the difference between the analytical solution of (3.1) and the numerical solution of (3.5) in each time step. We define the spatial error as  $e^s = \|v(t^k) - v_h^k\|$ . We will see later, which norm is used here. In the following an estimate for this error is derived by a standard duality based approach [38] using energy estimates for Equation (3.5). Following the arguments in [121] we show that the residual is a good approximation for the error.

For the development of the error estimator, we will simplify Equation (3.1) by neglecting the input from the synapses, i.e.  $g(x, t) = 0$ , for all  $(x, t) \in \Omega \times [0, T]$ . This is feasible, since the synapses are always demanded to be resolved in the grid, and we will see later that the control of the time steps takes the synaptic activity into account. Furthermore, we consider  $D_m, C_m$  and  $g_L$  to be constants. This is possible, since the error estimator will be evaluated separately on each control volume. Additionally, we set for lucidity  $D_m = C_m = g_L = 1$ . And finally, we consider only zero boundary conditions. Hence, the considered equations read

$$\begin{aligned} \partial_t v - \Delta v + v &= f && \text{in } \Omega \times [0, T], \\ v &= 0, && x \text{ on } \Gamma \times [0, T], \\ v(\cdot, 0) &= v^0(x) && \text{in } \Omega. \end{aligned} \tag{3.11}$$

For the derivation of the error estimator we look at a single edge of the neuron (compare Figure 3.1). Hence, no branching points occur. This can be done since the error estimator will be evaluated locally, i.e. on each element, in order to decide which elements have to be refined, respectively, can be coarsened. In the analytical derivation of the error estimator one piece of the neuron is not seen as an one-dimensional object, but as a domain  $\Omega \subset \mathbb{R}^3$  having a Lipschitz boundary  $\Gamma$ . This enables us to apply the standard techniques of analysis. The final time  $T$  is arbitrary, but kept fixed in the following. For simplicity, the right-hand side  $f$  is assumed to be measurable and square-integrable on  $\Omega \times (0, T]$  and to be continuous with respect to time.  $v_0$  is assumed to be measurable and square-integrable on  $\Omega$ .

Analogously, as for the complete equation for passive signal processing, we can rewrite Equation (3.11) in its variational formulation and discretize the solution in space and time like in Equation (3.6-3.7).

We associate with the sequence of numerical solutions of (3.6-3.7)  $v_h^k$  the function  $v_h^{\tau}$ , which is piecewise affine on the time intervals  $[t^k, t^{k+1}]$ ,  $0 \leq k \leq (N-1)$ , and equals  $v_h^k$  at times  $t^k$ ,  $0 \leq k \leq N$ .

Before deriving the error estimator, we state the notation used for function spaces and norms, for more details, see e.g. [5]. By  $H^n(\Omega)$ ,  $n \in \mathbb{N}_0$ ,  $L^2(\Omega) = H^0(\Omega)$  we denote the usual Sobolev and Lebesgue spaces equipped with the standard norms  $\|\cdot\|_n = \|\cdot\|_{H^n(\Omega)}$ . As usual  $H_0^1(\Omega)$  denotes the space of all functions in  $H^1(\Omega)$  with vanishing trace on the boundary  $\Gamma$ .  $H_0^1(\Omega)$  is equipped with the norm  $|\cdot|_1 = \|\nabla \cdot\|_0$ . The dual space of  $H_0^1(\Omega)$

is denoted by  $H^{-1}(\Omega)$  and the corresponding duality pairing is  $\langle \cdot, \cdot \rangle$ .

Furthermore, we denote for any separable Banach space  $V$  and any two numbers  $a < b$  by  $L^2(a, b; V)$  and  $L^\infty(a, b; V)$  the spaces of measurable functions  $u$  defined on  $(a, b)$  with values in  $V$  such that the function  $t \rightarrow \|u(\cdot, t)\|_V$  is square integrable, respectively, essentially bounded. These spaces are equipped with the norms

$$\begin{aligned}\|u\|_{L^2(a, b; V)} &= \left( \int_a^b \|u(\cdot, t)\|_V^2 dt \right)^{\frac{1}{2}} \\ \|u\|_{L^\infty(a, b; V)} &= \text{ess. sup}_{a < t < b} \|u(\cdot, t)\|_V.\end{aligned}$$

As in [121] we introduce the abbreviation

$$X(a, b) = \{u \in L^2(a, b; H_0^1(\Omega)) \cap L^\infty(a, b; L^2(\Omega)) : \partial_t u \in L^2(a, b; H^{-1}(\Omega))\}$$

and equip  $X(a, b)$  with its graph norm

$$\|u\|_{X(a, b)} = \left\{ \|u\|_{L^\infty(a, b; L^2(\Omega))}^2 + \|u\|_{L^2(a, b; H_0^1(\Omega))}^2 + \|\partial_t u\|_{L^2(a, b; H^{-1}(\Omega))}^2 \right\}^{\frac{1}{2}}.$$

By using these notations, the weak form of Problem (3.11) reads, find  $v \in L^2(a, b; H_0^1(\Omega))$  such that  $\partial_t v \in L^2(a, b; H^{-1}(\Omega))$ ,  $v(\cdot, 0) = v_0$  and for almost every  $t \in (0, T)$  and all  $w \in H_0^1(\Omega)$

$$(\partial_t v, w) + (\nabla v, \nabla w) + (v, w) = (f, w). \quad (3.12)$$

We are now able to use  $v_h^\tau$  to define the residual  $R(v_h^\tau) \in L^2(a, b; H^{-1}(\Omega))$  by

$$\langle R(v_h^\tau), w \rangle = (f, w) - (\partial_t v_h^\tau, w) - (\nabla v_h^\tau, \partial_x w) - (v_h^\tau, w), \quad (3.13)$$

for all  $w \in H_0^1(\Omega)$ . Adding the variational formulation (3.12) with the analytical solution  $v$  and choosing  $w = (v - v_h^\tau)(\cdot, t)$ , we get

$$(\partial_t(v - v_h^\tau), v - v_h^\tau) - (\nabla(v - v_h^\tau), \nabla(v - v_h^\tau)) - (v - v_h^\tau, v - v_h^\tau) = \langle R(v_h^\tau), v - v_h^\tau \rangle. \quad (3.14)$$

Following the arguments given in [121], we get by choosing  $t \in (0, t_k]$

$$(\partial_t(v - v_h^\tau)(\cdot, t), (v - v_h^\tau)(\cdot, t)) = \frac{1}{2} \frac{d}{dt} \|(v - v_h^\tau)(\cdot, t)\|_0^2, \quad (3.15)$$

$$(\nabla(v - v_h^\tau)(\cdot, t), \nabla(v - v_h^\tau)(\cdot, t)) = \|(v - v_h^\tau)(\cdot, t)\|_1^2, \quad (3.16)$$

$$((v - v_h^\tau)(\cdot, t), (v - v_h^\tau)(\cdot, t)) = \|(v - v_h^\tau)(\cdot, t)\|_0^2. \quad (3.17)$$

In addition, we can estimate

$$\begin{aligned}\langle R(v_h^\tau)(\cdot, t), (v - v_h^\tau)(\cdot, t) \rangle &\leq \|R(v_h^\tau)(\cdot, t)\|_{-1} \|(v - v_h^\tau)(\cdot, t)\|_1 \\ &\leq \frac{1}{2} \|R(v_h^\tau)(\cdot, t)\|_{-1}^2 \\ &\quad + \frac{1}{2} \|(v - v_h^\tau)(\cdot, t)\|_1^2.\end{aligned} \quad (3.18)$$

Using (3.15-3.18), we get

$$\frac{d}{dt} \|(v - v_h^\tau)(\cdot, t)\|_0^2 + \|(v - v_h^\tau)(\cdot, t)\|_1^2 + 2\|(v - v_h^\tau)(\cdot, t)\|_0^2 \leq \|R(v_h^\tau)(\cdot, t)\|_{-1}^2.$$

We integrate from zero to  $t$  and get

$$\begin{aligned} \|(v(t) - v_h^\tau)(\cdot, t)\|_0^2 &= \|v_0 - I_0 v_0\|_0^2 \\ &+ \int_0^t \|(v - v_h^\tau)(\cdot, s)\|_1^2 ds + \int_0^t \|(v - v_h^\tau)(\cdot, s)\|_0^2 ds \\ &\leq \|R(v_h^\tau)(\cdot, t)\|_{L^2(0, t_k; H^{-1}(\Omega))}^2. \end{aligned}$$

Since  $t \in (0, t^k]$  was arbitrary, this yields

$$\|v - v_h^\tau\|_{L^\infty(0, t^k; L^2(\Omega))}^2 \leq \|v_0 - I_0 v_0\|_0^2 + \|R(v_h^\tau)\|_{L^2(0, t_k; H^{-1}(\Omega))}^2 \quad (3.19)$$

and

$$\|v - v_h^\tau\|_{L^2(0, t^k; H_0^1(\Omega))}^2 \leq \|v_0 - I_0 v_0\|_0^2 + \|R(v_h^\tau)\|_{L^2(0, t_k; H^{-1}(\Omega))}^2. \quad (3.20)$$

Additionally, we have

$$\|v - v_h^\tau\|_{L^2(0, t^k; L^2(\Omega))}^2 \leq \|v_0 - I_0 v_0\|_0^2 + \|R(v_h^\tau)\|_{L^2(0, t_k; H^{-1}(\Omega))}^2. \quad (3.21)$$

On the other hand, starting again with Equation (3.14) we get

$$\|\partial_t(v - v_h^\tau)\|_{-1} \leq \|R(v_h^\tau)\|_{-1}^2 + \|v - v_h^\tau\|_1^2 + 2\|v - v_h^\tau\|_0^2.$$

Taking the square of this inequality and, as above, integrating from zero to  $t_k$ , and inserting the estimates from above gives

$$\|\partial_t(v - v_h^\tau)\|_{L^2(0, t_k; H^{-1}(\Omega))}^2 \leq 2\|v_0 - I_0 v_0\|_0^2 + 4\|R(v_h^\tau)\|_{L^2(0, t_k; H^{-1}(\Omega))}^2. \quad (3.22)$$

Combining the estimates (3.19-3.22) we proved the following theorem.

**THEOREM 3.4.1 (ERROR BOUND)** *The error in solving Equation (3.11) can be bounded from above by*

$$\|v - v_h^\tau\|_{X(0, t^k)}^2 \leq \left\{ C_1 \|v_0 - I_0 v_0\|_0^2 + C_2 \|R(v_h^\tau)\|_{L^2(0, t_k; H^{-1}(\Omega))}^2 \right\}^{\frac{1}{2}}. \quad (3.23)$$

with constants  $C_1, C_2$ .

Equation (3.23) means, that the error in the computation can be estimated by evaluating the residual defined in (3.13). Note that Theorem 3.4.1 is a direct generalization of the error bound derived in [121]. There it was also shown, that the residual is not only a bound but is equivalent to the error  $\|v - v_h^\tau\|_{X(0, t^k)}$ .

We use the knowledge developed in Theorem 3.4.1 to introduce a heuristic a-posteriori error estimator for the spatial error  $e^s = \|v(t^k) - v_h^k\|_{X(0,t^k)}$  for branched nerve equations. Since the residual is a bound for  $\|v - v_h^\tau\|_{X(0,t^k)}$ , we evaluate the residual by evaluating it for the numerical solution  $v_h^k$  on each control element. We have

$$e^s \leq C \left( \sum_{i=1}^{n_h} \eta_i^2 \right)^{1/2} \quad (3.24)$$

with

$$\eta_i = h_i \|f - (C_m \partial_t^k v_h^k - \partial_x(D_m \partial_x v_h^k) + g v_h^k)\|_{2,i}, \quad (3.25)$$

omitting the contribution of the start values, since we can not control them during the computations.  $\|\cdot\|_{2,i}$  denotes the euclidean norm evaluated on the control element  $\Omega_i$ . In the implementation one has to take care whether a linear control element or a control element with a branching point is considered.  $h_i$  denotes the length of the control elements. For branched elements, we evaluate Equation (3.25) on each linear part of the element separately. Both, the analytic and the numerical solution fulfill the Neuman boundary conditions. Therefore, there are no boundary terms present in Equation (3.24). There are no terms resulting from the jumps at the boundaries of the discretization elements due to the fact that neurons are modeled by one-dimensional elements.  $\partial_t^k v_h$  is an approximation of the time derivative, meaning the difference quotient is used. By observing  $\partial_x(D_m \partial_x v_h) = 0$  for linear elements one evaluates  $\eta_i$  as

$$\eta_i = h_i \|g_s(v_s - v_h) + g_L(v_L - v_h) - C_m \frac{1}{\tau^k} (v_h^k - v_h^{k-1})\|_{2,i}. \quad (3.26)$$

We use the error estimate (3.24) and (3.26) to implement an adaptive grid control for the spatial grid. In each time step we compute an estimate of the local error on each element of the grid by evaluating Equation (3.26) only on the considered element. Using this information the following steps are applied:

1. If the sum of the local errors (which is a measure for the global error) is not below an user tolerance  $TOL$ , the  $\tau_{fine}$  percent of the grid elements with the largest errors are refined until we reach the finest refinement  $\max_{level}$  level allowed.
2. The  $\tau_{coarse}$  percent with the smallest errors are coarsened until we reach the coarsest refinement  $\min_{level}$  level allowed.

This leads to Statement 3.4.2.

**STATEMENT 3.4.2 (ADAPTIVE GRID CONTROL)** *By using the result of Theorem 3.4.1 the error estimator for the spatial error is defined by Equation (3.24) and (3.26). The grid control strategy used here achieves that each element in the grid contributes about the same local error to the global error.*

### 3.4.2 TIME STEP SIZE CONTROL

In addition to the spatial grid control we derive a new step length for the next time step, depending on a measure for the error done in the previous time step. This error is called temporal error  $E_h^t$ . In each time step system (3.7) is solved for the vector of coefficients  $V^k$ . Hence, we use a simple error indicator based on them:

$$E_h^t \approx \|V^k - V^{k-1}\|_\infty. \quad (3.27)$$

$\|\cdot\|_\infty$  denotes the maximum norm of a given vector in  $\mathbb{R}^{n_h}$ .

In the same manner as in the spatial grid control the right hand side of Equation (3.27) is used as measure for the temporal error  $E_h^t$  to implement a control for the length of the next time step  $dt^k = t^k - t^{k-1}$ :

1. If the time error (3.27) is larger than a bound  $\tau_{large}$  we decrease the next time step, but not below a minimum time step  $dt^{\min}$  (e.g.  $dt^{k+1} = 0.5dt^k$ ).
2. If the time error (3.27) is smaller than a bound  $\tau_{small}$  we increase the next time step, but not above a maximal time step  $dt^{\max}$  (e.g.  $dt^{k+1} = 2dt^k$ ).

We chose  $\tau_{large} > c\tau_{small}$ ,  $c$  sufficiently large, to get an interval where the time step is not changed at all.

**STATEMENT 3.4.3 (ADAPTIVE TIME STEP CONTROL)** *By measuring the computation error of the previous time step as in Equation (3.27) an adaptive control of the size of the simulation time steps is applied.*

In addition to the grid control described above, another point which has to be taken into account in the step size control are the synaptic activities. To resolve them an additional step size control is implemented. The synaptic activity is always triggered from outside, i.e. the time point when each synapse starts its activity is given. This point is always used as a point of the time grid  $t^k$ , and the length of the next time step is adapted afterwards due to the dynamical properties of the synapses,  $dt = dt^{syn}$ , if the actual time step computed by the error control is larger than  $dt^{syn}$ . Otherwise, the computed step size is used. By always accessing the start point of synaptic activity, it is guaranteed that the solver is not integrating past a synaptic activity without even noticing it.

## 3.5 CONCLUSIONS OF CHAPTER 3: ADAPTIVE COMPUTATIONS FOR NEURONS

To conclude this chapter we summarize the approach introduced above in Algorithm 3.1. For the simulation of neurons with their spatial expansion and Hodgkin-Huxley dynamics

**Algorithm 3.1** Adaptive computations for branched nerve equations

---

```

1: Initialize:  $t = 0$ ,  $dt = dt_s$ ,  $k = 0$ , make grid & refine uniform to  $start_{level}$ 
2: while  $t < T_{end}$  do
3:
4:   Compute discretized system on current grid
5:   Timestep  $t^{k+1} = t^k + dt$ : use adequate time-stepping scheme (e.g. backward Euler
      or Crank-Nicholson)
                                      $\Rightarrow v_h^{k+1}$ 
6:   Use current  $v_h^{k+1}$  solution for error-estimation:
7:
8:   Time: compute  $\|E_h^t\|$  using (3.27)
9:   if  $\|E_h^t\| > \tau_{large}$  then
10:      $dt = 0.5dt$ 
11:     if  $dt < dt_{min}$  then
12:        $dt = dt_{min}$ 
13:     end if
14:   end if
15:   if  $\|E_h^t\| < \tau_{small}$  then
16:      $dt = 2dt$ 
17:     if  $dt > dt_{max}$  then
18:        $dt = dt_{max}$ 
19:     end if
20:   end if
21:   if  $t < t_{syn}$  &  $(t + dt) > t_{syn}$  then
22:      $dt = \max\{dt_{syn}, dt\}$ 
23:      $t = t_{syn} - dt$ 
24:   end if
25:
26:   Space: compute  $e_s$  using (3.24) for each element of the actual grid
27:   if  $\sum e_s > TOL$  then
28:     Refine  $\tau_{fine}$  percent of grid elements with largest errors (until  $max_{level}$ )
29:   end if
30:   Coarsen  $\tau_{coarse}$  percent of grid elements with smallest errors (until  $min_{level}$ )
31:
32:    $k = k + 1$ 
33:
34: end while
35:
36: Values for the parameters used in simulations can be found in Appendix A.1.

```

---

good simulation techniques are required. For an implementation of a finite-element solver on non-uniform grids we showed a way to implement adaptive grid control in space and time. The adaption process is based on a-posteriori error estimates. We introduced them here for passive signal propagation on branched neurons.

The error estimator for spatial grid control is derived by a standard duality based approach. It turns out that the residual is a good measure for the error in space. For the step size control in time we introduced two parts. First, a heuristic measure for the error which measures the changes in the solution in time was derived. Second, an adaptive step size control for synaptic activities was introduced.

These adaptive grid controls in space and time allow efficient and accurate numerical solutions for simulating the dynamics of complete nerve cells as we will show in Chapter 5. But before we come to the simulations, we have a look at the third theoretical part of this thesis in the next chapter: the theory of equation-free computation methods.





## Chapter 4

# EQUATION-FREE SIMULATIONS: INTRODUCTION AND THEORY

*We think in generalities,  
but we live in detail.*

ALFRED N. WHITEHEAD

In order not only to simulate but also to analyze the dynamics of neuron networks with respect to changing connection parameters we need sophisticated simulation and analysis techniques. It turns out that equation-free methods are suitable for our problems. We adapt them to the needs for the analysis of the behavior of the OB network. Additionally, we interpret the equation-free time-stepping scheme new as an one-step method and prove a convergence theorem. Finally, we introduce basic techniques of numerical bifurcation analysis and show how they can be combined with the equation-free simulation method.

---

In this chapter we introduce a method for coarse-grained multiscale computations developed by I.G. Kevrekidis and coworkers: equation-free simulations [62]. The class of problems this method was developed for are high dimensional dynamical systems with fast components which are damped out after a short time, and slow components which are still present in the solution. Fast components arise from eigenvalues with large negative real parts. The active, slow components can arise from driving terms in non-autonomous systems or from eigenvalues of small magnitude. That means, the considered systems must have two sets of eigenvalues: one with very negative real parts and one close to the

origin. It is now assumed that these two sets are in suitable large distance from each other. This distance is called gap [113]. Normally problems of this type are solved by using implicit methods, where the resulting coupled nonlinear equations are solved using some approximation of the Jacobian of the system [47]. Equation-free simulation is, in contrast, a method which does not require any approximation of the Jacobian or any representation of its dominant subspace. A detailed introduction can be found in [62]. For more details on the theory of the method one may consider [48, 49, 61, 100]. This method was already applied successfully to different application fields as it can be seen in [58, 74, 75, 76, 78, 96, 105, 108, 115, 116]. A first application to neuron networks can be found in [66].

**T**his chapter is organized as follows. Section 4.1 gives the basic definitions, which are necessary to use this method. Then we give an overview about the literature where methods to bridge the gap between different scales of the considered problems are treated in Section 4.2. In Section 4.3 we describe the method of equation-free simulations consisting of a coarse time-stepper and a projection step to integrate the dynamics of the considered system on a coarse, macroscopic level numerically. This passage follows [48, 62]. In Section 4.4 we introduce a convergence theory for this numerical method and show assumptions under which the method converges to the exact solution for time-steps converging to zero.

In Section 4.5 and 4.6 we present an additional application field for the equation-free simulation techniques. We re-interpret the approach, which enables us to use it to investigate dependencies of macroscopic variables on independent parameters using equation-free Newton's method. This allows us to develop equation-free simulation techniques for traveling waves in Section 4.7 and perform equation-free numerical bifurcation analysis as introduced in Section 4.8.

## 4.1 BASIC DEFINITIONS

**W**e consider problems the dynamics of which is described mathematically by the following fine or microscopic equations

$$\dot{u} = f(u), \quad u \in \mathbb{R}^m, \quad m \gg 1, \quad (4.1)$$

with a start value  $u(t_0) = u_0$ . Additionally, we assume that a microscopic time-stepper is given, which means we have a numerical solver for Equation (4.1) of order  $O(\Delta t^k)$ . Although we talk in terms of ODEs here, equation-free simulations can also be used to analyze problems arising from the semi-discretization of PDEs [48] or discrete time-stepping models as our SRM network model for the olfactory bulb network.

We assume that the long-term dynamic of (4.1) is described only by a few components on a coarse, macroscopic level. Mathematically, this behavior can be interpreted using the theory of initial manifolds [25, 42, 113].

**DEFINITION 4.1.1** *Let  $H$  be a finite or infinite-dimensional Hilbert space.*

$$\dot{u} = f(u) \quad (4.2)$$

*is a dynamical system in  $H$ , with which we can associate the semigroup  $\{S(t)\}_{t \geq 0}$ , where  $S(t)$  is the mapping  $S(t) : u_0 \mapsto u(t)$ ,  $u(\cdot)$  denoting the solution of (4.2) satisfying  $u(0) = u_0$ . An **inertial manifold** of this system is a finite-dimensional Lipschitz manifold  $IM$  which enjoys the following properties:*

1.  *$IM$  is positively invariant for the semigroup, i.e.  $S(t)IM \subset IM \quad \forall t \geq 0$ .*
2.  *$IM$  attracts exponentially all orbits of (4.2).*

*An **inertial system** for (4.2) is the system obtained by restricting (4.2) to  $IM$ .*

Most criteria for the existence of inertial manifolds use so-called spectral gap conditions [25, 77, 97]. One considers general evolution equations of the form

$$\frac{du}{dt} + Au + \tilde{f}(u) = 0, \quad u \in H \quad (4.3)$$

where  $A$  is a positive operator with discrete spectrum and  $\tilde{f}$  is a nonlinear continuous mapping. For such a system there exists a criterion for the existence of initial manifolds [25], which we state here.

**LEMMA 4.1.2** *Let  $\lambda_1 \leq \lambda_2 \leq \dots$  denote the eigenvalues of  $A$ . Then it holds that if the spectral gap condition*

$$\lambda_{N+1} - \lambda_N \geq \frac{2M}{q} \left( (1+k)\lambda_{N+1}^\theta + \lambda_N^\theta \right), \quad 0 < q < 1, \quad (4.4)$$

*is fulfilled for some  $N$ , then there exists an inertial manifold. We have  $0 \leq \theta < 1$ ,  $M$  is a positive constant independent of  $t$  and  $k = \theta^\theta \int_0^\infty \xi^{-\theta} e^{-\xi} d\xi$  for  $\theta > 0$  and  $k = 0$  for  $\theta = 0$ .*

We assume that the long term dynamics of (4.1), i.e. the dynamics of the slow components after the fast components are damped, can be described by a low dimensional inertial manifold. By restricting (4.1) to this inertial manifold one obtains the inertial system

$$\dot{U} = F(U), \quad U \in \mathbb{R}^M, \quad (4.5)$$

with the so-called macroscopic or coarse variable  $U$ . We call the initial system (4.5) macroscopic or coarse equation and assume  $M \ll m$ . This states the main requirement for equation-free simulations:

**STATEMENT 4.1.3** *In equation-free simulations of high-dimensional systems, with a long term dynamics that can be defined in a low-dimensional space, explicit macroscopic equations are not needed, since the coarse dynamic is evaluated numerically. To be able to do that, we have to assume that the long term dynamics of (4.1) can be described by a low-dimensional initial system.*

An example for that situation is a model of the neuron network in the olfactory bulb. The microscopic equations are, for example, a Spike Response network of point neurons, as described in Chapter 2. Principal and independent component analysis of calcium-sensitive dye imaging experiments in the olfactory bulb of rats show that the network activity can be described with a small number of so-called modes [95]. We will see in Chapter 6 that one possibility to apply equation-free techniques for simulating the dynamics of the OB network is to interpret these PCA/ICA modes as coarse variables.

## 4.2 OVERVIEW OF EXISTING METHODS

We will see in detail in the next section that the main point of equation-free simulations is to bridge the different scales of the considered problems by “on demand” closure. This is a mainstream approach in current research and there are several numerical multiscale techniques known. In the context of large scale reactive flow computations Maas and Pope suggested the dimension reduction technique ILDM (Intrinsic Low-Dimensional Manifolds) [72, 73]. The ILDM is a dynamical system based approach, which does not require information concerning which reactions are to be assumed in partial equilibrium nor which species are assumed to be in steady states. Based on local eigenvector analysis, the method identifies the fast scales of the chemical reaction system. The only information needed to be able to do this are the detailed kinetics mechanism and the number of degrees of freedom required in the simplified scheme. In the original work the dimension of the reduction is kept constant throughout each computation. Deufelhard and Herroth suggested a mathematically correct and nevertheless cheap dimension monitor for the chemistry part [33, 34].

Philips and coworkers developed a quasi-continuum method in the context of material sciences [87]. Kinematic-theory based solvers were proposed by Xu and Prendergast [123]. To get the Euler and Navies-Stokes solutions from gas-kinetic theory, they developed a numerical approach to the Bhatnagar-Gross-Kook model [18] of the Boltzmann equations.

Chorin, Kast and Kupferman developed the optimal predictor method [24]: here the average solution of problems that are too complicated for adequate resolution, but where information about the statistics of the solution is available, is computed. The method involves computing average derivatives by interpolation based on linear regression.

All these methods have in common, that special structures of the considered problems, in addition to the existence of a low dimensional description of the dynamics, are required.

Equation-free simulations only require the existence of a low dimensional description of the system's dynamics.

### 4.3 EQUATION-FREE SIMULATIONS IN TIME

The best available description of a system often comes at a fine level with fine, microscopic equations describing the detailed dynamics of the system like in equation (4.1). This system is assumed to include fast and slow components. The fast components are damped out after a short time, while the slow ones are still present in the solution. It often occurs, that a microscopic time-stepper for equation (4.1) exists, i.e. one has a numerical solver for the fine dynamics. We assume in our theoretical considerations, that a one-step method

$$u(t + \Delta t) = u(t) + \Delta t \Phi^f(t, u(t), \dot{u}(t), \dots; \Delta t) \quad (4.6)$$

of the order  $O(\Delta t^k)$ ,  $k \geq 1$  with the operating function  $\Phi^f$  is used. In many applications one wants to solve (4.1) for long or even infinite times, but applying the microscopic time-stepper is very computation intensive, e.g. due to size of the problem or because nonlinearities in the system require small time steps. And in many applications, even if the best description of the dynamics is given at a fine level, the questions asked are at a much coarser macroscopic level. Traditional modeling techniques start by deriving macroscopic evolution equations from microscopic models. But in several applications a closed form of the macroscopic equations is not available. We introduce an approach which enables numerical simulations in that case: I.G. Kevrekidis and coworkers developed and validated a mathematically inspired computation technique that allows the modeler to perform macroscopic tasks acting on the microscopic models directly. This approach is called “equation-free” approach, since it circumvents the step of obtaining closed macroscopic descriptions [62].

One assumes that the long term dynamics of (4.1) can be described by a low-dimensional inertial manifold. That means the dynamics of the slow components, as the fast components are damped, can be described by a coarse variable  $U$  describing the dynamics on the inertial manifold of the dynamical system (4.1). Its time course is described by the inertial system (4.5), where the explicit form of the right-hand side function  $F$  is in general unknown, but we know/assume that it exists. Furthermore, we assume  $M \ll m$ . This is the main point of this method: the macroscopic, coarse equation (4.5) is not derived in a closed form, and neither a specific spatial structure of the underlying dynamical system nor explicit macroscopic equations are needed. We only assume that the long-term dynamics of (4.1) can be described by a low-dimensional initial system to evaluate it efficiently numerically.

The following description of the equation-free simulation follows closely the report [62]. Given the situation described above we assume that it is too expensive to simulate the whole

system (4.1), i.e. we have the following problem:

**PROBLEM 4.3.1** *We want to simulate the coarse equation (4.5) for large or infinite times, but we are only able to simulate the fine system (4.1) for short times using the fine time stepper (4.6).*

### 4.3.1 COARSE TIME-STEPPER

To reduce Problem 4.3.1 we introduce two routines: lifting and restricting. They enable us to derive macroscopic values  $U$  belonging to a microscopic value  $u$  via restricting. In the case of lifting, consistent fine values are computed for a given coarse value. Lifting is in general not unique and it is an important part of the modeling to choose a suitable lifting routine for a given problem [61].

**DEFINITION 4.3.2** *Let  $l : \mathbb{R}^M \rightarrow \mathbb{R}^m$  be a  $L$ -continuous function. We define  $l$  in such a way that for a given coarse quantity consistent fine quantities  $l(U(t)) = u(t)$  for the fine system (4.1) are computed. This function is called **lifting**. Furthermore let  $r : \mathbb{R}^m \rightarrow \mathbb{R}^M$  be a linear function, which gives the coarse quantity connected to a given fine value, i.e.  $r(u(t)) = U(t)$ . We call this routine **restricting**.*

In order to make these routines reasonable, the following assumption has to hold.

**ASSUMPTION 4.3.3** *We claim that*

$$r \circ l = Id.$$

With the lifting and the restricting routines a so-called coarse time-stepper (see Figure 4.1) can be applied to reduce Problem 4.3.1. By applying lifting on a given macroscopic start value we get a consistent fine value. We apply the given time-stepping scheme to perform a small solution step on the fine level. Then we restrict the solution to the macroscopic level, i.e.

$$U(t + \Delta t) = r \left( l(U(t)) + \Delta t \Phi^f(l(U(t)); \Delta t) \right)$$

By connecting the coarse level to the fine level equations and time-stepping scheme, we reduced Problem 4.3.1 to:

**PROBLEM 4.3.4** *We want to simulate the coarse system (4.5) for large or infinite times, but we are only able to simulate it for short discrete times  $\Delta t$ .*

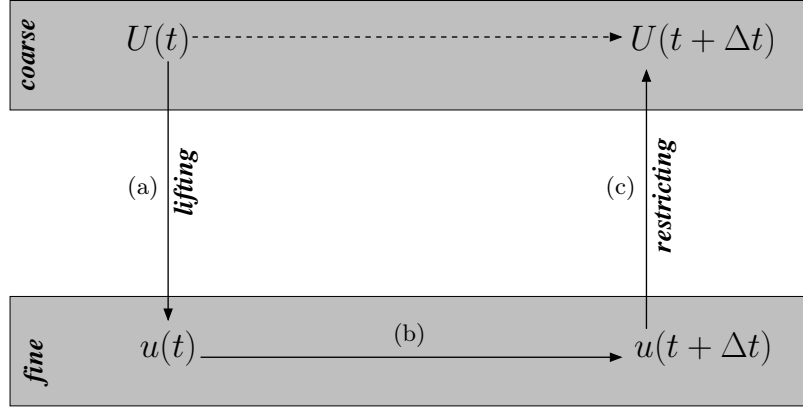


Figure 4.1: *The coarse time-stepper. Since macroscopic equations are not available, lifting is used to derive a consistent fine value in (a) for a given coarse value. (b) A small simulation step is performed on the fine equations using the fine time-stepper (4.6). By using restricting in (c) the coarse variable is finally derived. This process can be seen as a “black box” for performing small coarse time steps.*

#### 4.3.2 COARSE PROJECTIVE INTEGRATION

To solve Problem 4.3.4 we use the restricting procedure not only to evaluate  $U(t + \Delta t)$ , but also its derivatives needed to apply a time-stepping scheme, e.g. forward Euler, on the coarse level. Therefore, we are able to perform a coarse projection step using an one-step method of the order  $O(\Delta T^K)$

$$U(t + \Delta t + \Delta T) = U(t + \Delta t) + \Delta T \Phi^c \left( t + \Delta t, U(t + \Delta t), \dot{U}(t + \Delta t), \dots; \Delta T \right), \quad (4.7)$$

with the operation function  $\Phi^c$ . In the case of an Euler step, we have  $U(t + \Delta t + \Delta T) = U(t + \Delta t) + \Delta T \cdot \dot{U}(t + \Delta t)$ . The important idea here is that  $U$  and  $\dot{U}$  are not calculated by evaluating (4.5) but by applying the restricting procedure  $r$  to calculate them based upon the fine quantities  $u$ . That means, in the simple case of using forward Euler as course time-stepping scheme, we get

$$U(t + \Delta t + \Delta T) = r(u(t + \Delta t)) + \Delta T \frac{r(u(t + \Delta t + \tau)) - r(u(t + \Delta t))}{\tau}, \quad \tau < \Delta t,$$

by representing the derivative  $\dot{U}(\cdot) = \frac{\partial U}{\partial t}(\cdot)$  by finite differences. This leads to the following statement, which summarizes the abilities of equation-free simulations.

**STATEMENT 4.3.5 (EQUATION-FREE SIMULATIONS)** *The equation-free approach enables us to simulate the coarse behavior of high dimensional systems by only evaluating small bursts of the complete dynamics.*

We close this section with a remark on the wording used here. In the projection step we perform an extrapolation of the coarse variables using evaluation of the microscopic states. But nevertheless the method of projective integration should not be confused with “extrapolation methods” [21], which is an unrelated class of numerical methods.

#### 4.4 CONVERGENCE OF EQUATION-FREE SIMULATIONS

In the following, we investigate the convergence properties of the equation-free simulation method. Therefore, we divide the solution interval of the coarse dynamical system (4.5)  $[t_0, t_0 + T]$  into subintervals

$$t_0 < t_1 < \dots < t_k < \dots < t_N = t_0 + T. \quad (4.8)$$

In each point  $t_k$  the exact solution of (4.5) is denoted by  $U_k = U(t_k)$  and the solution of the equation-free simulation is denoted by  $\eta_k$ . The solution method consists of the following four steps to perform a time-step starting at the numerical solution in the  $k$ -th step  $\eta_k$

1. Lifting:  $l(\eta_k)$
2. Fine time step:  $l(\eta_k) + \Delta t \Phi^f(l(\eta_k); \Delta t)$
3. Restricting:  $r(l(\eta_k) + \Delta t \Phi^f(l(\eta_k); \Delta t)) =: \bar{\eta}_k$
4. Projection:  $\bar{\eta}_k + \Delta T \Phi^c(\bar{\eta}_k; \Delta T) =: \eta_{k+1}$ .

We show that it converges to the exact solution  $U(t)$  of (4.5), i.e the error during the integration tends to zero, if the integration steps  $\Delta t$  and  $\Delta T$  converge to zero. To do so, we show how the classical theory of one-step methods can be applied in the equation-free context.

In numerical analysis one-step methods are a standard technique to solve initial value problems numerically [93, 111]. We will interpret the equation-free method in this context and use well known convergence results to derive a convergence theorem.

In order to solve a given initial value problem

$$\begin{aligned} \dot{y} &= f(t, y), & t \in I = [t_0, t_0 + T] \\ y(t_0) &= y_0, & y \in \mathbb{R}^d, \end{aligned} \quad (4.9)$$

with the exact solution  $y(t)$ , one discretizes the time-interval  $I$  as in (4.8). On this time-grid we are able to define an one-step method starting with  $\eta_0$  and

$$\begin{aligned} \eta_{k+1} &= \eta_k + \Delta t_k \Phi(t_k, \eta_k; \Delta t_k) \\ t_{k+1} &= t_k + \Delta t_k, \end{aligned} \quad (4.10)$$



with  $\Delta t_k := t_k - t_{k-1}$ . In the equation-free context, it is convenient to split the operation function  $\Phi$  in (4.10) in two parts, i.e.

$$\begin{aligned}\eta_{k+1} &= \eta_k + \Delta t_k \Phi^1(t_k, \eta_k; \Delta t_k) \\ &\quad + \Delta T_k \Phi^2(t_k + \Delta t_k, \underbrace{\eta_k + \Delta t_k \Phi^1(t_k, \eta_k; \Delta t_k)}_{:= \bar{\eta}_k}; \Delta T_k) \\ t_{k+1} &= t_k + \Delta t_k + \Delta T_k.\end{aligned}\tag{4.11}$$

For this “two-step” method one defines the truncation error, where one for simplicity sets  $\Delta t_k = \Delta T_k = \frac{\Delta t}{2}$ ,  $\forall k = 0, 1, 2, \dots, N-1$ .

**DEFINITION 4.4.1** *For the two step method (4.11) the **truncation error** is defined as*

$$\tau_k := \Delta t^{-1}(y_{k+1} - y_k) - \left[ \Phi^1\left(t_k, y_k; \frac{\Delta t}{2}\right) + \Phi^2\left(t_k + \frac{\Delta t}{2}, \bar{y}_k; \frac{\Delta t}{2}\right) \right], \tag{4.12}$$

with  $\bar{y}_k := y(t_k + \frac{\Delta t}{2})$ .

The truncation error shows how good the exact solution of (4.9) fulfills the equation of the two-step method. This is a measure for the performance of the numerical method. Hence, one defines:

**DEFINITION 4.4.2** *The two-step method (4.11) is called **consistent**, if*

$$\max_{t_k \in I} \|\tau_k\| \rightarrow 0, \text{ for } \Delta t \rightarrow 0.$$

There exists an simple criterion for consistency.

**LEMMA 4.4.3** *A two-step method is consistent, if and only if*

$$\lim_{\Delta t \rightarrow 0} \Phi(t, x; \Delta t) = f(t, x), \quad \forall t \in I, x \in \mathbb{R}^d$$

with  $\Phi(t, x; \Delta t) = \Phi^1(t, x; \frac{\Delta t}{2}) + \Phi^2(t + \frac{\Delta t}{2}, x + \frac{\Delta t}{2} \Phi^1(t, x; \frac{\Delta t}{2}); \frac{\Delta t}{2})$ .

Finally, we need an additional definition in order to be able to perform convergence analysis for the equation-free method.

**DEFINITION 4.4.4** *A two-step method is called **Lipschitz-continuous (L-continuous)**, if the operation functions satisfy an uniform Lipschitz condition*

$$\|\Phi^{1,2}(t, x, \Delta t) - \Phi^{1,2}(t, \tilde{x}, \Delta t)\| \leq L_{1,2} \|x - \tilde{x}\|, \quad \forall x, \tilde{x} \in \mathbb{R}^d, t \in I.$$

With this definitions we are able to formulate a convergence theorem for two-step methods, based on the standard convergence theorem for one-step methods [93].

**THEOREM 4.4.5** *Let a given two-step method (4.11) with the operation functions  $\Phi^1$  and  $\Phi^2$  be Lipschitz-continuous with the constants  $L_1$  and  $L_2$  and consistent. In the case that  $\|y_0 - \eta_0\| \rightarrow 0$ , we get*

$$\max_{t_k \in I} \|y_k - \eta_k\| \rightarrow 0, \text{ for } \Delta t \rightarrow 0.$$

*And the following a-priori error estimate holds*

$$\|y_k - \eta_k\| \leq e^{(2(L + \frac{\Delta t}{2}L')(t_k - t_0))} \left\{ \|y_0 - \eta_0\| + \Delta t \sum_{\nu=1}^k \|\tau_\nu\| \right\},$$

with  $L = L_1 + L_2$  and  $L' = L_1 L_2$ .

**Proof** We introduce a difference operator  $D_h$  for the grid functions  $\eta = \{\eta_k\}_{1 \leq k \leq N}$  by

$$(D_h \eta)_k := \Delta t^{-1}(\eta_k - \eta_{k-1}) - \Phi(t_k, \eta_k, \Delta t),$$

with  $\Phi$  as in Lemma 4.4.3. For two grid functions  $y = \{y_k\}_{1 \leq k \leq N}$  and  $z = \{z_k\}_{1 \leq k \leq N}$  we get by subtracting the two equations

$$\begin{aligned} (D_h y)_k &= \Delta t^{-1}(y_k - y_{k-1}) - \Phi(t_k, y_k, \Delta t) \\ (D_h z)_k &= \Delta t^{-1}(z_k - z_{k-1}) - \Phi(t_k, z_k, \Delta t) \end{aligned}$$

the equation

$$y_k - z_k = y_{k-1} - z_{k-1} + \Delta t \{ \Phi(t_k, y_k, \Delta t) - \Phi(t_k, z_k, \Delta t) + (D_h y - D_h z)_k \}.$$

Hence,

$$\|y_k - z_k\| \leq \|y_{k-1} - z_{k-1}\| + \Delta t \left\{ \left( L + \frac{\Delta t}{2} L' \right) \|y_k - z_k\| + \|(D_h y - D_h z)_k\| \right\}$$

with  $L = L_1 + L_2$  and  $L' = L_1 L_2$ . By applying this inequality recursively for  $\nu = k, \dots, 1$  one gets

$$\|y_k - z_k\| \leq \|y_0 - z_0\| + \left( L + \frac{\Delta t}{2} L' \right) \sum_{\nu=0}^k \Delta t \|y_\nu - z_\nu\| + \sum_{\nu=0}^k \Delta t \|(D_h y - D_h z)_\nu\|.$$

Now one applies the discrete Gronwall's lemma and gets

$$\|y_k - z_k\| \leq e^{2(L + \frac{\Delta t}{2} L')(t_k - t_0)} \left\{ \|y_0 - z_0\| + \sum_{\nu=0}^k \Delta t \|(D_h y - D_h z)_\nu\| \right\}. \quad (4.13)$$

We have

$$D_h y = \tau \text{ and } D_h \eta = 0, \quad \tau = \{\tau_k\}_{1 \leq k \leq N}$$

and by inserting this in Equation (4.13) the claim of the theorem is proven.  $\blacksquare$

To apply Theorem 4.4.5 to the equation-free method, we have to show two properties: first that the equation-free method is consistent and second that it is L-continuous. Before we do so, we state the equation-free method in the nomenclature of one- or two-step methods. For lucidity we omit the dependency of  $t_k$  in the operation functions. We have

$$\begin{array}{ccc}
 \text{fine} & l(\eta_n) & \rightarrow & l(\eta_n) + \frac{\Delta t_k}{2} \Phi^f(l(\eta_n); \Delta t_k) \\
 & \uparrow & & \downarrow \\
 \text{coarse} & \eta_k & \rightarrow & \underbrace{r(l(\eta_k) + \frac{\Delta t_k}{2} \Phi^f(l(\eta_k); \Delta t_k))}_{:= \bar{\eta}_k} \rightarrow \bar{\eta}_k + \Delta T_k \Phi^c(\bar{\eta}_k; \Delta T_k)
 \end{array} \quad (4.14)$$

with consistent and L-continuous one-step methods on the microscopic and on the macroscopic level. Now we are able to write the equation-free processing as

$$\begin{aligned}
 \eta_{k+1} &= \bar{\eta}_k + \Delta T_k \Phi^c(\bar{\eta}_k; \Delta T_k) \\
 &= r \left( l(\eta_k) + \Delta t_k \Phi^f(l(\eta_k); \Delta t_k) \right) + \Delta T_k \Phi^c(\bar{\eta}_k; \Delta T_k).
 \end{aligned}$$

For the convergence analysis we choose  $\Delta t_k = \Delta T_k = \frac{1}{2} \Delta t$ . By using that  $r(\cdot)$  is assumed to be linear, see Definition 4.3.2, and Assumption 4.3.3, it holds

$$\eta_{k+1} = \eta_k + \Delta t \underbrace{\frac{1}{2} \left( r(\Phi^f(l(\eta_k); \frac{1}{2} \Delta t)) + \Phi^c(\bar{\eta}_k; \frac{1}{2} \Delta t) \right)}_{:= \Phi(\eta_k, \Delta t)}, \quad (4.15)$$

with the operation function  $\Phi(\eta_k, \Delta t)$ . First, it is proven that  $\Phi(\eta_k, \Delta t)$  is consistent by applying Lemma 4.4.3. We have

$$\begin{aligned}
 r(\Phi^f(l(\eta_k); \frac{1}{2} \Delta t)) &\rightarrow r(f(l(\eta_k))), \text{ for } \Delta t \rightarrow 0 \\
 &\underbrace{=}_{(A_1)} F(\eta_k, t),
 \end{aligned}$$

where the first step holds, since the one-step method used on the fine level is assumed to be consistent.  $(A_1)$  is an assumption, which will hold in praxis only approximately. At this point the convergence of the microscopic state to a slow dimensional manifold, compare Figure 4.2, comes into play: if the dynamics of the considered dynamical system (4.1) has completely converged to the initial system (4.5) assumption  $(A_1)$  holds. To achieve that, we will perform in praxis several fine steps, which will lead to fast convergence, since initial manifolds, if they exist, attract all orbits exponentially, compare Definition 4.1.1.

For the second term in Equation (4.15) we assume that the coarse one-step method is consistent and we have  $\bar{\eta}_k \rightarrow \eta_k$  for  $\Delta t \rightarrow 0$ , i.e.  $\Phi^c(\bar{\eta}_k; \frac{1}{2} \Delta t) \rightarrow F(\eta_k, t)$  for  $\Delta t \rightarrow 0$ . Therefore, we get

$$\Phi(\eta_k, \Delta t) \rightarrow F(\eta_k, t).$$

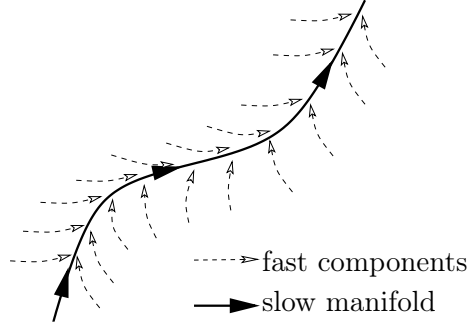


Figure 4.2: *Convergence to the inertial manifold. To be able to use the equation-free approach it is necessary that the dynamics of the complete system converge quickly to the manifold described by the dynamics of the considered coarse variable as it is shown schematically here.*

Hence, it is shown that the equation-free method is consistent.

In the next step, we show that the equation-free method is L-continuous in the sense of Definition 4.4.4. We have  $\Phi^1(\eta_k; \Delta t) = r(\Phi^f(l(\eta_k); \Delta t))$  and  $\Phi^2(\bar{\eta}_k; \Delta t) = \Phi^c(\bar{\eta}_k; \Delta t)$ . For  $\Phi^1$  we get

$$\begin{aligned} \|\Phi^1(x; \Delta t) - \Phi^1(y; \Delta t)\| &= \|r(\Phi^f(l(x); \Delta t)) - r(\Phi^f(l(y); \Delta t))\| \\ &\leq L_r L_f L_l \|x - y\|, \quad \forall x, y \in \mathbb{R}^M \end{aligned}$$

since  $r$  and  $l$  are L-continuous, see Definition 4.3.2 and  $\Phi^f$  is a L-continuous method on the microscopic level. Furthermore, we get

$$\begin{aligned} \|\Phi^2(x; \Delta t) - \Phi^2(y; \Delta t)\| &= \|\Phi^c(x; \Delta t) - \Phi^c(y; \Delta t)\| \\ &\leq L_c \|x - y\|, \end{aligned}$$

if the one-step method on the coarse level is assumed to be L-continuous. By applying Theorem 4.4.5, we just proved the following convergence theorem for the equation-free method.

**THEOREM 4.4.6 (CONVERGENCE OF THE EQUATION-FREE METHOD)** *Consider the equation-free method to solve an initial system*

$$\dot{U} = F(u), \quad U \in \mathbb{R}^M. \quad (4.16)$$

*belonging to the dynamical system*

$$\dot{u} = f(u), \quad u \in \mathbb{R}^m, \quad m \gg M.$$

Apply the following time-stepping scheme to solve equation (4.16) with the start value  $U(t_0) = U_0 = \eta_0$ ,  $r : \mathbb{R}^m \rightarrow \mathbb{R}^M$ ,  $l : \mathbb{R}^M \rightarrow \mathbb{R}^m$  as in Definition 4.3.2, and

$$\eta_{k+1} = \eta_k + \frac{1}{2}\Delta t \left( r(\Phi^f(l(\eta_k); \frac{1}{2}\Delta t)) + \Phi^c(\bar{\eta}_k; \frac{1}{2}\Delta t) \right),$$

with  $\bar{\eta}_k = r(l(\eta_k) + \frac{\Delta t}{2}\Phi^f(l(\eta_k); \Delta t))$ . Assume  $\Phi^f$  and  $\Phi^c$  to be consistent,  $L$ -continuous operating functions of time-stepping schemes on  $\mathbb{R}^m$  and on  $\mathbb{R}^M$ . If

$$r(f(l(\eta_k), t_k)) = F(\eta_k, t_k), \quad \forall \eta_k, t_k, \quad k = 0, 1, 2, \dots, N,$$

we get

$$\max_{t_k \in I} \|U_k - \eta_k\| \rightarrow 0, \quad \text{for } \Delta t \rightarrow 0.$$

The equation-free method, which we investigated theoretically here, will not only be used for pure simulation but also to analyze the dynamics of coarse initial systems by applying dynamical system theory. To be able to do so, we generalize the approach in the next sections.

## 4.5 EQUATION-FREE NEWTON'S METHOD

In several applications we are interested in finding stationary states of the macroscopic equations (4.5), i.e.  $\dot{U}(t) = 0$ . There are two possibilities to determine the stationary states in general: one can integrate (4.5) until the stationary state is reached. Or one applies Newton's method to solve

$$F(U) = 0.$$

With the first approach one will find stable stationary states, but long computation times must be expected and unstable stationary states will not be reached. The second approach is also able to detect unstable stationary states and is due to the good convergence properties of Newton's method fast, if good start values are available [111]. As in the case of the coarse projective integration all necessary evaluations of the macroscopic variables  $U$  and the derivatives will be done by integrating the fine system (4.1) for short bursts. The single steps of this process are shown in Algorithm 4.1, where  $TOL$  is a user defined tolerance for which one wants to reach  $\|F(U^k)\| \leq TOL$ , i.e. the numerical test for  $F(U^k) = 0$ . Note again that  $U$  is not computed by evaluating a closed form of the coarse equation (4.5) at the different points in time, but by restricting the connected fine states from the fine equation (4.1).

**STATEMENT 4.5.1 (EQUATION-FREE NEWTON'S METHOD)** *One is able to compute stationary states of the coarse dynamics by evaluating only small bursts of the complete equations of the system by applying Algorithm 4.1.*

---

**Algorithm 4.1** Equation-free Newton's method

---

- 1: Start:  $U^0$
- 2: **while**  $\|F(U^k)\| > TOL$  **do**
- 3:   Perform a Newton step

$$U^{k+1} = U^k + \frac{\partial F}{\partial U}(U^k)^{-1} F(U^k)$$

by approximating the Jacobian, in the one dimensional case as

$$\frac{\partial F}{\partial U}(U^k) \approx \frac{F(U^k + \Delta U) - F(U^k)}{\Delta U^k}.$$

$F(U^k)$  is approximated by using finite differences, i.e.  $F(U^k) = \frac{U(t_k + \tau) - U(t_k)}{\tau}$ .

- 4: **end while**
- 

## 4.6 DEPENDENCIES ON INDEPENDENT PARAMETERS

In the case of simulating neuron networks in the olfactory bulb we are not only interested in the time course of the dynamics. Other interesting questions are how network parameters influence the network dynamics. One purpose of the olfactory bulb network is to perform contrast enhancement, to be able to discriminate similar odors. One wants to investigate which parameters, like the strength of synapses or the radius of interaction between single neurons, influence this ability. With this motivation in mind we develop a way to use equation-free simulation techniques to explore the dependence of macroscopic variables on independent parameters. The result of this development can be formulated as in the following statement.

**STATEMENT 4.6.1 (EQUATION-FREE PARAMETER STUDIES)** *The equation-free techniques allow to perform parameter studies on the coarse level of the dynamics, if it exists. The considered high-dimensional fine system has to be evaluated only for small bursts.*

We are interested in the stationary state of the macroscopic dynamical system (4.5). To find the stationary state, we use an equation-free Newton's method (see Section 4.5).

First we consider one independent parameter. That means we have a coarse equation

$$\dot{U} = F(U, \mu), \quad U \in \mathbb{R}^M, \mu \in \mathbb{R} \quad (4.17)$$

with the independent parameter  $\mu$ . The function  $F$  can be highly nonlinear. The influence of  $\mu$  in the fine dynamics is given by Equation (4.1), where  $f = f(u, \mu)$  depends also on  $\mu$ . The equation-free simulation for investigating the dynamics in a parameter range  $\mu \in [\mu^s, \mu^e]$  is described in Algorithm 4.2. Besides the projection step in time, one also

performs a projection step in the parameter space. This leads to reasonable start values for Newton's method and, therefore, to good convergence properties.

---

**Algorithm 4.2** Parameter study: one parameter

---

- 1: Start:  $\mu = \mu^s$
- 2: **while**  $\mu < \mu^e$  **do**
- 3:   Use **Equation-free Newton's method** (see Section 4.5) to derive stationary state  $U(\mu)$  and  $U(\mu + \Delta\mu)$  of the system (4.17) for  $\mu$  and  $\mu + \Delta\mu$ .
- 4:   **Project:** Perform a large step  $\Delta\bar{\mu}$  using forward Euler (any other explicit numerical method can be used):

$$U(\mu + \Delta\mu + \Delta\bar{\mu}) = U(\mu + \Delta\mu) + \Delta\bar{\mu} \frac{U(\mu + \Delta\mu) - U(\mu)}{\Delta\mu}.$$

- 5:   Set  $\mu = \mu + \Delta\mu + \Delta\bar{\mu}$ .
  - 6: **end while**
- 

In the case of several independent parameters

$$\dot{U} = F(U, \mu_1, \mu_2, \dots, \mu_p), \quad U \in \mathbb{R}^M, \mu_i \in \mathbb{R}, 1 \leq i \leq p \quad (4.18)$$

we apply the techniques developed for one parameter, for each parameter. The resulting procedure is linked to the gap-tooth scheme for equation-free computations in space and time [62]. The single steps to explore the dependency of a coarse variable from two parameters in an area  $\mu_{1,2} \in [\mu_{1,2}^s, \mu_{1,2}^e]$  are shown in Algorithm 4.3. For more parameters this approach can be generalized in higher-dimensional space directly.

---

**Algorithm 4.3** Parameter study: two parameter

---

- 1: Start:  $\mu_1 = \mu_1^s, \mu_2 = \mu_2^s$ .
  - 2: **while**  $\mu_2 < \mu_2^e$  **do**
  - 3:   Perform equation-free dependence analysis for  $\mu_1 \in [\mu_1^s, \mu_1^e]$  for a constant  $\mu_2$  using Algorithm 4.2.
  - 4:   For each value  $U(\mu_1^k, \mu_2)$ , where  $\mu_1^k$  is a value where  $U(\mu_1^k, \mu_2)$  was derived in step (2.) perform a coarse step in  $\mu_2$  direction.
  - 5:   Update  $\mu_2 = \mu_2 + \Delta\mu_2 + \Delta\bar{\mu}_2$ .
  - 6: **end while**
- 

## 4.7 EQUATION-FREE METHODS FOR TRAVELING WAVES

In the olfactory system traveling-waves-like structures are found in experiments [44]. We want to investigate which network parameters are responsible for this behavior. For this

aim we use equation-free methods for traveling waves as introduced in this section. A traveling wave solution of a dynamical system is defined as a function moving with constant velocity in a constant direction while retaining a fixed shape [36].

#### 4.7.1 TRAVELING WAVE VARIABLE

We introduce a method using homoclinic orbits to investigate traveling waves in the following. This method is very well known in the context of dynamical systems [109]. We assume that the coarse system (4.5) has a traveling wave solution for a given start value  $U_0$ . Traveling wave systems are e.g. nonlinear reaction-diffusion equations like the Hodgkin-Huxley equations introduced in Section 2.4.2. One reduces these systems by introducing a traveling wave variable  $\xi$ . In the one-dimensional case, with the position variable  $x$  and  $t$  denoting time,  $\xi$  is defined as

$$\xi = x - \lambda t, \quad (4.19)$$

where  $\lambda$  is the propagation velocity of the traveling wave. The solution of Equation (4.5) has now the form

$$U(x, t) = \tilde{U}(\xi) = \tilde{U}(x - \lambda t).$$

It holds

$$\begin{aligned} \frac{\partial U}{\partial t} &= \frac{\partial \tilde{U}}{\partial \xi} \frac{\partial \xi}{\partial t} = -\lambda \frac{\partial \tilde{U}}{\partial \xi} \\ \frac{\partial U}{\partial x} &= \frac{\partial \tilde{U}}{\partial \xi} \frac{\partial \xi}{\partial x} = \frac{\partial \tilde{U}}{\partial \xi}. \end{aligned}$$

By denoting  $' = \frac{\partial}{\partial \xi}$  and omitting the tilde, we get

$$-\lambda U' = F(U, U', \dots). \quad (4.20)$$

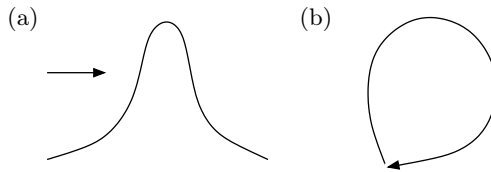


Figure 4.3: A traveling wave (a) results in a homoclinic orbit (b) by introducing the traveling wave variable  $\xi$ .

This means, a reaction-diffusion equation is reduced to an ODE-system. The traveling wave solution of the PDE is given, after transformation to an ODE system (4.20), as a homoclinic orbit, compare Figure 4.3. This can be seen by keeping  $t$  fixed and changing  $x$  for changing  $\xi$ . A homoclinic orbit is a stationary point connected by a trajectory with itself. The trajectory is formed by the intersection of the unstable and the stable manifold of this point. The development of the homoclinic orbit for changing parameters gives



insights into the reasons why traveling waves emerge in certain parameter regions and why they are not seen in other regimes.

Before we are able to use the equation-free methods to analyze the traveling wave system we have to determine the traveling wave velocity  $\lambda$  in order to be able to perform the reduction described above. A way of doing this is the so-called template fitting [98]. Template fitting is a method that allows to remove variables associated with symmetries in systems with continuous symmetries. Given an ensemble of data  $u(x, t)$ , one first chooses a template  $u_0(x)$ . After that one determines a symmetry variable  $c(t)$ , so that

$$\min_{c(t)} \|u(x - c(t), t) - u_0(x)\|. \quad (4.21)$$

That means  $u(x, t)$  is shifted by the amount  $c(t)$  in a way that the data matches up best with the preselected template. Let, for example,  $u(x, t)$  be a  $2\pi$ -periodic function in  $x$ . Equation (4.21) is then equivalent to

$$(u(x, t), u_0(x + c(t))) = 0, \quad (4.22)$$

where  $(\cdot, \cdot)$  denotes the standard inner product on  $L^2[0, 2\pi]$ . If  $c(t)$  solves (4.22), then assuming differentiability, one has a critical point

$$\partial_c (u(x, t), u_0(x + c(t))) = 0, \quad (4.23)$$

which is equivalent to

$$(u(x, t), u'_0(x + c)) = 0, \text{ i.e. } (u(x - c, t), u'_0(x)) = 0. \quad (4.24)$$

Equation (4.24) is used to determine the shift amount  $c(t)$  when template fitting is applied. By dividing  $c(t)$  by  $t$ , we get the traveling wave velocity  $\lambda$ .

#### 4.7.2 EQUATION-FREE TEMPLATE FITTING

**T**o use template fitting in the equation-free context of one-dimensional traveling waves we introduce a template  $u_0(x)$ , which is a snap-shot of the traveling wave. One should choose a template where the shape of the traveling wave is fully developed. Otherwise, artifacts can appear due to boundary effects. Furthermore, we introduce the template fitting variable  $c(t) \in \mathbb{R}$ , which describes how much the state  $u(x, t)$  has to be shifted to be in alignment with the template  $u_0(x)$ , as defined in Equation (4.21). We choose  $c(t)$  as a coarse variable and apply the coarse time-stepper with a projection step as introduced in Section 4.3.1 by performing Algorithm 4.4. This allows us to investigate traveling wave systems without deriving the explicit traveling wave ODE like in Equation (4.20), but just by determining the velocity of the traveling wave numerically.

---

**Algorithm 4.4** Equation-free Template Fitting

---

1: Perform (several) fine steps

$$\Rightarrow u(x, t), u(x, t + \Delta t).$$

2: **Restricting:** Compute the coarse variable  $c(t)$  and  $c(t + \Delta t)$  by applying a template fitting routine.

3: Perform a coarse step using forward Euler

$$\Rightarrow c(t + dt + dT) = c(t + \Delta t) + dT \cdot \dot{c}(t + \Delta t).$$

4: **Lifting:** Compute the new  $u(x, t)$  by

$$u(x, t) = u_0(x + c(t)).$$


---

## 4.8 NUMERICAL BIFURCATION ANALYSIS

As last part of this chapter, we state results of (numerical) bifurcation analysis, which we will need for our numerical investigations later. The results are taken from [23, 65, 109]. One of the great advantages of the equation-free approach is that it can be combined directly with the techniques introduced here [115]. Again the coarse quantities, e.g.  $U$  and  $F(U)$ , are derived numerically using restricting and lifting combinations. We consider a coarse dynamical system, which is dependent on an independent parameter  $\mu$

$$\dot{U} = F(U, \mu), \quad U \in \mathbb{R}^M, \mu \in \mathbb{R}^p. \quad (4.25)$$

For systems of this form so-called bifurcation points may occur. A bifurcation point is defined in the following way.

**DEFINITION 4.8.1** *A dynamical system given by (4.25) is said to undergo a **bifurcation** at a parameter value  $\mu = \mu_0$  if in any neighborhood of  $\mu_0 \in \mathbb{R}^p$  there is a  $\mu$ -value containing dynamics that are not topologically equivalent to those at  $\mu_0$ .*

*A **bifurcation diagram** is a plot of (some measure of) the invariant sets of (4.25), i.e. the subsets of phase space which are invariant under the dynamics of (4.25), against a single bifurcation parameter  $\mu$ , indicating stability.*

The Hartman-Grobman Theorem [23] shows that hyperbolic equilibria are structurally stable. But also the converse holds. Non-hyperbolic equilibria are not structurally stable and hence generically lead to bifurcations. For  $p = 1$  it can occur in Equation (4.25) that the hyperbolicity of equilibria is violated if, on one hand, a simple real eigenvalue of  $F_U$  approaches zero. In this case a saddle-node bifurcation occurs. On the other hand, it is possible that a pair of simple complex eigenvalues of  $F_U$  crosses the imaginary matrix while the parameter  $\mu$  is changing. Then a Hopf bifurcation occurs.

#### 4.8.1 SADDLE-NODE BIFURCATION

The saddle-node or fold bifurcation has the following normal form

$$\dot{U} = \mu + U^2 = F(U, \mu), \quad U, \mu \in \mathbb{R}. \quad (4.26)$$

At  $\mu = 0$  the system (4.26) has a non-hyperbolic equilibrium at  $U = 0$  with  $F_U(0, 0) = 0$ . In the following we investigate under which conditions an one-dimensional system (4.25) undergoing a saddle-node bifurcation with an equilibrium at  $U = 0$  with  $F_U(0, 0) = 0$  can be transformed by smooth invertible changes of the coordinates and the parameters into the form (4.26) up to and including second order terms. These systems are said to have generic saddle-node bifurcations. We will see that some extra non-degeneracy and transversally conditions must be imposed. These conditions will actually specify which one-parameter system having a saddle-node bifurcation can be considered generic. We show exemplary how the genericity theorem is proven for saddle-node bifurcations.

**THEOREM 4.8.2 (SADDLE-NODE BIFURCATION)** *Suppose  $\dot{U} = F(U, \mu)$ ,  $U, \mu \in \mathbb{R}$ ,  $F$  smooth, has an equilibrium at  $U = 0$  and  $\mu = 0$  and let  $F_U(0, 0) = 0$ . Assume the following conditions are satisfied*

$$F_\mu(0, 0) \neq 0 \quad (4.27)$$

and

$$F_2(0) = \frac{1}{2}F_{UU}(0, 0) \neq 0. \quad (4.28)$$

Then there exist invertible coordinate and parameter changes transforming the system to

$$\dot{\eta} = \beta + s\eta^2 + O(\eta^3).$$

**Proof** We perform a Taylor expansion of  $F$  in Equation (4.25),

$$F(U, \mu) = F_0(\mu) + F_1(\mu)U + F_2(\mu)U^2 + O(U^3). \quad (4.29)$$

We have  $F_0(0) = F(0, 0) = 0$ , due to the equilibrium condition and  $F_1(0) = F_U(0, 0) = 0$ , since we have a saddle-node bifurcation here. Then a new variable  $\xi$  is introduced by the following linear coordinate shift

$$\xi = U + \delta,$$

where  $\delta = \delta(\mu)$  is an a-priori unknown function, which will be defined later. We insert the coordinate transformation in to Equation (4.25) using Equation (4.29) and get

$$\begin{aligned} \dot{\xi} &= \dot{U} = F_0(\mu) + F_1(\mu)(\xi - \delta) + F_2(\mu)(\xi - \delta)^2 + \dots \\ &= (F_0(\mu) - F_1(\mu)\delta + F_2(\mu)\delta^2 + O(\delta^3)) \\ &\quad + (F_1(\mu) - 2F_2(\mu)\delta + O(\delta^2)) \xi \\ &\quad + (F_2(\mu)\delta - O(\delta)) \xi^2 \\ &\quad + O(\xi^3). \end{aligned} \quad (4.30)$$

By using Equation (4.28) there exists a smooth function  $\delta(\mu)$  that annihilates the linear term in Equation (4.30) for all sufficiently small  $|\mu|$ , which follows from the implicit function theorem. The condition for the linear term to vanish can be written as

$$\bar{F}(\mu, \delta) = F_1(\mu) - 2F_2(\mu)\delta + \delta^2\phi_1(\mu, \delta) = 0,$$

with some smooth function  $\phi_1$ . We have

$$\begin{aligned}\bar{F}(0, 0) &= 0, \\ \frac{\partial \bar{F}}{\partial \delta}(0, 0) &= -2F_2(0) \neq 0, \\ \frac{\partial \bar{F}}{\partial \mu}(0, 0) &= -2F_1'(0) \neq 0.\end{aligned}$$

Therefore, it follows the (local) existence and uniqueness of a smooth function  $\delta = \delta(\mu)$  such that  $\delta(0) = 0$  and  $\bar{F}(\mu, \delta(\mu)) = 0$ , with

$$\delta(\mu) = \frac{F_1'(0)}{2F_2(0)}\mu + O(\mu^2).$$

We plug that in into Equation (4.30) and get

$$\dot{\xi} = (F_0'(\mu) + O(\mu^2)) + (F_2(0) + O(\mu)) + O(\xi^3). \quad (4.31)$$

In addition to the coordinate transformation we introduce a new parameter  $\alpha = \alpha(\mu)$ ,

$$\alpha = F_0'(\mu) + \mu^2\phi_2(\mu)$$

with some smooth function  $\phi_2$ . We have

$$\begin{aligned}\alpha(0) &= 0 \\ \alpha'(0) &= F_0'(0) = F_\mu(0, 0).\end{aligned}$$

When Equation (4.27) holds, there exists locally an unique smooth inverse function  $\mu = \mu(\alpha)$  with  $\alpha(0) = 0$ . With this we can rewrite Equation (4.31) as

$$\dot{\xi} = \alpha + b(\alpha)\xi^2 + O(\xi^3),$$

where  $b(\alpha)$  is a smooth function with  $b(0) = f_2(0) \neq 0$ . Finally, a scaling is done with  $\eta = |b(\alpha)|\xi$  and  $\beta = |b(\alpha)|\alpha$  and we get

$$\dot{\eta} = \beta + s\eta^2 + O(\eta^3),$$

where  $s = \text{sign}(b(0)) \in \{-1, 1\}$ . ■

### 4.8.2 HYSTERESIS

The occurrence of two saddle-node bifurcation points connected by an unstable branch leads to hysteresis effects. The term hysteresis is based on the greek word “hysteros” meaning “deficiency” or “lagging behind”. A system with hysteresis exhibits path-dependency in its dynamics. That means, for a certain control parameter more than one stable state of the system is possible and the actual state of the system depends on which path it is following.

Many physical systems naturally exhibit hysteresis. It occurs e.g. in magnetic and ferromagnetic materials. When an external magnetic field is applied to a ferromagnet, the atomic dipoles align themselves with the external field. Even when the external field is removed, part of the alignment will be retained: the material is magnetized. If we look the other way round and reduce the magnetic field linearly from a saturated material, the magnetic flux density will follow a different curve as it has followed for a growing external field. One obtains a S-shaped loop. The width of the middle part of the S describes the amount of hysteresis, related to the coercivity of the material.

Besides the physical applications, hysteresis also occurs in biology. It is found in cell biology [88] as well as in neuroscience [10]. In dynamical system theory hysteresis occurs in a system with the normal form

$$\dot{U} = \mu + U - U^3, \quad U, \mu \in \mathbb{R}$$

with two bifurcation points where no branching but a change of stability takes place. We have a system with two saddle-node bifurcations. A physical system will always presume a stable solution, i.e. for small changes of  $\mu$ , the stable solution jumps from one stable branch to the other (see Figure 4.4). The system will have different states, depending whether  $\mu$  grows or diminishes.

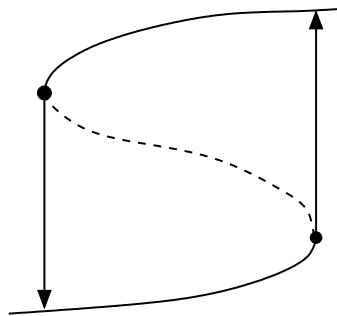


Figure 4.4: A hysteresis formed by two saddle-node bifurcation points (black dots), connected by an unstable branch (dashed line). A physical system with this dynamics will perform jumps between stable branches (solid lines) indicated by the arrows when coming to the bifurcation points.

The presence of hysteresis in the dynamics of Equation (4.25) makes changes in the system states stable for small fluctuations in the bifurcation parameter  $\mu$ . Therefore, the system has two clearly defined stable states (Figure 4.4, upper and lower branches with solid lines). As the system gets near a saddle-node point (black dots), it jumps suddenly to the other stable branch. After the jump it is stable with regard to further fluctuations of the parameter  $\mu$ , i.e. stays on the second branch.

The path-dependency is one effect that may occur in dynamical systems. There is a wide range of other effects described by other standard types of local bifurcations for one-dimensional systems like Hopf bifurcations, which have been mentioned earlier, trans-critical or pitchfork bifurcations. These bifurcations do not occur in the simulations results included in this work. Therefore, we do not go into detail for their description.

### 4.8.3 CUSP BIFURCATION

In the case of dynamical systems depending on two parameters, i.e.

$$\dot{U} = F(U, \mu), \quad U \in \mathbb{R}, \mu \in \mathbb{R}^2$$

other bifurcations may occur. Having an equilibrium at  $\mu = 0$  and  $x = 0$  with

$$F_U(0, 0) = 0 \tag{4.32}$$

$$\frac{1}{2}F_{UU}(0, 0) = 0 \tag{4.33}$$

a so-called cusp bifurcation takes place. Again there is a theorem describing the conditions, when a cusp bifurcation is generic.

**THEOREM 4.8.3 (CUSP BIFURCATION)** *Suppose the dynamical system*

$$\dot{U} = F(U, \mu), \quad U \in \mathbb{R}, \mu \in \mathbb{R}^2$$

*with smooth  $F$ , has at  $\mu = 0$  the equilibrium  $U = 0$ , and let the cusp bifurcation conditions hold:*

$$F_U(0, 0) = 0, \quad \frac{1}{2}F_{UU}(0, 0) = 0.$$

*Assume that the following genericity conditions are satisfied*

$$F_{UUU}(0, 0) \neq 0$$

*and*

$$(F_{\mu_1}F_{U\mu_2} - F_{\mu_2}F_{U\mu_1})(0, 0) \neq 0.$$

*Then there are smooth invertible coordinate and parameter changes transforming the system into*

$$\dot{\eta} = \beta_1 + \beta_2\eta \pm \eta^3 + O(\eta^4).$$

In practical applications it is not only interesting to detect a bifurcation point, but also to follow it for changing parameter values. In the next section we show, how this can be done.

#### 4.8.4 PSEUDO-ARCLENGTH CONTINUATION

Numerical continuation in the case of bifurcation points, means to follow the path  $(U, \mu)$  for which a continuation condition

$$G(U, \mu) = 0, \quad G : \mathbb{R} \times \mathbb{R}^M \rightarrow \mathbb{R}^M \quad (4.34)$$

is fulfilled. In the case of saddle-node bifurcations of  $\dot{U} = F(U, \mu_1, \mu_2)$  we have  $G(X, \mu) = (F(X, \mu), F_X(X, \mu))$ , with  $X = (U, \mu_1)$  and  $\mu = \mu_2$ . Hence, we solve the condition for an equilibrium and a zero eigenvalue of  $F_U$  in tandem. The idea behind numerical continuation lies in the implicit function theorem, which reads as follows.

**THEOREM 4.8.4 (IMPLICIT FUNCTION THEOREM)** *If for some  $\mu = \mu_0$  we can find a solution of (4.34)  $U = U_0$ , then provided  $G_U(U_0, \mu_0)$  is nonsingular, a smooth path of solutions  $U(\mu)$  can be continued locally, with  $U(\mu_0) = U_0$ .*

A numerical strategy for solving (4.34) will be introduced in the following. A very good method for solving systems of nonlinear equations is Newton's method, if a sufficiently good initial guess is available.

Therefore, a predictor-corrector algorithm is applied to follow the solution curve in small steps  $(U_i, \mu_i)$ ,  $i = 1, \dots, N$  which is possible if the implicit function theorem holds. We use the solution at the previous parameter value  $\mu_i$  to make a prediction  $U_{i+1}^{(0)}$  for the solution at the new parameter  $\mu_{i+1}$ . Then Newton's method is used to correct the prediction. Note, that this predictor-corrector method should not be confused with predictor-corrector method for solving initial values problems [111].

There are several possibilities for predictors, trivial ( $U_{i+1}^{(0)} = U_i$ ) or secant predictors to mention two of them. We will use a tangent predictor

$$U_{i+1}^{(0)} = U_i - (\mu_{i+1} - \mu_i) [G_U(U_i, \mu_i)]^{-1} G_\mu(U_i, \mu_i),$$

which is the same as applying Euler's method.

For the corrector step we start from the predicted point  $U_{i+1}^{(0)}$  and compute a sequence of better approximations  $U_{i+1}^{(j)}$ ,  $j = 1, 2, \dots$  for fixed  $\mu = \mu_{i+1}$  by using Newton's method. Hence,

$$U_{i+1}^{(j+1)} = U_{i+1}^{(j)} - [G_U(U_{i+1}^{(j)}, \mu_{i+1})]^{-1} G(U_{i+1}^{(j)}, \mu_{i+1}).$$

Since Newton's method is expensive for high-dimensional problems, Quasi-Newton's methods may be applied if necessary.

The drawback of the current method is that it fails if the implicit function theorem fails, which is the case, for example, at saddle-node points. A solution is to parameterize the solution curve not by  $\mu$  but by an approximation to the arclength  $s$  along the curve. We then seek a solution curve  $(U(s), \mu(s))$  and during the corrector stage we solve

$$G(U_{k+1}, \mu_{k+1}) = 0 \quad (4.35)$$

$$(U_{k+1} - U_k)^2 + (\mu_{k+1} - \mu_k)^2 = \Delta s^2. \quad (4.36)$$

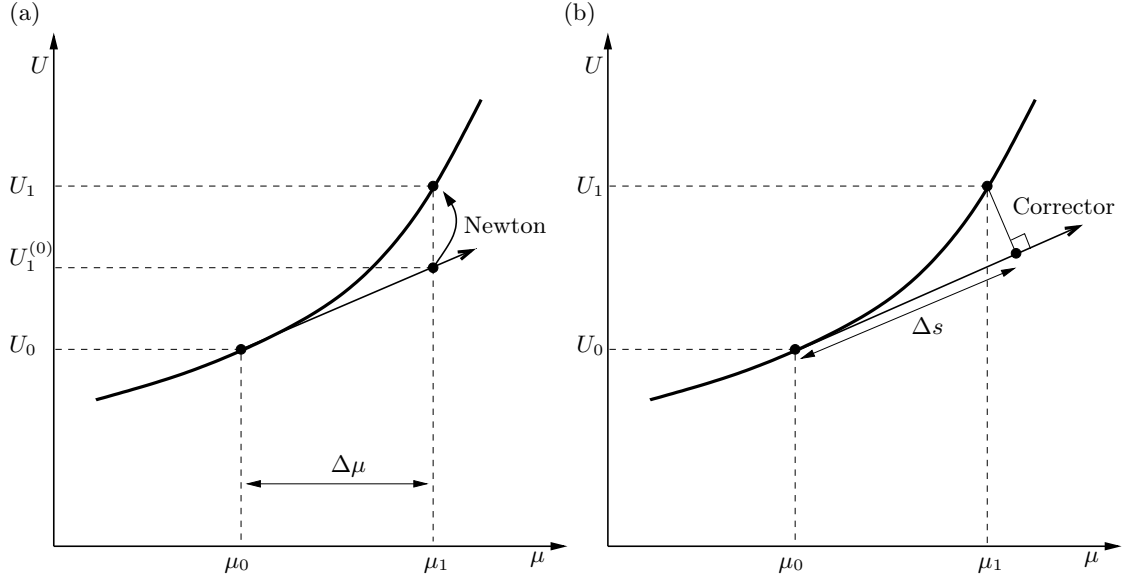


Figure 4.5: *Illustration of continuation approach. (a) Predictor-corrector algorithm using a Newton-step as corrector. Using the initial value  $(U_0, \mu_0)$  a tangent predictor with the step length  $\Delta\mu$  is applied to compute  $(U_1^{(0)}, \mu_1)$ . This point is used as the start value for Newton's method to solve Equation (4.34), i.e. to get  $(U_1, \mu_1)$ . Since this approach does not work as the implicit function theorem fails, pseudo-arclength continuation has to be used as shown in (b). The corrector step is performed by additionally solving Equation (4.37).*

Since linear equations are easier to solve numerically, it makes sense to replace (4.36) with its linearized pseudo-arclength version

$$\langle U'_i, (U_{i+1} - U_i) \rangle + \langle \mu'_i, (\mu_{i+1} - \mu_i) \rangle - \Delta s = 0 \quad (4.37)$$

where  $(U'_i, \mu'_i)$  denotes the tangent vector to the curve  $(U(s), \mu(s))$  at  $(U_i, \mu_i)$ , see Figure 4.5. This allows to follow solution curves of Equation (4.34) even if the implicit function theorem does not hold. Note that a branching point has to be treated in a special way. But we do not see them in our simulations, hence we refer to [23, 65] for more details.

## 4.9 CONCLUSIONS OF CHAPTER 4: EQUATION-FREE SIMULATIONS

In the past chapter we introduced the method of equation-free computations. It turns out that it is a technique suitable for the simulation and analysis of the dynamics of neuron networks as they are present in the OB. This is the case, since macroscopic patterns emerge in the network after odor stimulation as described in Section 2.3.



We showed a convergence theorem for the equation-free method based on classical convergence theory for one-step methods.

To be able to use the equation-free technique, we showed how an equation-free Newton's method can be applied, and how the dependence on independent parameters and traveling waves can be investigated. Finally, we presented how equation-free computations and numerical bifurcation analysis can be combined.

With this considerations we complete the theoretical part of this thesis. In the following we turn our focus to simulations and numerical analysis of the olfactory bulb network dynamics. We apply the equation-free techniques developed in this chapter to simulate and analyze the olfactory network model with point neurons described in Section 2.3 in Chapter 6 to 8. Before doing that we simulate single cells with taking their spatial expansion into account in the next chapter. Here, we will see how the error estimates developed in Chapter 3 can be used to speed up simulations.



## Chapter 5

# ADAPTIVE COMPUTATIONS FOR MITRAL CELLS

*To make no mistakes is not in the power of man;  
but from their errors and mistakes the wise  
and good learn wisdom for the future.*

PLUTARCH

This chapter is devoted to the simulation of a single mitral cell taking its spatial expansion into account by using adaptive computations. First, we investigate the performance properties of the adaptive computations. Second, we look how synapses on the secondary dendrites influence the signal processing in the mitral cell.

---

In this section we simulate the behavior of a model of a mitral cell as they are present in the mammalian olfactory bulb. Our test case is based on the description of the mitral cell geometry found in the literature, see also Section 2.2.2. A mitral cell consists of a tuft, receiving input from the glomeruli, and a primary dendrite, connecting the tuft to the cell body. From the cell body several secondary or basal dendrites spread perpendicular to the primary dendrite. These dendrites receive and give input from and to the granule cells. In our example we have seven secondary dendrites with a diameter between  $1\mu m$  and  $6\mu m$  and a length between  $500\mu m$  and  $600\mu m$ . On each secondary dendrite we have one or two synapses. This number is not realistic, but it is enough to show the main properties of our approach.

For the simulation results of the dynamics of synaptic input in the tuft and on the secondary dendrites of a mitral cell see Figure 5.1. We show the development of the grid

size in the adaptive simulation. Finer grids are used in the neighborhood of synapses and near the cell body as the activity takes place here. A coarse grid is used where no activity takes place, and this are the areas where our approach saves time compared to uniform simulations, but does not lose accuracy.

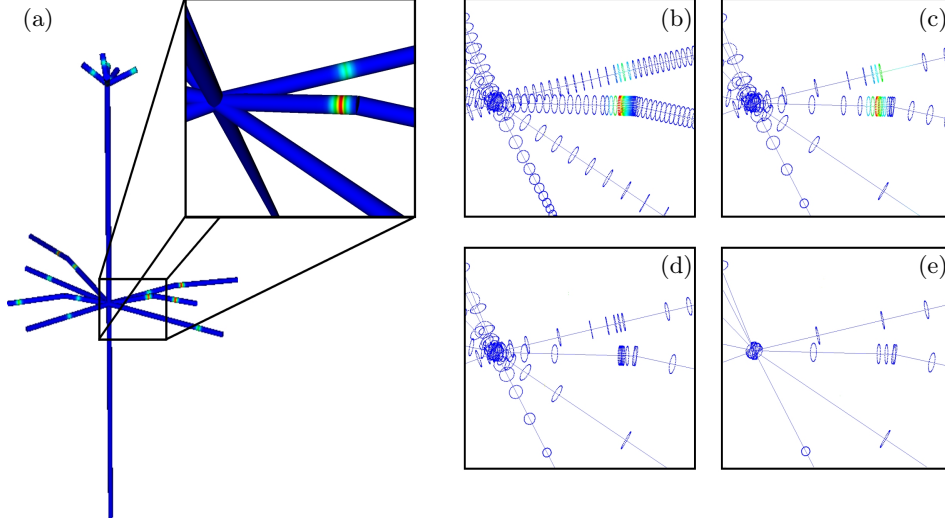


Figure 5.1: *Dynamics of synaptic inputs in the tuft and on secondary dendrites of a mitral cell simulated with error based adaptive grid control. (a) shows the morphology of the considered cell. (b)-(e) depict the development of the spatial grid during the computations. Around the synapses the grid is finer as long as activity takes place there. After that the grid is coarsened until  $\text{min}_{\text{level}}$ . There is one grid point at the beginning and the end of each linear part of the dendrite and at each synapse. Since we have a level 2 refinement, an additional grid point is in between these points.*

If the stepsize control based on the error estimator (3.27) is enabled, we achieve a speed up, since only 71s are then needed for the computations compared to 91.5s without stepsize control. As the synapses are active at the beginning of the simulation, the step sizes are small. When their activity finishes, the steps are increased up to  $dt^{\text{max}}$ . One can profit from the adaptive approach, when one considers a problem where there are areas in space and time where not much activity takes place. We will investigate this behavior in detail in the following.

## 5.1 ADAPTIVE COMPUTATION IN SPACE

To investigate the performance properties of the error estimators, we use a simple test case with a linear piece of a dendrite with one synapse on it. First we test the performance of the spacial error estimator, see Statement (3.4.2). We use uniformly refined grids and

evaluate the error estimator for different levels of refinement. Figure 5.2 shows the result

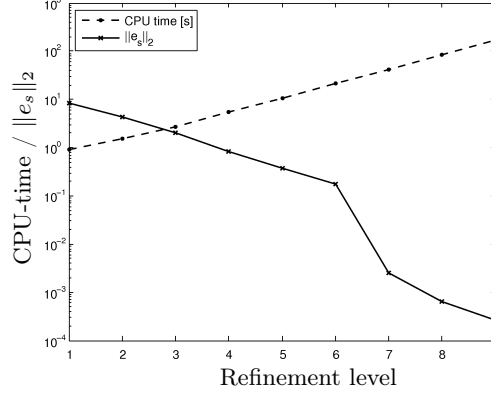


Figure 5.2: *Evaluation of the error estimator (solid line) and computation time (dashed line) for uniformly refined grids from level 1 to level 9 for a linear piece of a dendrite with one synapse. The computation time grows exponentially as the grid is refined more, but the computation error gets smaller.*

of these investigation. As it can be expected, the estimator gets smaller as the grid gets finer, i.e. the error estimator (3.24) is a reasonable measure for the computation error. Between level 6 and level 7 a strong decrease in the size of the error estimator happens. The error estimator depends mainly on the difference in the solution function on different boundary points of the discretization elements, compare Equation (3.26). Due to the simple and small problem, these differences may get smaller between level 6 and 7 as the computational precision for many discretization elements. Hence, these elements do not contribute to the error  $e_s$ . The needed simulation time grows exponentially, which makes sense, since the number of grid points is doubled if the refinement is increased one level.

In a second investigation we look how the adaptive computations perform. Since it can be expected that the adaptive computations show their best performance properties when the simulation area where no activity takes place is large, we increase the length of our test dendrite, still having only one synapse on it. In Figure 5.3 we show, for different error bounds  $TOL$  (see Algorithm 3.1), how the computation time needed for a increasing length of the dendrite develops. In comparison to the uniform case (Figure 5.3 (a)), the adaptive method achieves higher accuracy and is less computationally expensive, see Figure 5.3 (b). In the adaptive case grid points are only added where it is necessary to get better accuracy. This results in smaller grid point numbers as in a uniform grid, where points are added everywhere. Hence, the adaptive strategy allows to save computation time. The amount of saved computation time depends on the refinement level as well as on the considered problem. It is larger when there are larger areas where less activity takes place, i.e. a long dendrite in the model problem. This result can be summarized in Statement 5.1.1.

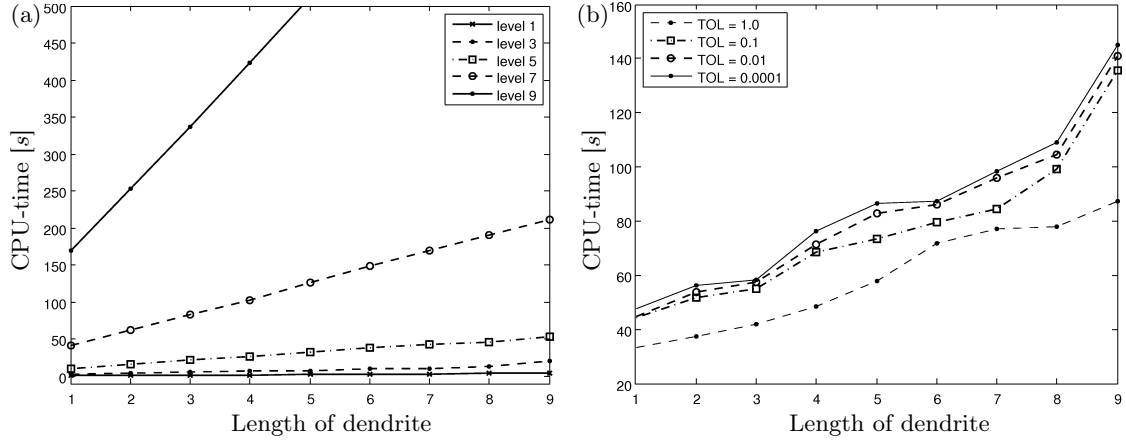


Figure 5.3: *Computation time for uniform (a) and adaptive (b) simulations for an increasing length of the test dendrite. In the uniform case we show the results for different levels of refinement, and in the adaptive case for different values of the error tolerance  $TOL$ . The slope of the curves in the adaptive case shows that better accuracy is here less expensive than in the uniform case.*

**STATEMENT 5.1.1 (PERFORMANCE OF ADAPTIVE GRID CONTROL)** *Compared to uniform refinements, the approach of adaptive grid control allows to perform the computations with the same accuracy faster. The speed up is problem dependent.*

## 5.2 TIME STEP SIZE CONTROL

In a second series of tests we investigate the performance of the error based step size control developed in Section 3.4.2. Again we use a linear piece of a dendrite with one synapse, which is triggered once during the simulation time. Figure 5.4 shows the results of this investigation. We first compare the computation times for equidistant time steps  $dt = \frac{1}{2^l}$ ,  $l$  denoting the grid refinement level and evaluate the error estimator (3.27) for these simulations. It turns out again, that the simulation time grows exponentially and that the error estimator decreases for finer time steps, see Figure 5.4 (a).

Secondly, we directly investigate the performance of the stepsize control, starting with  $dt = \frac{1}{2^l}$ ,  $l$  denoting the grid refinement level with different values of the user tolerance  $TOL$  as defined in Section 3.4.2. It turns out, see Figure 5.4 (b), that the overall computation time grows slower as in the equidistant case with comparable accuracy. It is remarkable that for fine grids the computation time depends less on the tolerance  $TOL$  than for coarse grids. An explanation for this is that the computation error is already very small for fine grids, and therefore the simulations can be always performed with large steps, i.e.  $dt = dt^{\max}$ , with  $dt^{\max} = 1.0ms$  in the simulations. In general this leads to a speed up.

The results of the investigation of the performance of the adaptive stepsize control are

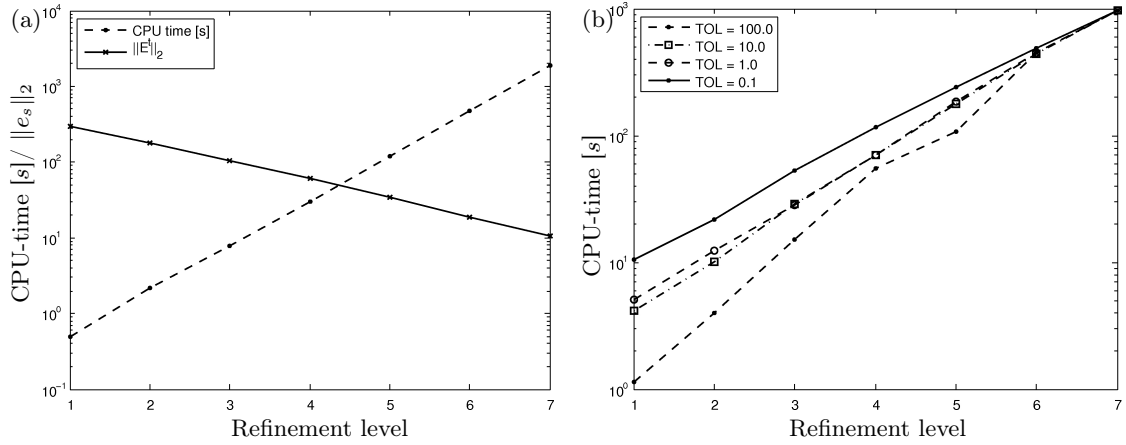


Figure 5.4: *Adaptive stepsize control enables to perform simulations of neuron activity with high accuracy and less computation time as compared to uniform stepsizes, if there are time intervals where no activity takes place.*

summarized in Statement 5.2.1.

**STATEMENT 5.2.1 (PERFORMANCE OF STEPSIZE CONTROL)** *Adaptive stepsize control enables us to perform simulations of neuron activity with high accuracy and less computation time than with uniform stepsizes, if there are time intervals where no activity takes place. As in the adaption of the spatial grid, the improvement depends on the structure of the considered problem.*

### 5.3 INFLUENCE OF INHIBITORY SYNAPSES

To conclude this chapter we apply adaptive computations to investigate the dynamics of a mitral cells with inhibitory synapses. Olfactory bulb mitral cells get inhibitory feedback from granule cells they form synapses with. In the following we investigate how this process may result e.g. in the contrast enhancement properties of the network.

We investigate two aspects of the influence of inhibitory synaptic activity on the dynamics of mitral cells. A model of a mitral cell with seven secondary dendrites is used. We simulate the following situation: the input from the primary dendrite is assumed to trigger an action potential at the cell soma. This results, on one hand, in active transport of the signals along the axon and, on the other hand, in passive signal transport along the secondary dendrites as described in Section 2.3. During this process several interesting situations may occur, as Figures 5.5 and 5.6 indicate. First, we see that active inhibitory synapses repress the signal propagation along the secondary dendrites in Figure 5.5. There are synapses between granule cells and the considered mitral cell all over the MC's dendrites. Hence, granule cells connected further away from the soma as the active inhibitory

synapses will not be activated. This leads to a localization of the activity for the mitral cell dendrites, i.e. the inhibitory synapses may repress the range of signal propagation in the network. It can be understood that this leads to contrast enhancement in the olfactory bulb network.

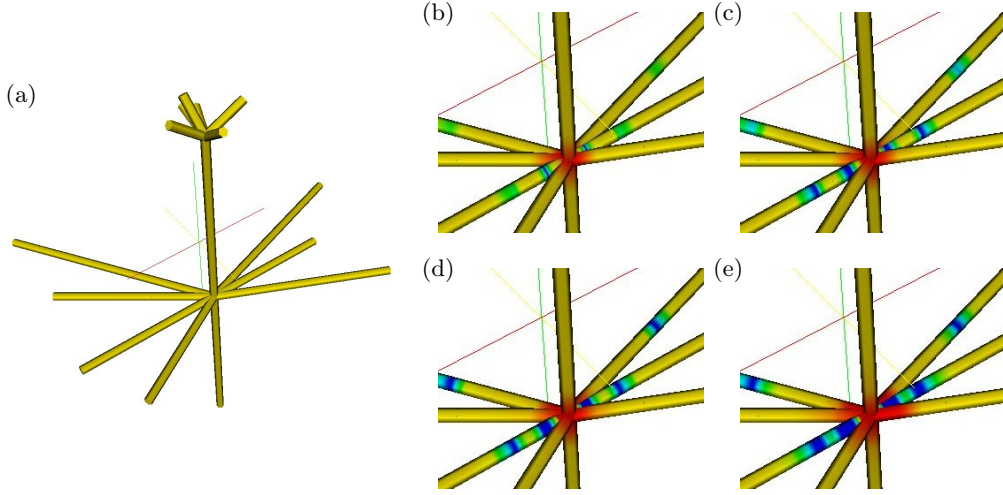


Figure 5.5: *Synapses inhibit the signal processing along the secondary dendrites of a single mitral cell. (a) Morphology of the cell. (b)-(e) Time course of the dynamics. In (d) and (e) the repressing of the signals from the soma due to the activity of inhibitory synapses (blue) is visible.*

It has to be mentioned that this process is very sensitive to the course of the events as Figure 5.6 shows. There the synapses are activated a little bit later as in Figure 5.5. It turns out that the signal along the dendrite is already past the inhibitory synapse when it gets active. That means, the signal is able to activate synapses further of the soma.

Since there are about  $10^4$  synapses per mitral cell in the olfactory bulb of mammals [90], it can be assumed that inhibition is caused by several synapses every time. Therefore, the exact course of time is maybe not that important and the large number of synapses per cell leads to robustness of the system. Nevertheless, our investigations show that inhibitory synaptic activity on the mitral cell secondary dendrites influences the signal processing in the olfactory bulb network.

**STATEMENT 5.3.1 (MITRAL CELL DYNAMICS)** *Inhibitory connections between granule and mitral cells influence the signal processing of mitral cells and can, therefore, mediate contrast enhancement in the olfactory bulb network. The time course of the inhibitory activity compared to the signal processing in the mitral cell is significant for the mitral cell dynamics.*



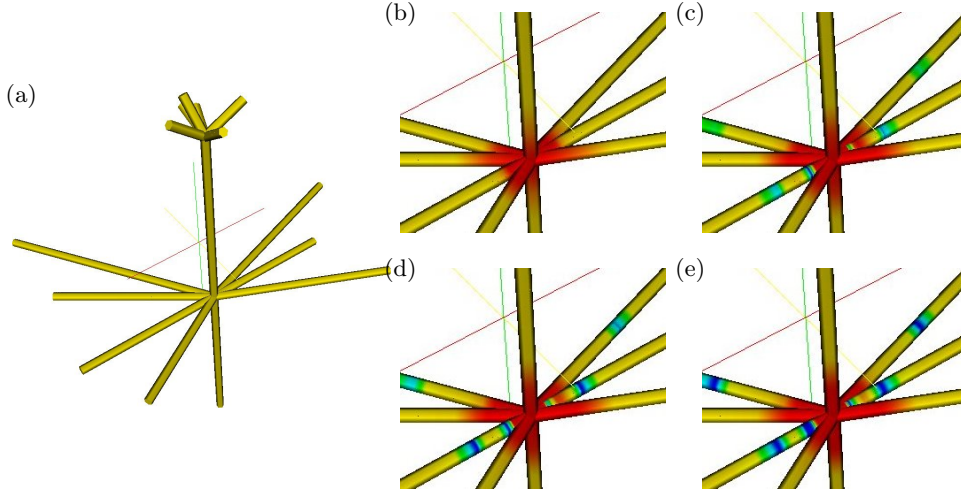


Figure 5.6: *Time course of firing and synaptic activity is important: late activity of a synapse allows the signal to pass. (a) Morphology of the cell. The inhibitory synapses are activated in (c), i.e. later as in Figure 5.5. (d) and (e) show, that the dendritic activation is already past the synapses and is, therefore, able to activate synapses that are further away from the soma.*

## 5.4 CONCLUSIONS OF CHAPTER 5

In this chapter we first showed that adaptive computations in space and time based on the error estimators introduced in Chapter 3 lead to a speed up in computations without loss of accuracy, when there are areas or time intervals where few or no activity takes place.

Secondly, we used the developed simulation tools to investigate the influence of inhibitory synapses to the signal processing in the network of mitral cells and granule cells in the olfactory bulb. Inhibitory synapses can lead to a localization of the activity in the network.

Further simulations of a network formed of mitral and granule cells may underline this statement. At the moment, neuron networks with couplings between the axon of the presynaptic cell and a dendrite of the postsynaptic cell are implemented in NeuroDUNE [67]. But in the olfactory network synapses between dendrites of the pre- and the postsynaptic cell are present. Hence, it is not possible to use this tool for simulating network formed by mitral and granule cells. We solve this problem in the next chapters by investigating a model network of point neurons introduced in Section 2.3.



## Chapter 6

# LATERAL INHIBITION AND CONTRAST ENHANCEMENT

*Sometimes it's good to contrast  
what you like with something else.  
It makes you appreciate it even more.*

DARBY CONLEY

In this chapter we test the equation-free simulation approach with regard to its performance properties for simulating networks of point neurons. We validate the equation-free approach by using results from Principal and Independent Component Analysis of experimental data as simulation setting. Furthermore, we validate our SRM-network of the OB by showing that it reproduces experimental results of lateral inhibition qualitatively. We investigate how these properties are influenced by the connection parameters in the network. Additionally, we investigate contrast enhancement properties of the network with equation-free analysis techniques.

---

### 6.1 EQUATION-FREE SIMULATION OF SPIKING DYNAMICS

In [95] it was shown using Principal and Independent Component Analysis (PCA/ICA), that the time dynamics of the olfactory bulb network can be reproduced by only a few patterns. PCA/ICA uses decomposition of spatiotemporal data sets into simple spatial patterns, so-called modes and the corresponding time course. That means the dynamics of the whole network can be described by few variables. These variables represent in the

considered experiments activity of different neuron groups and blood vessels. The neuron activity is periodic with a period coupled to the breath cycle of the animal. The blood vessel activity is also periodic, but coupled to the heart beat. We will use these insights to develop an equation-free simulation approach to speed up the simulations for the network. In a SRM network with 100 MCs and 400 GCs we defined three “modes”  $M_i$ ,  $i \in \{1, 2, 3\}$  of input from the glomeruli. These are implemented as external input for the SRM neurons during the following time intervals (compare Equation (2.2)).

$M_1: h_{28}^{ext} = 0.3$	$t = 0-10$	30-40	60-70	90-100	120-130
$M_2: h_{52}^{ext} = 0.3$	$t = 10-20$	40-50	70-80	100-110	130-140
$M_3: h_{75}^{ext} = 0.3$	$t = 20-30$	50-60	80-90	110-120	140-150

For all other neurons and during the other time intervals we have  $h_i^{ext} = 0.0$ . This setting models periodic glomerular input to different neuron groups as described above. In equation-free simulations, we apply Algorithm 6.1. Note: in the SRM the dynamics of the network is based on the evaluation of the spiking matrix  $S$  and the external input in each time step. So only  $S$  has to be derived in the lifting routine. We choose  $\delta_C = 0.2$  in the lifting routine of Algorithm 6.1 as threshold for spiking or not spiking, which turned out to be a reasonable value because the coarse variable  $S_C$  is a matrix that represents the average spiking rate and due the refractoriness in the SRM the neurons have times of rest between their spikes.

---

**Algorithm 6.1** Equation-free simulation: Periodic input to the OB network

---

- 1: Start:  $t = 0$
- 2: **while**  $t < t_{end}$  **do**
- 3:   **Fine step:** Simulate the complete network from time  $t$  to  $t + dt$ . Get the spiking matrix  $S(t) \in \mathbb{R}^{(n_m+n_g) \times t}$ .
- 4:   **Restricting:** Compute the mean value  $S_C \in \mathbb{R}^{(n_m+n_g)}$  over the last ten entries in  $S$  for  $t + dt$  and  $t + dt - 1$ , i.e.  $S_{C,i}(t) = \frac{1}{10} \sum_{j=0}^9 S_{i,t-j}$ , for  $i \in \{1, \dots, n_m + n_g\}$ .
- 5:   **Projection:** Derive  $S_C(t + dt + dT)$  using forward Euler scheme

$$S_C(t + dt + dT) = S_C(t + dt) + dT(S_C(t + dt) - S_C(t + dt - 1)).$$

- 6:   **Lifting:** In the SRM we have  $S_i(t) \in \{0, 1\}$  for all  $i$  and  $t$ . We achieve that by setting

$$S_i(\tau) = \begin{cases} 0, & \text{if } S_{C,i} < \delta_C \\ 1, & \text{else.} \end{cases}$$

- 7:    $t = t + dt + dT$ .
  - 8: **end while**
- 

Figure 6.1 shows the time course of the spiking dynamics for a direct (left part) and an equation-free (right part) simulation. In the latter case we have  $dt = 20$  and  $dT = 5$ .

We see that the general dynamics is reflected in the equation-free case. It occurs that sets of spikes in the GCs are not recognized ( $t = 40, 90, 145$ ), or that the spiking takes place to late ( $t \approx 80$ ). But the overall impression is that the equation-free simulation reproduces the rough dynamical properties of the modes and therefore of the network.

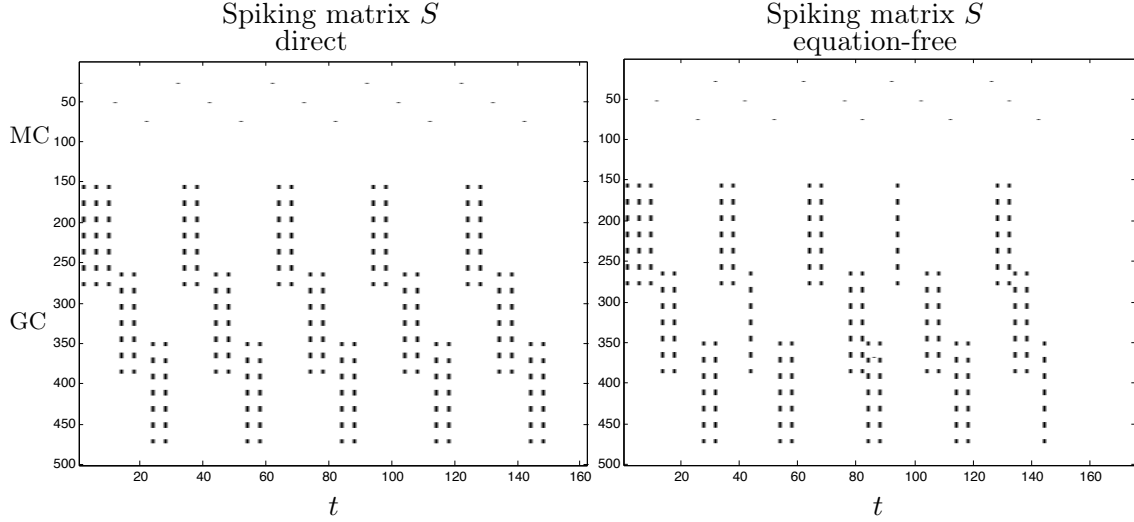


Figure 6.1: *Spiking dynamics of a network with 100 MCs (first hundred lines) and 400 GCs (lower lines). The networks gets input from three modes  $M_i$ ,  $i \in \{1, 2, 3\}$ . Left: direct simulation, right: equation-free simulation. Black entries indicate  $S_i(t) = 1$ , while white ones show  $S_i(t) = 0$ . There is a good agreement, although some spiking activities are not detected by the equation-free simulations due to large coarse steps.*

One of the aims of applying equation-free simulation techniques is to speed up the computations. And, indeed, the equation-free approach in Figure 6.1 is about 25% faster than the direct simulation. Even more speed up can be expected, if one does not evaluate all cells to compute  $S_C$  but one only takes the cells activated by  $M_i$ ,  $i \in \{1, 2, 3\}$  into account. These are the activated MCs and the GCs which are connected to them. The equation-free computations achieve a speed up of about 28% compared to the direct simulations in this case.

We applied the equation-free simulation techniques to speed up the simulations of a SRM network, modeling the neuron network in the olfactory bulb. In Chapter 4 it was pointed out that the microscopic variables are required to converge to a low dimensional inertial manifold quickly, in order to apply equation-free simulations. We want to test this behavior numerically. The test is established in the following way: after several simulation steps, i.e. at  $t = 75$ , we disturb the lifting procedure by replacing  $S_C(t)$  with  $S_C(t) + \bar{\Delta}$ , where we have

$$\bar{\Delta} = \delta \cdot r, \quad r \in [-0.5, 0.5] \text{ a random number.}$$

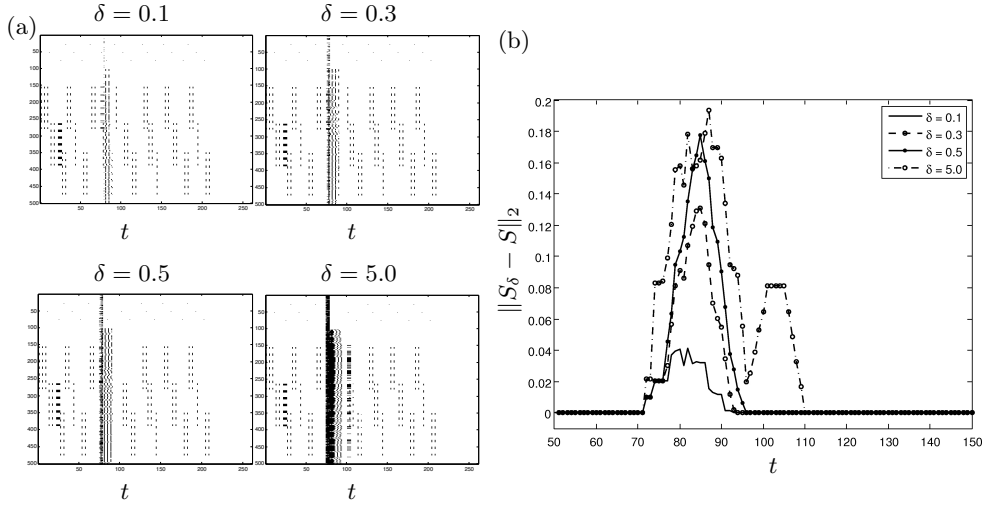


Figure 6.2: *Influence of disturbances in the lifting step: spiking dynamics of a network with 100 MCs (upper part) and 400 GCs. Black entries indicate  $S_i(t) = 1$ . The network gets input from three modes  $M_i$ ,  $i \in \{1, 2, 3\}$ . Disturbed equation-free simulations where a disturbance  $\bar{\Delta} = \delta r$ ,  $r \in [-0.5, 0.5]$  a random number, is added to the spiking matrix  $S(t)$  at  $t = 75$ . (a) Spiking matrices for different disturbances. (b) Error during disturbed simulations. Even for large disturbances the error tends to zero after maximal 40ms, which means two spiking cycles of a MC.*

After this artificial disturbance we investigate how fast the simulations recover to the undisturbed simulation. The main idea of the test is: if the dynamics of the microscopic variables can be described by the macroscopic variables, the system will converge back to the coarse dynamics even if the fine state is disturbed.

Figure 6.2 shows the result of this convergence test. We have the results for  $\delta = 0.1, 0.3, 0.5, 5.0$ . In Figure 6.2 (a) we show the spiking matrices. Figure 6.2 (b) depicts the mean difference in the spiking matrix between the disturbed and the undisturbed simulations. It can be seen that the system recovers quickly for the small disturbances, while it stays disturbed longer for larger  $\delta$ . But even for  $\delta = 5$  the error is zero after 40ms, i.e. maximal two spiking cycles of a MC, the refractory time of which is 20ms, see Appendix A.2. Hence, the equation-free simulation techniques can be applied in the case of simulating the time dynamics of a SRM network here. Later we will show a case where it cannot be applied.

An improvement of the equation-free simulation techniques can be achieved by simulating several fine ensembles in each fine step and averaging their results. The lifting step is not unique, i.e. there exist several fine representations which fit to a given coarse state. Hence, one lifts the system to several consistent fine states by varying  $\delta_C = 0.2 + 0.01 \cdot r$ , with  $r \in [-0.5, 0.5]$  a random number, and simulates all these states in the next fine step.

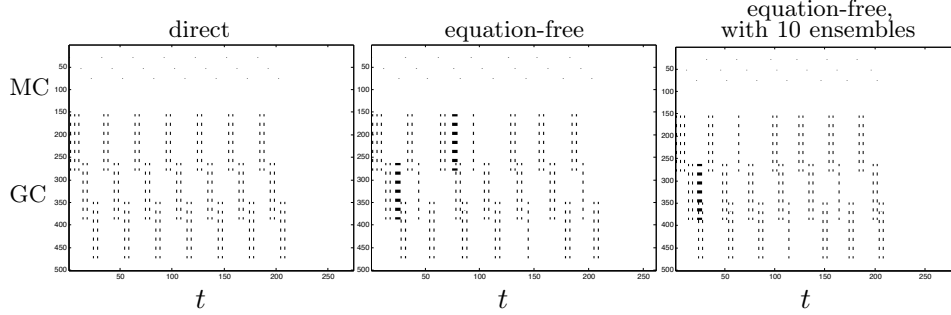


Figure 6.3: *Equation-free simulation with several ensembles: spiking dynamics of a network with 100 MCs (upper part) and 400 GCs. Black entries indicate  $S_i(t) = 1$ , while white ones show  $S_i(t) = 0$ . The network gets input from three modes  $M_i$ ,  $i \in \{1, 2, 3\}$ . Left: direct simulation, middle: simple equation-free simulation, right: equation-free simulation with 10 ensembles.*

The results are restricted and one averages the coarse state afterwards. In Figure 6.3 we depict the results of a simple equation-free computation (middle) and of a simulation with 10 ensembles (right). Compared to the direct simulations (left), we see that the simulation with 10 ensembles gets the better results. The spiking activity for the GCs belonging to the first mode around  $t = 75$  shows extra spikes in the equation-free simulation with one fine state. This activity is not present in the direct simulation and in the equation-free computation with 10 ensembles. So, the result is actually improved. But it is not perfect: at  $t = 75, 125, 175$  some spiking activities are not detected in the equation-free case. And this remains the case even if we increase the number of fine ensembles. What happens here is that the spiking would occur just after the projection step and is, therefore, not detected. But the overall dynamics is reproduced by the equation-free technique.

### 6.1.1 LIMITS OF THE EQUATION-FREE TECHNIQUE

To conclude this section we show the limits of the equation-free approach. We look at a setting that is a little different to the one used above: the network gets continual input from the three modes  $M_i$ ,  $i \in \{1, 2, 3\}$ . The input  $h_{ext}^i = 0.3$  starts at different points in time. I.e. mode  $M_1$  is active for  $t > 10$ ,  $M_2$  is active for  $t > 20$ , and  $M_3$  for  $t > 30$ . The fine steps, lifting, restricting, and the projection step are the same as described in Algorithm 6.1.

In Figure 6.4 we see the direct (left) and the equation-free (right) results for this investigation. We used 50 ensembles in this simulation. We see that as the simulation proceeds, the spiking activity for all three modes synchronize. This situation can not be found in the direct simulations. We can not improve this situation by using more ensembles. This problem shows the limits of the equation-free approach: the reason for

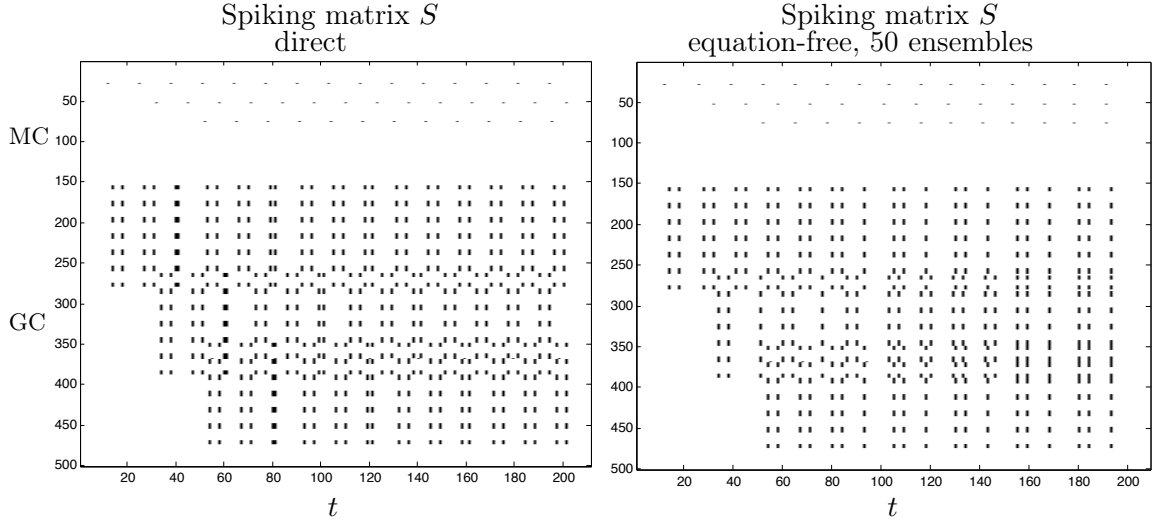


Figure 6.4: *A problem setting, where equation-free simulation does not work. Spiking dynamics of a network with 100 MCs and 400 GCs. The network gets continual input from three modes  $M_i$ ,  $i \in \{1, 2, 3\}$ , starting at different time points. Left: direct simulation, right: equation-free simulation with 50 ensembles. In the equation-free simulation the system “forgets” the different starting points and the activity gets in phase, which will not happen in the direct simulations.*

the phase delay in the spiking activity of the cells belonging to the different modes is that their input starts at different times. These settings are “forgotten” during the equation-free projection. After several time steps the rules governing the dynamics of the network do not include the rules responsible for the phase shift anymore. Since the system is re-initialized during the equation-free computations, only the dynamics belonging to the rule “continual input for all modes” are simulated.

These investigations show the limits of the equation-free simulation techniques. If the rules governing the coarse dynamics are not present any more, the system will converge to the wrong macroscopic state. But the investigation above showed that there are problems where this approach can be used in the case of simulating networks of SRM neurons. We will use this knowledge to investigate the behavior of the network due to changing parameters in the next sections.

This section investigated how equation-free simulation techniques can be used to simulate the spiking dynamics of a model of the olfactory bulb network. It turned out, that the following statement holds.

#### STATEMENT 6.1.1 (EQUATION-FREE COMPUTATIONS OF SPIKING ACTIVITY)

*Equation-free simulation techniques are able to reproduce the results of direct simulations*



*in the case of on going periodic activation of the network. If the dynamics depends on activities back in time, the equation-free method is not able to memorize these effects.*

## 6.2 LATERAL INHIBITION

**L**ike in several neuron networks of the nervous system, lateral inhibition is a main principle according to which signals are processed in the olfactory network [6, 71]. We first define this term [118].

**DEFINITION 6.2.1** *In sensory systems one observes an suppressed activity of weakly stimulated cells if strongly stimulated cells are activated nearby. This process is called **lateral inhibition**.*

In the olfactory bulb, lateral inhibition is mediated amongst others by the MC-GC circuit, which involve inhibitory connections between cells of different types [104, 117]. We follow the ideas developed in [6, 30] to determine whether our model developed in Section 2.5 gives rise to lateral inhibition: we stimulate, i.e.  $h^{ext} = 0.5$ , a single MC in a  $10 \times 10$  array of uniformly weak stimulated cells with  $20 \times 20$  GCs. The background input is set to  $h^{ext} = 0.3$ . Since the spiking activity of MCs getting input from the same glomerulus is correlated [103], this approach can also be interpreted as inhibition among glomeruli, which can be seen experimentally [7].

In Figure 6.5 we plot the number of spikes which occur in the MC-array during a simulation time of 500ms for different values of the connection parameters  $r_{exc}$ ,  $r_{inh}$ ,  $J_{exc}$  and  $J_{inh}$ . In Figure 6.5 (a) we have  $r_{inh} = 7.5$  and  $J_{inh} = 0.5$  and changing values  $r_{exc}$  and  $J_{exc}$  and in Figure 6.5 (b) the role of the excitation and the inhibition parameters are exchanged with  $r_{exc} = 2.0$  and  $J_{exc} = 0.5$ . For all parameter values we see clearly that the spiking activity around the strongly activated MC is diminished. In Figure 6.5 (a) the influence of  $r_{exc}$  and  $J_{exc}$  is shown: as  $r_{exc}$  grows, the radius of the inhibited area grows. Since  $r_{exc}$  describes the radius of interaction where synapses between MCs and GCs are formed, this observation was expected. The activated MC influences GCs which are further away and, therefore, influence also more distant MCs. This leads to a larger radius where lateral inhibition takes place.  $J_{exc}$  is not that much responsible for the size of the simulation area but more for its structure.

The same holds for the influence on the other two connection parameters as it is shown in Figure 6.5 (b). It can be seen that the influence on the size of the inhibited area is not as large as in the case of  $r_{exc}$ . The three parameters  $r_{inh}$ ,  $J_{exc}$  and  $J_{inh}$  influence more the structure of the inhibition, i.e. are all cells diminished homogeneously or is there a structure that can be seen. Since in the case of homogeneous diminution the neighboring MCs are spiking less as in the inhomogeneous case. The latter can be interpreted as less inhibition than in the first case. That means we get an increase of inhibition as  $r_{inh}$ ,  $J_{exc}$

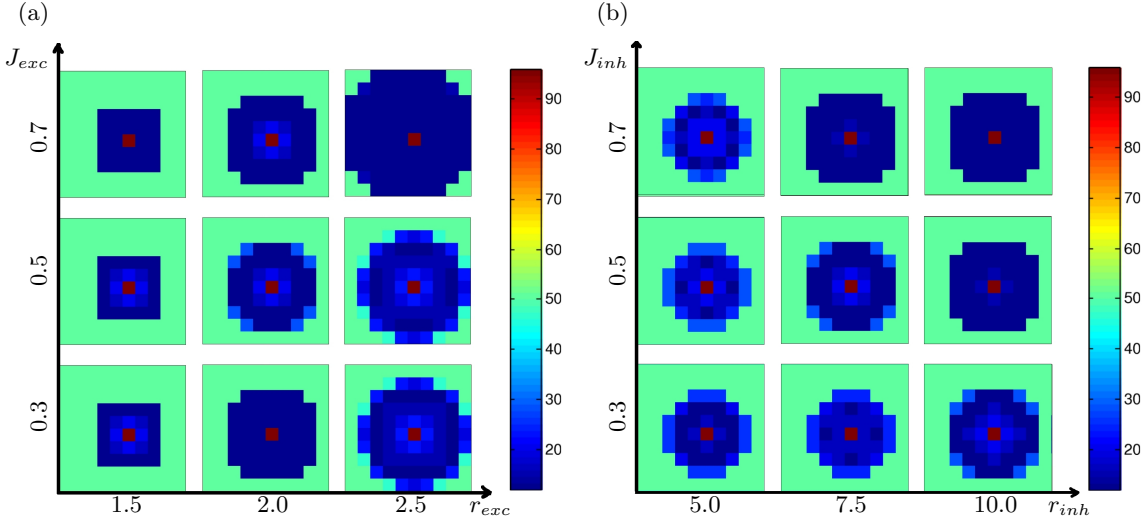


Figure 6.5: *Lateral inhibition is responsible for less spiking activity around an active cell. In (a) we have  $r_{inh} = 7.5$  and  $J_{inh} = 0.5$  and changing values  $r_{exc}$  and  $J_{exc}$  and (b) it is  $r_{exc} = 2.0$  and  $J_{exc} = 0.5$ . The influence of the connection parameters  $r_{exc}$ ,  $r_{inh}$ ,  $J_{exc}$  and  $J_{inh}$  shows that the parameter which influences lateral inhibition most is  $r_{exc}$ , i.e. the length of the secondary dendrites of the MCs. All other parameters do not influence that much the size of the inhibition area but the structure of inhibition.*

or  $J_{inh}$  grow. The results of this section are summarized in Statement 6.2.2.

#### STATEMENT 6.2.2 (LATERAL INHIBITION IN THE OB NETWORK MODEL)

*Lateral inhibition is included in the network model of the olfactory bulb developed in this work. Its range depends mostly on the length of the secondary dendrites of the mitral cells modeled by the radius of excitation  $r_{exc}$ .*

### 6.3 CONTRAST ENHANCEMENT

Contrast enhancement is assumed to be a direct consequence of lateral inhibition [112]. It is defined in the following way [44]:

**DEFINITION 6.3.1 Contrast enhancement** *means, that even if initial firing patterns of MCs evoked by related odors are similar, after a few hundred milliseconds the firing patterns will become distinguishable.*

We introduce a method to investigate the contrast enhancement properties of a MC-GC-network based on the geometric properties of the input and output signals, indicated by the membrane potentials of the MCs.

We look at the geometric properties of the network activity by monitoring two activity centers in the MC layer of the network. As measure for contrast enhancement we choose the distance between the centers  $\Delta_{ce}$  (compare Figure 6.6 (a)). It grows up to a stationary state in the course of time. Figure 6.6 (b)-(d) show different stationary states for different values of  $J_{exc}$ . Note that the network activity takes place in an oscillatory manner. Stationary state is meant here in the sense that the amplitude of the oscillations is constant. The idea behind this setting is the following: The easiest way to achieve that the initial firing patterns of MCs become more distinguishable during signal processing is to sharpen the boundaries of nearby activity centers. This is seen in imaging experiments [45]. We map this observation to our model by investigating how much the distance between two activity centers grows in the course of time. It turns out that the distance reaches a stationary state as discussed above.

Therefore, we compute the stationary state of the distance  $\Delta_{ce}$  between the activity centers for different values of  $J_{exc}$  and  $r_{exc}$  in a network with 100 MCs and 400 GCs. The activity centers are implemented as external input  $h_i^{ext} = 5$  for the SRM neurons in the centers. The other MC have again a weak input  $h_i^{ext} = 0.3$ .

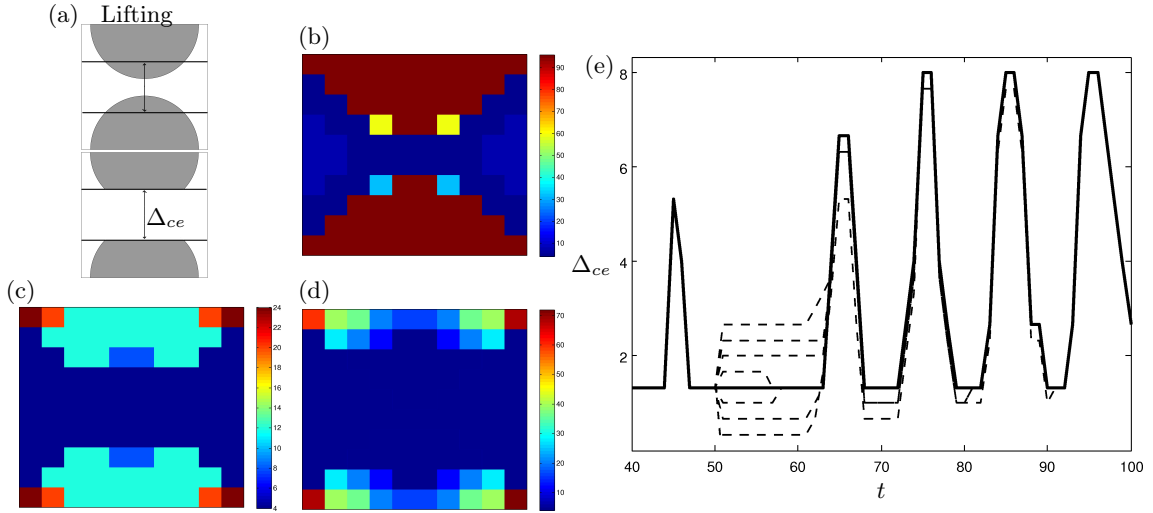


Figure 6.6: *Equation-free investigations of contrast enhancement in the OB network model. (a) Schematic illustration of lifting procedure. (b)-(d) Spiking activity showing differences in contrast enhancement, (b)  $\Delta_{ce} = 2$ , (c)  $\Delta_{ce} = 4$  and (d)  $\Delta_{ce} = 8$ . (e) Convergence of disturbed simulation (dashed lines) to undisturbed simulation (solid line).*

### 6.3.1 EQUATION-FREE INVESTIGATIONS OF CONTRAST ENHANCEMENT

In the following, we use an equation-free approach, where we investigate the behavior of

$\Delta_{ce}$  by treating it as a coarse variable. This approach speeds up the simulations compared to direct parameter studies. It is assumed to be described by a dynamical system

$$\dot{\Delta}_{ce}(t) = F_{ce}(\Delta_{ce}, r_{exc}, J_{exc}) \quad (6.1)$$

the explicit form of which is unknown. Equation (6.1) is not derived in a closed form analytically but evaluated by simulating the whole system and then deriving  $\Delta_{ce}$  numerically. The restricting routine  $r$ , i.e. deriving  $\Delta_{ce}$  from a given state of the complete system, means here measuring the distance between the activity centers. For example in Figure 6.6 (b) we have  $r(S) = \Delta_{ce} = 2$ , in Figure 6.6 (c)  $\Delta_{ce} = 4$  and in Figure 6.6 (d)  $\Delta_{ce} = 8$ .

When we are in a stationary state, i.e.  $F_{ce} = 0$ , we predict a new  $\Delta_{ce}$  for changing parameter values  $J_{exc}$  or  $r_{exc}$  as described in Algorithm 4.3. As introduced in Section 2.4.1 the state of a SRM neuron network is described by the spiking matrix  $S$ . For a changing macroscopic state, we adjust this state by a lifting procedure  $l$ . Here we set the spiking history of the neurons in the gap between the two activity regions to zero, see Figure 6.6 (a). Then the simulation is started for a new parameter value.

The benefit of this approach is that the system will reach its stationary state faster than after starting the system anew for each parameter. We get a total speed up of about 40% without loss of accuracy, since we are still computing directly until we reach the stationary state. The lifted system reaches the same stationary value of  $\Delta_{ce}$  as the direct simulations for all values of  $r_{exc}$  and  $J_{exc}$ . This statement is underlined by Figure 6.6 (e). Here, we disturb the macroscopic state, i.e.

$$\Delta_{ce} = \Delta_{ce} + \delta, \quad \delta \in [-1, 2]$$

at  $t = 50$  after a lifting step (dashed lines). It can be seen, that after 40ms all curves have converged to the undisturbed state (solid line).

In Figure 6.7 we show how changing network parameters influence the contrast enhancement properties of the network. For small values of  $J_{exc}$ , i.e.  $J_{exc} \in [0.15, 0.3]$  the contrast enhancement properties grow for changing  $r_{exc}$  until they reach a maximum at  $r_{exc} = 40\%$  of the simulation area. After that  $\Delta_{ce}$  gets smaller again. This behavior can be explained in the following way: as the radius of excitation grows more granule cells are activated from the mitral cell activity. Hence, there is also more inhibition in the network. Since the excitation is not strong, i.e. we have small values of  $J_{exc}$  in that regime, this leads finally to a damping of the complete activity in the network. Hence, less contrast enhancement can take place.

For large  $J_{exc}$ , i.e.  $J_{exc} > 0.3$  the situation changes. Now the excitation is strong enough to compete against the stronger inhibition as  $r_{exc}$  grows and, therefore, the contrast enhancement properties grow for growing  $r_{exc}$ . This observations lead to the following statement:

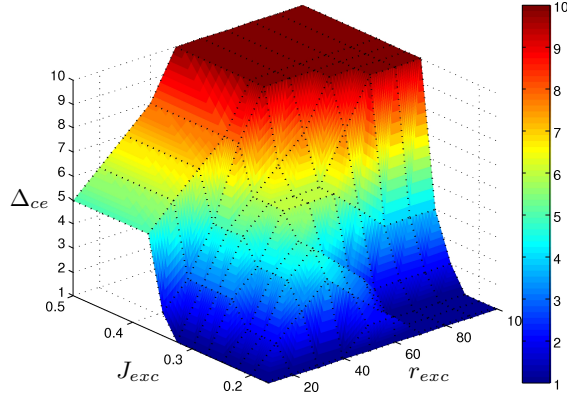


Figure 6.7: Equation-free parameter studies to investigate the dependence of  $\Delta_{ce}$ , the measure of contrast enhancement, on the connection parameters  $r_{exc}$  and  $J_{exc}$ .

#### STATEMENT 6.3.2 (CONTRAST ENHANCEMENT IN THE OB NETWORK MODEL)

The contrast enhancement ability of the olfactory network model is influenced by its connection parameters. For small values of  $J_{exc}$  there is an optimal length of the radius of excitation where the network has its best contrast enhancement properties. Above and below the contrast enhancement ability vanishes. For large  $J_{exc}$  the contrast enhancement ability of the network grows as  $r_{exc}$  grows.

## 6.4 CONCLUSIONS OF CHAPTER 6: LATERAL INHIBITION AND CONTRAST ENHANCEMENT

This chapter consists of three parts. First, we investigated the performance properties of equation-free simulations in the context of spiking neuron networks. We showed where the limits of the approach are, but were also able to show that several cases exist where it performs well.

Secondly, we tested whether our network model is able to reproduce lateral inhibition properties. This was possible. For changing the connection parameters it turns out that  $r_{exc}$  describes how long the range of the lateral inhibition is. The other parameters, namely  $r_{inh}$ ,  $J_{exc}$  and  $J_{inh}$ , are responsible for the structure of the decreased network activity.

In the third part of this chapter, we investigated how  $r_{exc}$  influences the contrast enhancement properties of the network. It turns out that for small values of  $J_{exc}$  not only very small radii of interactions but also large ones do not allow contrast enhancement.

Hence, it can be concluded, that the length of the MC dendrites, which are here modeled by the radius of excitation  $r_{exc}$ , has a major impact on the network dynamics. We will follow this consideration in the next two chapters.  $r_{exc}$  is in mammals about one third of

the size of the OB. For large values of  $J_{exc}$  we get good contrast enhancement properties in that parameter region. For larger values much of the network activity is damped. For smaller values of  $J_{exc}$  the contrast enhancement properties have their optimum for  $r_{exc}$  in the range of one 30% to 40% of the of the simulation area. Hence, our results are comparable to the experimental findings.

## Chapter 7

# ODOR DISCRIMINATION

*If you believe that discrimination exists, it will.*

ANTHONY J. D'ANGELO

In this chapter we investigate the ability of the olfactory bulb network model with point neurons to distinguish binary mixtures of odors, depending on the ratio of the mixtures. It turns out that experimental results can be reproduced qualitatively. Furthermore, we can predict different discrimination abilities depending on the connection parameters of the network. We see that hysteresis effects occur in the network dynamics in the case of systems where long-term dynamics with changing input is investigated.

---

In Chapter 6 we investigated the contrast enhancement behavior of a Spike Response network model of the OB with regard to the distance of geometric activity centers. In this section we look at another biological question where contrast enhancement comes into play: odor discrimination. In [1] behavior experiments with rats were used to investigate the ability to discriminate binary odor mixtures. It turned out that animals need longer to discriminate more similar mixtures than mixtures where one odor is more dominant. This knowledge of the experimental results allows us to define the ability to discriminate odors in the following way.

**DEFINITION 7.0.1** *The ability to discriminate which odor is more present in a mixture of two odors is called **odor discrimination ability**.*

Nearly similar binary odor mixtures evoke almost identical odor maps in the olfactory bulb, which become more distinguishable in the course of time. This is believed to mirror

the results of the behavioral test [1]. In these tests it is measured how fast a mouse is able to detect the dominant odor in a binary mixture of two odors. It turns out, that the animal needs longer to fulfill this task as the odor mixtures become more similar. The mouse needs about  $200ms$  for discriminating simple odors and it requires  $70 - 100ms$  more time to discriminate highly similar binary mixtures. It is generally hypothesized that differences in activity maps reflect the animals ability to discriminate between different odors in behavioral tests [79, 119]. Therefore, we want to explore the time-dependent activity distribution in the network using inputs representing binary odor mixtures. We define external input areas to the MCs in a network with 900 MCs and 8100 GCs. This represents the input from the glomeruli to the network model. The different ratios of odor mixtures are implemented in the SRM by setting  $h_i^{ext} = 0.5c_1$ , if MC  $i$  belongs to the activity area of the first odor and  $h_i^{ext} = 0.5c_2$ , if it belongs to the second activity center, with  $c_1 + c_2 = 1$ . First, we investigate the network model behavior with two very simple inputs – two squares, see Figure 7.1.

By looking at the spiking activities of the mitral cells, depicted in Figure 7.1, it can be seen that differences in the two activity areas occur faster as the ration of two inputs is more different compared to more similar odor mixtures. Hence, it can be assumed that the animal would be able to discriminate the more different setting faster.

In the experiments in [1] the odors amyl acetate and ethyl butyrate were used. Projections of imaging results of the odor maps of odors are shown in Figure 7.2, first and last line. These inputs are projections to the 900 MCs in the considered network model.

In Figure 7.2 the simulation results for the inputs modeling the two odors amyl acetate and ethyl butyrate are shown. The sum of the spikes generated by the MCs up to a certain point in time is again depicted in this figure. One again recognizes that the network needs longer to discriminate more similar mixtures. We want to investigate this behavior in a more formal way and define therefore a quantity that measures the time the system needs to discriminate two odors in the next section.

## 7.1 DISCRIMINATION TIME

In order to investigate the odor discrimination ability of the network model, we define the discrimination time, i.e. the time when the network is able to discriminate which odor is more present in the following way.

**DEFINITION 7.1.1** *The time  $t_d$  needed until a significant difference between the number of spikes in the first activity area and the second area is defined as*

$$t_d = \min t' \quad (7.1)$$

$$s.t. \quad \left\| \frac{1}{o_1} \sum_{i=1}^{o_1} S_i(t < t') - \frac{1}{o_2} \sum_{i=1}^{o_2} S_i(t < t') \right\| > \delta_d.$$



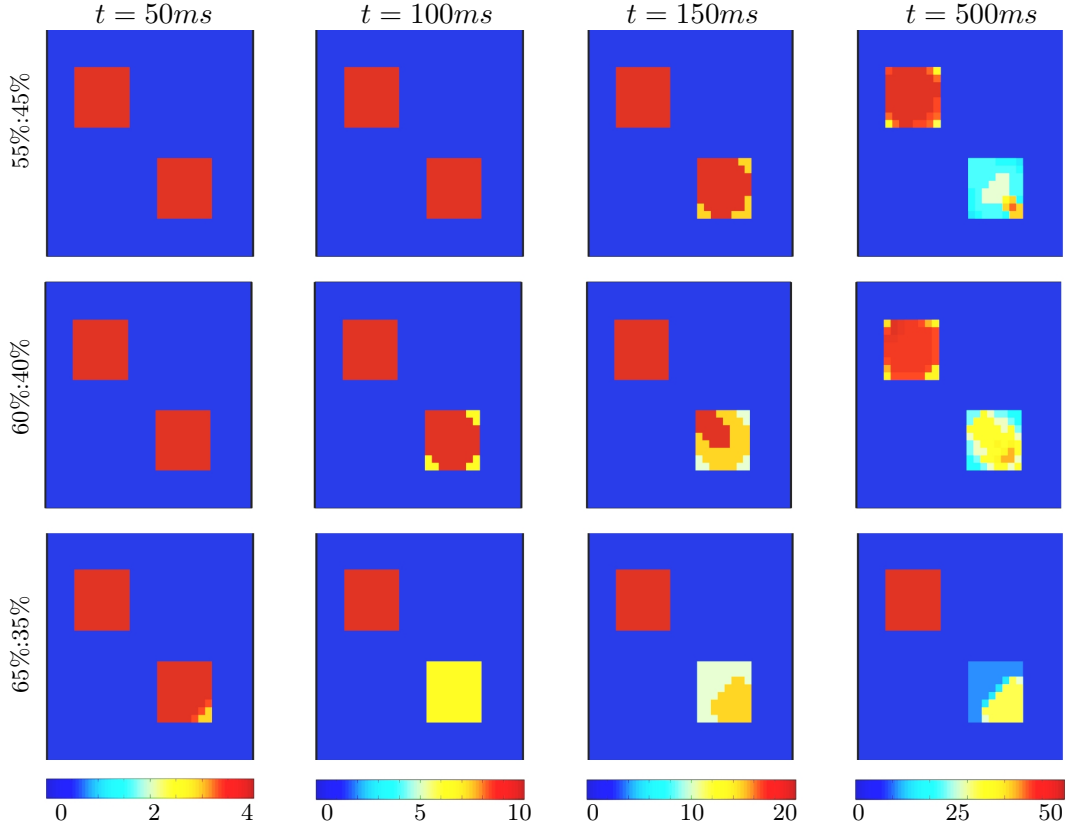


Figure 7.1: Odor discrimination for two square inputs and different ratios of the binary mixtures (55%:45%, 60%:40%, 65%:35%). The sum of the spikes generated by the MCs up to a certain point in time are depicted. It turns out, that the network needs more time to discriminate the odors if the mixtures are highly similar.

We call  $t_d$  **discrimination time**,  $o_i$  denotes the number of cells in the activity area  $i$ ,  $i \in \{1, 2\}$ .

In the following we examine for square inputs and a network of 100 MCs and 400 GCs how the discrimination time  $t_d$  depends on the discrimination threshold  $\delta_d$  and on the connection parameters of the network  $r_{exc}$ ,  $r_{inh}$ ,  $J_{exc}$  and  $J_{inh}$ , see Figure 7.3. One can observe several points in this figure:

- For growing values of  $\delta_d$  the overall discrimination time grows simultaneously, see Figure 7.3 (a). We choose  $\delta_d = 5$ , which equals a spiking rate difference of about 20Hz, for the following simulations.
- $r_{exc}$  has the largest influence on the discrimination time. If the connection in the network are too short or too long, the network is not able to discriminate the odors

as fast as in an optimal area of connectivity length between 30% and 40% of the network size.

- $r_{inh}$  has not much influence on the dynamics compared with the influence of  $r_{exc}$ : it only shifts the  $t_d$  curves in a small range, compare Figure 7.3 (b).
- Strong excitation of the granule cells damps the overall network activity and this leads to an increase of  $t_d$  for large values of  $r_{exc}$  and  $J_{exc}$ , as can be seen in Figure 7.3 (c).
- The effects of less inhibition can be seen in Figure 7.3 (d). As  $J_{inh}$  is small  $t_d$  only gets smaller for relatively large values of  $r_{exc}$ .

One open question is whether the different discrimination times are due to the fact that the odor ratio is different or due to the fact that the odor concentration of the odor with the smaller ratio is not that large. If we change the total input weight  $h_{ext} = \frac{\delta_c}{2} \cdot c_{1,2}$ . It turns out that  $t_d$  keeps nearly the same ( $t_d \in [132ms, 137ms]$ ) for  $\delta_c \in [0.8, 1.4]$ ,  $c_1 = 0.6$ ,  $r_{exc} = 35\%$ ,  $r_{inh} = 30\%$  of the network size, and  $J_{exc}, J_{inh} = 0.5$ . Hence, the difference of the odor discrimination times results indeed from the different odor ratios not from the concentrations. This was also described experimentally [1]. We can conclude this investigations of the odor discrimination ability of the OB network model with the following statement:

**STATEMENT 7.1.2 (ODOR DISCRIMINATION ABILITY)** *The simulation results in this section show, that the odor discrimination ability of the OB network depends on its connection properties. The most influence has the radius of excitation  $r_{exc}$ . There is an optimal interval of its scope where the network is able to discriminate binary odor mixtures fastest. Below and above this area it needs longer to do so.*

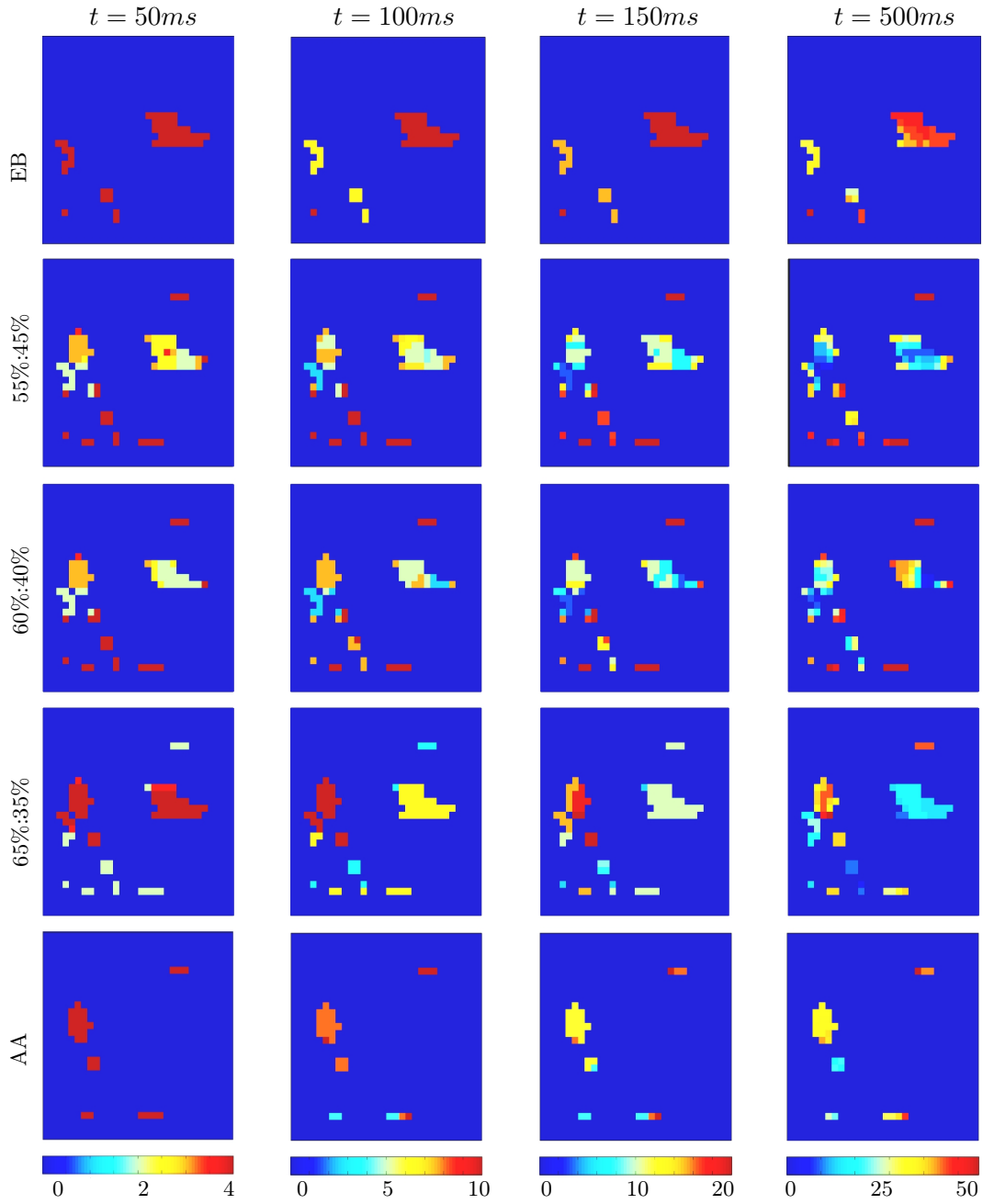


Figure 7.2: Odor discrimination for two inputs, defined based on the activity measured by imaging experiments of ethyl butyrate (EB) and amyl acetate (AA) (top and bottom line). Different ratios of binary mixtures of these two odors (55%:45%, 60%:40%, 65%:35%) show, that similar mixtures need longer to be discriminated than more different mixtures.

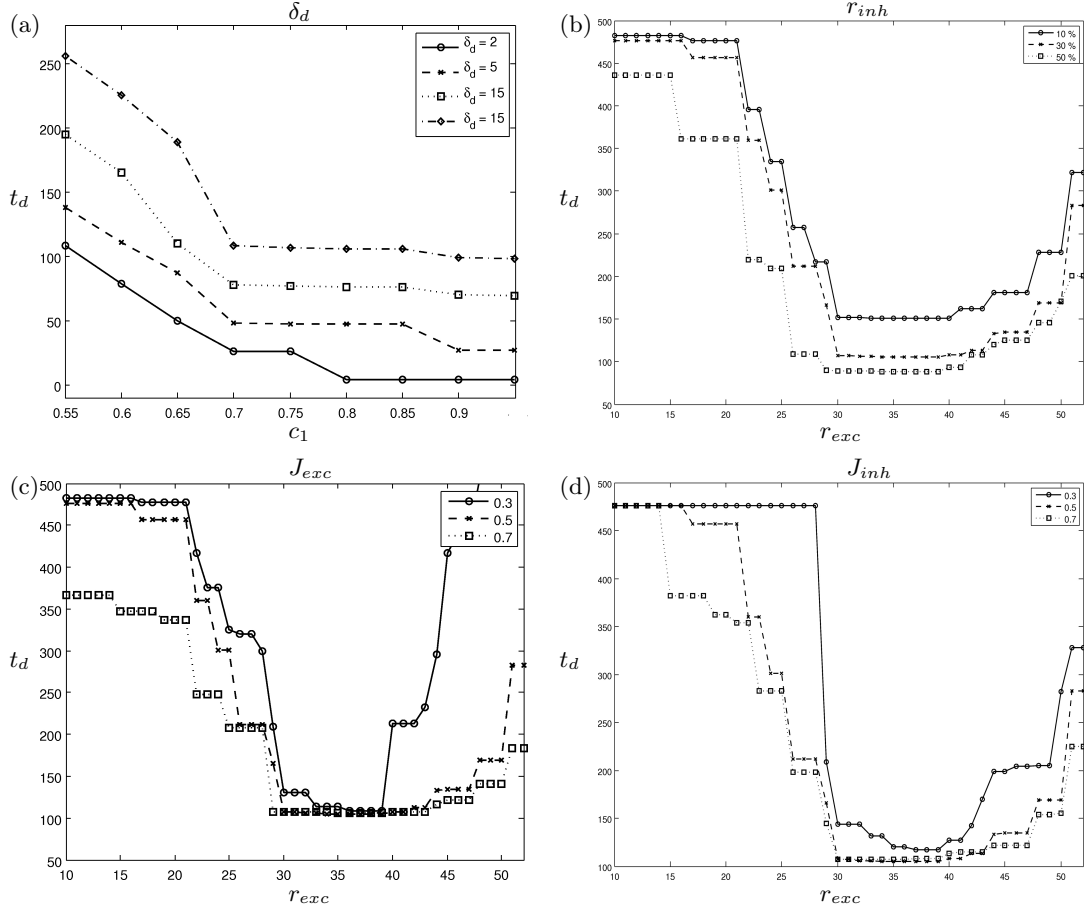


Figure 7.3: Behavior of  $t_d$  depending on the discrimination threshold  $\delta_d$  and on the connection parameters of the network  $r_{exc}$ ,  $r_{inh}$ ,  $J_{exc}$  and  $J_{inh}$ . In (a) the chosen parameter values were  $r_{exc} = 35\%$ ,  $r_{inh} = 30\%$  of the network size and  $J_{exc}, J_{inh} = 0.5$ . For (b)-(d) we have  $c_1 = 0.6$  and  $c_2 = 0.4$ .

## 7.2 EQUATION-FREE CONTINUATION OF SPIKING RATE DIFFERENCES

Mathematically it is interesting to investigate dynamical systems in terms of stationary states and the behavior of the stationary states for changing parameters. Experimental results also show that long term dynamics, i.e. 0.5s to a few seconds, can give rise to other effects as those of the fast dynamics after about 100 to 200ms [45]. Therefore, we look not only at the discrimination time  $t_d$  but also at the spiking rate difference  $\Delta_s$  in the activity centers of the different odors. It turns out that the system reaches the stationary states of  $\Delta_s$  for long simulation times, see Figure 7.4 (a). In many biological systems prehistory of the system is important, i.e. the new state of the system depends on the old state when a system parameter is changed. Learning and hysteresis effects are examples for that. Hysteresis is a phenomenon where a jump from one stable branch of equilibrium points to another branch occurs for a small change of a parameter as described in Section 4.8.2. We use equation-free pseudo-arclength continuation to follow a curve of equilibria points for changing the mixture ration  $c_1$ . The corrector step is performed by an equation-free Newton's method evaluating the unknown equation

$$\dot{\Delta}_s = F(\Delta_s, r_{exc}, c_1) \quad (7.2)$$

numerically using a finite-difference approximation for  $\dot{\Delta}_s$  as it was introduced in Section 4.8.4. The restricting procedure  $r$  is defined here by evaluating the mean spiking rate of the MCs in the two activity centers during the last 50ms, and computing the difference between the rates in the two activity areas. After performing a Newton-step  $\tilde{\Delta}_s = \Delta_s - (\partial F(\Delta_s, r_{exc}, c_1)/\partial \Delta_s)^{-1} F(\Delta_s, r_{exc}, c_1)$ , one has to adjust  $S$ , i.e. the system has to be lifted to a consistent microscopic state. This is done by, on one hand, keeping the spiking activity in the first activity area and, on the other hand, by adjusting the spiking frequency in the second activity area to get the spiking rate difference  $\tilde{\Delta}_s$ . Note that not only  $F(\Delta_s, r_{exc}, c_1)$  is evaluated numerically but also  $\partial F(\Delta_s, r_{exc}, c_1)/\partial \Delta_s$  by computing  $F(\Delta_s + d\Delta_s, r_{exc}, c_1)$  and approximating the derivative by finite differences.

Before we perform the continuation process of the stationary states, we investigate whether  $\Delta_s$  is actually a variable that describes the macroscopic dynamics of the underlying system. In Figure 7.4 (a) we depict the time course of  $\Delta_s$  for  $c_1 = 0.7$  derived by equation-free time-stepping for a small network as used in Figure 7.3. It can be seen that the system needs long, i.e. about 2.5s, until it reaches its stationary state. To test the equation-free approach we disturb  $\Delta_s$  arbitrarily after a lifting step by

$$\Delta_s = \Delta_s + \delta, \quad \delta \in [0.05, 0.4].$$

In Figure 7.4 (b) it can be seen that the disturbed states (dashed lines) converge to the undisturbed state (solid line) in less than 120ms. Hence the equation-free approach can be

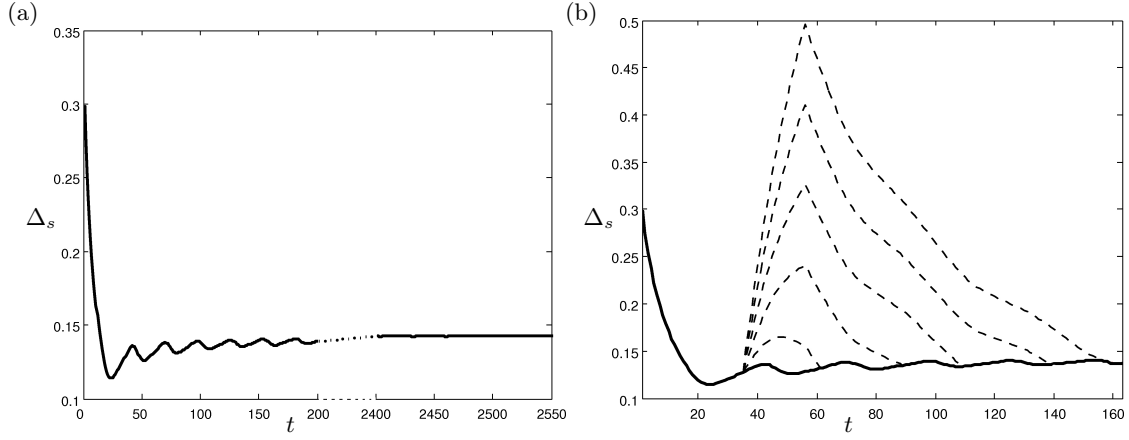


Figure 7.4: *Equation-free time-stepping for the spiking rate difference  $\Delta_s$ . (a) Time-course of  $\Delta_s$ . (b) Convergence of disturbed states (dashed lines) to undisturbed simulation (solid line).*

applied here and we use the continuation approach combined with equation-free Newton's method as described above.

In Figure 7.5 (a) and (b) we show the result of continuation of equilibria of Equation (7.2) for two parameter values of  $r_{exc}$ . In Figure 7.5 (c) a continuation of the bifurcation points detected in Figure 7.5 (a) for changing  $r_{exc}$  is depicted. In Subfigure 7.5 (a) a hysteresis effect for  $r_{exc} = 30\%$  of the simulation area, which is  $90\mu m$  here, formed by two saddle-node bifurcation points  $\alpha_1$  and  $\alpha_2$  is shown. The equilibrium condition  $F(\Delta_s, r_{exc}, c_1) = 0$  and the saddle-node bifurcation condition  $\frac{\partial F}{\partial \Delta_s}(\Delta_s, r_{exc}, c_1) = 0$  as introduced in Section 4.8.1 hold at these points. At the saddle-node points, changes from stable equilibria curves (solid lines) to unstable equilibria curves (dashed line) take place. Therefore, the physical system performs a jump from one stable branch to the other when coming to the bifurcation point.

In Subfigure 7.5 (b) we have  $r_{exc} = 75\%$  of the simulation area, i.e.  $225\mu m$ , and there are no hysteresis effects present. Adaptation takes place instead. By continuing the bifurcation points of Subfigure 7.5 (a) for changing  $r_{exc}$  we can explain this behavior, see Subfigure 7.5 (c). The two branches of the bifurcation points come closer for growing values of  $r_{exc}$ . During this process, the length of the unstable branch between the bifurcation points comes to zero. At the point  $\beta$  where the two bifurcation points come together a cusp bifurcation takes place. Again the equilibrium condition holds and  $\frac{\partial F}{\partial \Delta_s}(\Delta_s, r_{exc}, c_1) = 0$ , but we have additionally  $\frac{\partial^2 F}{\partial \Delta_s^2}(\Delta_s, r_{exc}, c_1) = \frac{\partial^3 F}{\partial \Delta_s^3}(\Delta_s, r_{exc}, c_1) = 0$  and

$$\frac{\partial F}{\partial c_1}(\Delta_s, r_{exc}, c_1) \frac{\partial^2 F}{\partial \Delta_s \partial r_{exc}}(\Delta_s, r_{exc}, c_1) - \frac{\partial F}{\partial r_{exc}}(\Delta_s, r_{exc}, c_1) \frac{\partial^2 F}{\partial \Delta_s \partial c_1}(\Delta_s, r_{exc}, c_1) \neq 0,$$

which are the condition for a cusp bifurcation as introduced in Section 4.8.3. Hence, the

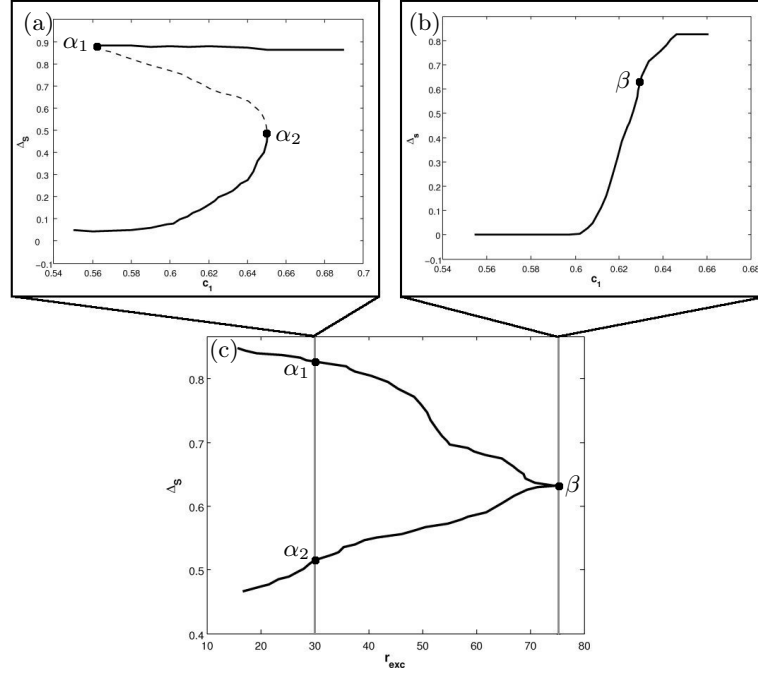


Figure 7.5: *Hysteresis and adaptation effect in a system with prehistory with 900 mitral cells and 8100 granule cells. An equation-free continuation process is applied to follow the equilibria in (a) and (b). For a small excitation radius hysteresis effects are present for changing the mixture ratio of the input. For a large excitation radius the hysteresis effect vanishes and adaptation occurs (b). In (c) the two saddle-node points  $\alpha_1$  and  $\alpha_2$  are continued. They move together forming a cusp-bifurcation at  $\beta$ .*

following statement holds.

**STATEMENT 7.2.1 (HYSTERESIS IN THE OB NETWORK DYNAMICS)** *For systems with prehistory, i.e. changes in the mixture ratio of the input  $c_1, c_2$  take place but the spiking matrix  $S$  is kept, a hysteresis can be detected using equation-free numerical bifurcation analysis and pseudo-arclength continuation. For changes in the radius of excitation of the network  $r_{exc}$  the hysteresis descends to an adaptation effect at a cusp bifurcation point.*

The hysteresis in Figure 7.5 avoids jumping between two states, represented by the lower and the upper stable branch (solid lines). If the system is close to the saddle-node points, some fluctuations in the concentration values make the system jump to the other branch and after the jump it is robust to further fluctuations. In Figure 7.5 (b) fluctuations around the turning point  $c$  lead to jumps between the lower and the upper states.

Hysteresis effects occur in other neuron network models [60]. A model of a network

of pyramidal cells in the prefrontal cortex for example shows a hysteresis effect in the advantage population firing rate for changes in the connection strength of the network [10].

### 7.3 BIOLOGICAL INTERPRETATION

Our investigations showed that the odor discrimination time for a binary mixture depends on the connectivity parameters of the network. But the region where  $t_d$  is at its minimum is, for example, large for  $r_{exc}$  (between 30% and 40% of the network size). For the synaptic strength the minimal  $t_d$  is nearly independent of  $J_{exc}$  and  $J_{inh}$ . This leads to a robustness, i.e. several realizations of the network are feasible. Therefore, nature is able to form a network that is able to perform discrimination tasks fast and can still be optimized for other tasks, too.

The hysteresis as we detected it plays a minor role for simple discrimination tasks, since an animal does not have to wait until the stationary state of the network activity is reached. It is in general able to decide earlier which odor is present. Nevertheless, if similar odorants are present for long times, the animal may reach the stable states. The hysteresis effect described in this chapter will then stabilize the behavior of the animal for small changes in the input.

To conclude this section, we want to have a look at the time scales of the activities related to odor discrimination, on one hand, detected in experiments [16] and, on the other hand, found in our simulations. Note that there are many unknown parameters in the network model, and not much is known about the actual connectivity properties of the network between mitral and granule cells. Hence, all interpretation can be only on the order of magnitude, not on the exact values. As described above, simple odor discrimination tasks are performed fast in experiments, i.e. in about 100ms to 200ms [1]. We saw the same order of magnitude in our simulations shown in Figure 7.1 and 7.2. These results exclude slow mechanisms such as attractor stabilization or slow decorrelation as mechanisms responsible for odor discrimination [1]. Nevertheless, there is experimental evidence, that e.g. winnerless competition models [68] based on slow temporal patterns and specific inhibitory circuits, suggest that a time window of 500ms to several seconds yields enhanced discrimination. In zebrafish a substantial decorrelation of activity patterns was observed only after 0.8s to 1.5s [45]. In this time scale, we reach the stationary states leading to hysteresis effects in the OB network model. Hence, it is supposable that in difficult discrimination tasks hysteresis effects are actually present.

### 7.4 CONCLUSIONS OF CHAPTER 7: ODOR DISCRIMINATION

**A** mathematical investigation of odor discrimination properties of the OB network model was performed in this chapter. We were able to reproduce the results of behavior experi-



ments. There it was shown that animals need longer to discriminate more similar binary odor mixtures.

The odor mixture results in two activity areas in the MCs of the network model. By investigating the stationary states of the spiking difference we were able to apply the techniques of numerical bifurcation analysis. In long-term simulations with changing input ratios we have, depending on the excitation radius  $r_{exc}$  hysteresis or adaptation processes. At the transition between these two situations a cusp bifurcation occurs.

This means we predict measurable path dependencies in the case of relatively short range MCs due to the hysteresis effect found by equation-free computations. For long ranging MC dendrites we saw adaptation processes in our simulations. That means, no path dependency can be expected in that case.



## Chapter 8

# TRAVELING WAVES

*Happiness is not a station you arrive at,  
but a manner of traveling.*

MARGARET LEE RUNBECK

In experiments with zebrafish, traveling waves are detected in the olfactory bulb neuron network. Using a SRM neuron network model, we investigate in this chapter when traveling waves emerge and how their appearance is influenced by the structure and the connectivity of the network. It turns out that, on one hand, the shape of the boundaries of the network has an influence on the shape of the waves. On the other hand, we can show that the radius of interaction is a main parameter which influences the traveling waves. They are faster as the interactions have a wider range. Biological interpretations of the simulation results conclude this chapter.

---

In [44] imaging experiments with zebrafish with voltage-sensitive dyes show traveling-wave-like structures in the dynamics of their olfactory bulb. These experiments measure the activity of the membranes of the cells. Since the GC produce the largest part of cell membranes in the olfactory bulb it is more likely that the images show the GC activity. The experiments show, that traveling waves emerge in an oscillatory manner and that the propagation velocity and direction was nearly odor independent. We will investigate in the following under which conditions we are able to detect traveling waves in the SRM network model established in Section 2.5.

## 8.1 INFLUENCE OF BOUNDARIES

In the case of boundary conditions, where no connections across the boundaries of the simulation area occur, we recognize for a constant external input  $h_{ext}^i = 0.3$  for  $i = 1, \dots, n_m$  traveling waves from the boundary to the center of the simulation area in the MC and the GC layer. As in the experiments the traveling waves emerge in an oscillatory manner. By introducing periodic boundary conditions at the boundary of the MC and GC arrays different wave structures can be produced, see Figure 8.1.

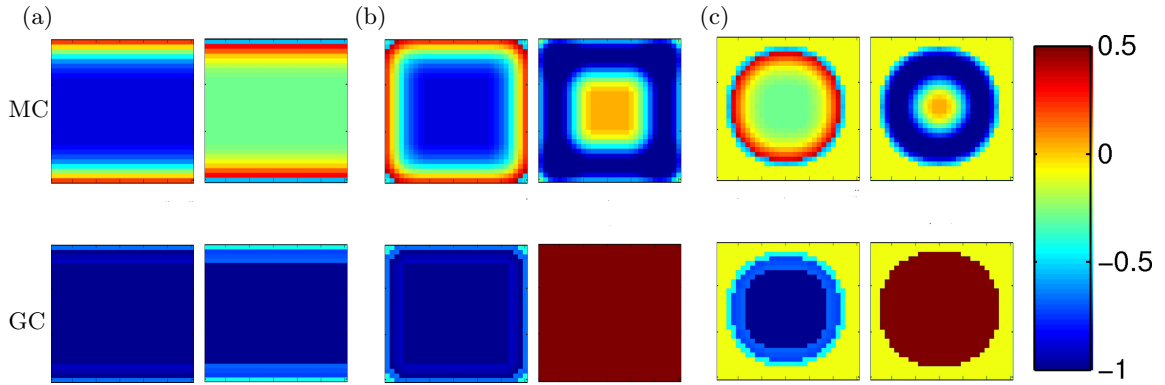


Figure 8.1: *Traveling waves in the OB network for different boundary shapes and homogeneous input.*

In Figure 8.1 it can be observed that the shape of the boundary influence the structure of the waves emerging in the OB, but the shape is constant as the shape of the boundary does not change. From left to right we have:

- (a) Quadratic simulation area with periodic boundary conditions in  $x$ -direction and no connections at the upper and the lower boundary. This results in waves moving from the top and the bottom to the middle of the simulation area.
- (b) Quadratic simulation area with no connections at all boundaries. The waves travel now from all four boundaries to the center of the network.
- (c) Circular simulation area with no connections at the boundary. As in case (b) the wave move from the boundary to the center of the network.

It is well known that lateral boundaries can effect traveling wave dynamics for example in binary fluid convection [3]. Boundaries where no connections occur in one direction are disruptions in a network where the rest of its structure is homogeneous. And these disruptions are starting points of waves. The waves occurring in the model network of the OB are actually waves of inhibition, i.e. the emerge first on the GC array and the

inhibition on the MC array is followed by a excitation wave there. We will come to this point again later.

## 8.2 INFLUENCE OF NETWORK PARAMETERS

To be not dependent on the boundary conditions, we search for another way to investigate the existence of traveling waves. Suitable initial conditions, i.e. a spiking history of a wave on the GC array followed by a wave on the MC array, result in oscillatory traveling waves, too. To investigate this behavior in detail, we investigate a chain of mitral and granule cells and the waves moving along this chain. In Figure 8.2 the first 25 plotted time steps show the initialization after which oscillatory waves occur even for periodic boundary conditions at the chain ends. The left part of Figure 8.2 shows the direct simulation of the waves in a chain of 400 MCs and 400 GCs with an external input of  $h_{ext}^i = 0.5$  for  $i = 1, \dots, n_m$ . We have  $r_{exc} = 20$ ,  $r_{inh} = 100$ ,  $J_{exc} = 0.4$  and  $J_{inh} = 0.01$ .

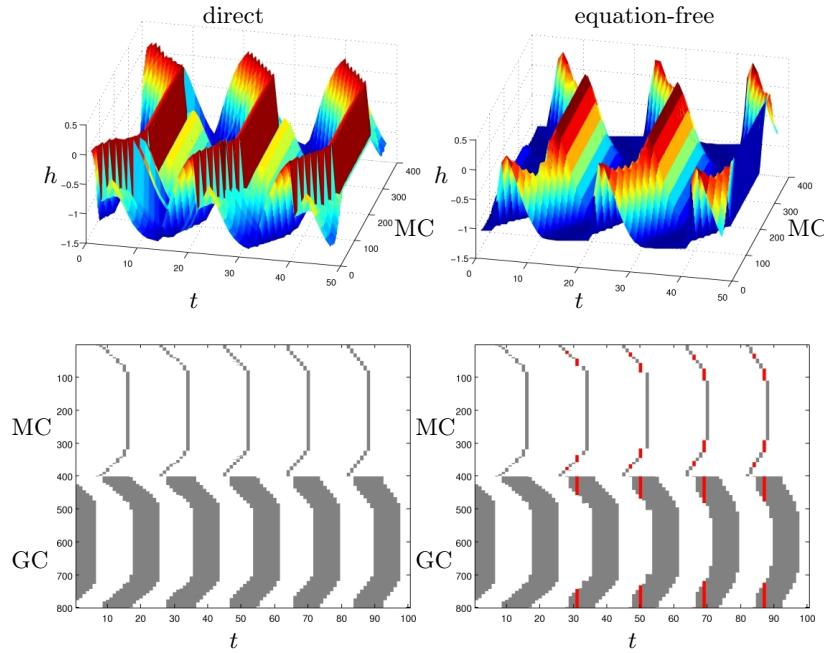


Figure 8.2: *Traveling waves in a cell chain of 400 MCs and 400 GCs. Left: direct simulation, right: equation-free simulation using template fitting. Upper row: membrane potential of the MCs, lower row: spiking activity of the network. The red entries in the spiking matrix indicate projection steps in the equation-free simulation.*

### 8.2.1 EQUATION-FREE INVESTIGATION OF TRAVELING WAVES

As before we want to speed up the simulations by using equation-free techniques. In the context of traveling waves we combine this approach with template fitting ideas as described in Section 4.7. That means the coarse variable is the template fitting variable  $c$ . We measure  $c$  in the MC chain from the spiking matrix after simulating a few time steps. This is the restricting process  $r$  here. Then we project the wave using the measured  $c$  and the old position of the wave. Then one has to lift the system – this is done by a projection of the spiking activity, i.e. one sets  $S_i = 1$  for MCs and GCs where the traveling wave is projected to be. The results of the equation-free simulations can be found in the right part of Figure 8.2 where the projection steps are indicated by red entries in the spiking profile.

Figure 8.2 shows that the waves occurring in the OB network are actually inhibition waves, i.e. we first have a wave on the GC chain, which then inhibits the MCs and after this inhibition wave the actual excitation wave is able to propagate across the network. This behavior is well known for example in epidemiology. In a model of a Hantavirus epidemics [2] a situation was observed, where first a wave of susceptible species has to emerge before a infection can occur. In the same manner the MCs are brought in a feasible state that a wave can emerge due to the inhibition by GCs in the OB.

We can achieve a speed up between the equation-free and the direct computation depending on the length of the simulation time: for  $100ms$  simulation time we get a speed up of 7%, for  $1000ms$  we have a 10% speed up and for  $10,000ms$  the equation-free computations are 21% faster than the direct simulations.

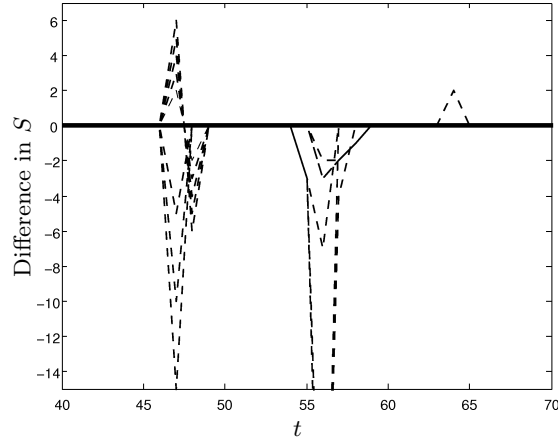


Figure 8.3: *Convergence of equation-free simulations of traveling waves in a cell chain of 400 MCs and 400 GCs. Difference in spiking matrix for disturbed states (dashed lines).*

In Figure 8.3 we investigate as before how disturbances in the spiking matrix influence the equation-free simulations. It turns out that the disturbed system (dashed lines) con-

verges quickly to the undisturbed state (solid line). We show the mean difference in the spiking rate. The oscillatory occurrence of an error is due to the oscillatory presence of the traveling waves.

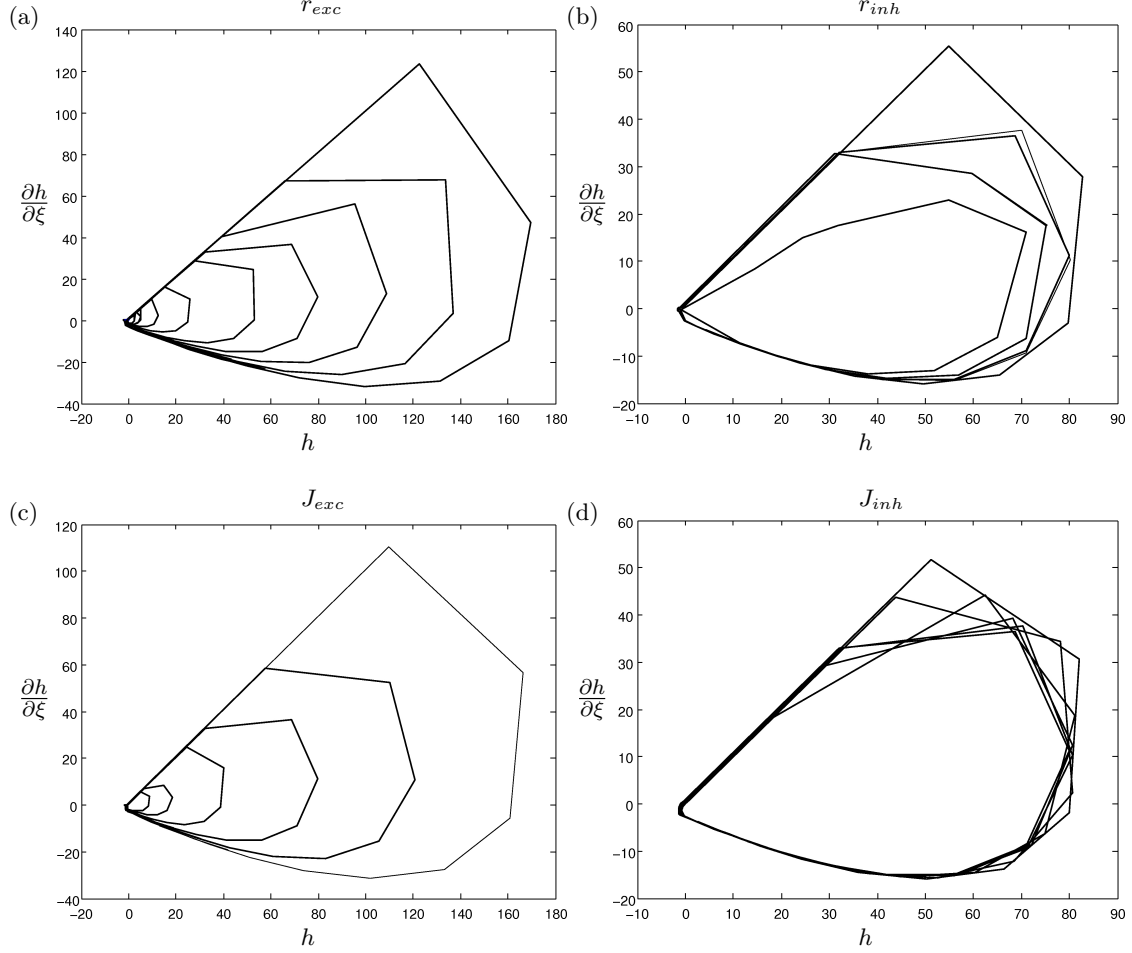


Figure 8.4: *Influence of the connectivity parameters on the amplitude of the traveling wave in the OB network. (a)  $r_{exc}=100, 80, 60, 40, 20, 10, 5, 3, 2, 1$ , (b)  $r_{inh}=200, 150, 100, 10, 1$ , (c)  $J_{exc}=0.8, 0.6, 0.4, 0.2, 0.1, 0.05$ ,  $J_{inh}=0.1, 0.81, 0.04, 0.02, 0.01$  (from outer orbits to the middle).*

In previous investigations of the olfactory bulb network dynamics we saw that the network connectivity parameters, especially  $r_{exc}$ , have an influence on the behavior of the network. It is again the case, that  $r_{exc}$  has the largest influence on the network dynamics in the case of traveling waves. For very small parameter values the connections between the cells are too weak. That means the cell activity of a single cell is not really influenced by the network. For very strong connections and very wide ranging inhibition, GC activity

damps the activities of the MCs and, therefore, no waves can occur on this level.

We investigate two properties of the waves: their amplitude and their velocity. In order to investigate the size of the amplitude we plot the homoclinic orbits, which are passed for one traveling wave, in Figure 8.4. Note the larger the radius of the orbit, the larger is the amplitude of the traveling wave. It turns out that the amount of excitation described by  $r_{exc}$  and  $J_{exc}$  has more influence on the amplitude than the inhibition described by  $r_{inh}$  and  $J_{inh}$ .

A different situation occurs for the traveling wave velocity. Figure 8.5 shows this: As  $r_{exc}$  grows, the traveling wave velocity of the emerging wave grows much more then for changing  $J_{inh}$  and  $J_{exc}$ . The value of  $r_{inh}$  has no influence on the traveling wave velocity at all. This leads to the following statement.

**STATEMENT 8.2.1 (TRAVELING WAVES IN THE OB)** *In the OB network model occur traveling waves due to boundary conditions or suitable initial settings. The amplitude of them depends on  $r_{exc}$  and  $J_{exc}$ . Their velocity depends mainly on  $r_{exc}$ .*

## 8.2.2 BIOLOGICAL INTERPRETATION

**T**o our knowledge traveling waves in the olfactory bulb are found in experiments only in zebrafish [44] not in mammals. There are two main differences between zebrafish and mammals. The first one is due to experimental settings: imaging experiments with zebrafish are done without anesthesia, whereas in imaging experiments of rats or mice the animals are anesthetized (see, e.g. [99]). As second difference comes because of anatomical differences between the OB of fish and mammals: The mammalian MCs have very long dendrites, with a length up to one third of the size of the OB [107]. The range of the dendrites of the fish MCs is not that long, i.e. unidendritic MCs occur with a single primary dendrite with one or more tufts and a short range compared to the size on the bulb [46].

Anesthesia damps neuron activity, it is therefore possible, that the network in anesthetized mammals is in a state, where no waves occur since the connections are too weak to influence the activity of a single cell, i.e. the amplitude of the waves may get smaller, which is the case for small values of  $J_{exc}$ . This can be one reason why waves are not depicted in mammals. Experiments with anesthetized fish could answer the question whether anesthesia plays a role in the emerging of traveling waves.

The influence of  $r_{exc}$  to the traveling wave velocity gives an other explanation for the presents of traveling waves in zebrafish with regard to its physiological properties. Since the connections are not as long as in mammals, traveling waves, if they emerge, may be slow enough to be detected in imaging experiments. I.e. they are too fast to be detected in mammals due to the wide range connections there.



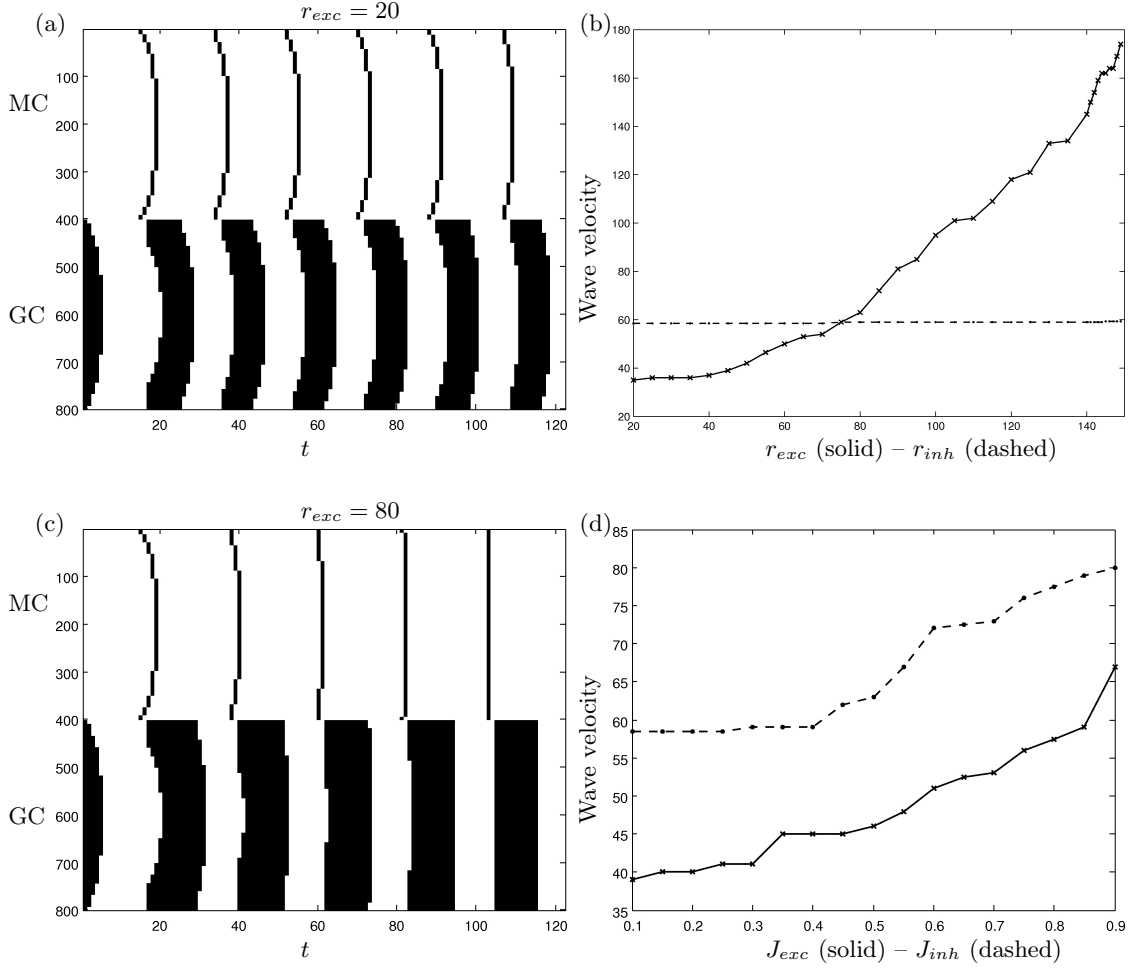


Figure 8.5: *Influence of the connectivity parameters on the traveling wave velocity in the OB network.*

The influence of the boundaries to the emerging of traveling waves described in Section 8.1 can give an explanation, why the waves detected in experiments are odor independent. The olfactory bulb has a boundary at its rostral end. Hence, it is possible that the waves emerge there relatively odor independent.

### 8.3 CONCLUSIONS OF CHAPTER 8: TRAVELING WAVES

As imaging experiment in zebrafish show, there are experimental settings where traveling waves emerge in the OB. These waves are nearly odor independent. We show that wave solutions in our model depend on the shape of the boundary of the network but are constant when the shape of the boundary does not change. Therefore, the boundary of the olfactory

bulb at its rostral end may be responsible for the wave.

Using equation-free methods for traveling waves, we are able to give an explanation why the waves are only seen in zebrafish not in mammals. As the radius of excitation  $r_{exc}$  grows, the propagation velocity of the traveling waves grows, too. It is possible in the case of very wide interactions between mitral and granule cells, as they occur in mammals, that the traveling-wave-like structures move too fast to be detected.

On the other hand are the experiments with fish done without anesthesia and damped synaptic strength reduces the amplitude of the traveling waves. This can give another explanation why waves are not seen in mammals, which are always anesthetized during imaging experiments at the olfactory bulb. Experiments with anesthetized fish could answer the question whether anesthesia plays a role in the emergence of traveling waves.

## Chapter 9

# CONCLUSIONS AND OUTLOOK

*But all endings are also beginnings.*

MITCH ALBOM

We introduced a mathematical description for the dynamical activity of the olfactory bulb (OB) neuron network in this work. We adapted the Spike Response model, an integrate-and-fire model for point neurons. This leads to a network model with uniformly arranged point neurons, representing mitral and granule cells, where the signal traveling times are incorporated via delays.

For cases where point neurons are not sufficient, we stated a finite-element based simulation method. Here, it is possible to include the spatial expansion of the considered neurons in the simulations. The dynamics is modeled by the Hodgkin-Huxley equations. We developed a-posteriori error estimators for passive signal propagation. Based on these estimators we adjusted adaptive grid and time-step control techniques for efficient and accurate simulations of neuron dynamics.

Numerical tests showed that these methods are effective with regard to saving computation time without loosing accuracy compared to uniform computations.

In order to simulate and analyze the network dynamics of the OB network model with regard to changing connection parameters of the network it turned out, that equation-free simulation and analysis methods can be successfully applied. The motivation for using these methods came from the observation that the network dynamics of the OB can be described in a low dimensional space. We adapted the equation-free simulation techniques to the needs of the investigations of the OB dynamics. Namely, we described equation-free Newton's method, parameter studies and methods for traveling waves. This allow to combine the equation-free approach with numerical bifurcation analysis methods. Furthermore, we interpreted the equation-free time-stepping scheme in the context of classical one-step methods. This enabled us to use standard techniques from the numerical analysis

to prove a convergence theorem for this method.

We combined these theoretical results in the second part of this thesis to perform numerical analysis of the dynamics of, first, single mitral cells and, second, the OB network model. In the case of single mitral cells we saw that the time course of cell activity and the inhibitory synaptic input from the granule cells is crucial for the dynamics on the mitral cell's dendrites. This may lead to contrast enhancement in the OB network.

In the case of simulating the OB network model with point neurons, we showed in which cases the equation-free computation method can be used, and when it does not make sense to use it. Furthermore, we investigated the following biological questions: How is lateral inhibition, contrast enhancement and the ability to discriminate binary odor mixtures influenced by the connectivity parameters of the network, and under which conditions do traveling waves emerge in the network.

In lateral inhibition and contrast enhancement it turned out that the ability to perform these tasks depends strongly on the range of the connections, modeled by  $r_{exc}$ . For odor discrimination tasks we could reproduce experimental results. Furthermore, we investigated the long term dynamics of the OB network and saw that hysteresis effects occur here. These effects lead to a stabilization of the network output for small changes in the input. Finally, we investigated traveling waves: it turned out, that the amplitude of the traveling wave depends on the amount of granule cell excitation, modeled by  $r_{exc}$  and  $J_{exc}$ . This makes sense, since the waves emerging in the OB network model are actually waves of inhibition on the granule cell level, which are followed by excitation waves on the mitral cell level. The velocity of the traveling waves is determined mainly by the radius of excitation  $r_{exc}$ . This results gave two possible explanations why traveling waves are only seen experimentally in zebrafish and not in mammals: on one hand, zebrafish are not anesthetized during the experiments. Anesthesia reduces the synaptic strength, i.e. this may prevent that traveling waves are seen experimentally in mammals. On the other hand, have the mitral cells of zebrafish a smaller range compared to the mitral cells of mammals. This could lead to slower waves, which are, therefore, detected in the experiments.

The presented model and the simulation results give rise to further interesting modeling, mathematical and biological questions. The OB network model does not include all mechanisms present in the OB. An interesting point could be to combine the MC-GC circuit with inhibition on the glomerula level. On one hand, one has to include periglomerular cells to the model for this task. On the other hand, the glomeruli themselves have to be modeled. To our knowledge not much data is available for the glomeruli activity. But as soon as experimental data is available, this task would be very interesting, and helpful to

get a complete picture of the OB dynamics.

For the simulations done in this work there was mostly constant network input used. Interesting effects could occur for input signals modeling the breath cycle of a animal, including sniffing and adaptation of the receptors. Our investigations of input modes varying in time with equation-free simulation techniques showed that simulation tools presented here can be used for this purpose.

A very interesting topic would be to combine the equation-free techniques and the adaptive computations presented in this work. One would, on one hand, have to deal with the special network structure in the OB, i.e.  $n$ -to- $n$  connections between mitral cell's and granule cell's dendrites. On the other hand, the evaluation of the coarse quantities has to be adapted. In networks with spicuous neurons not only the spiking activity has to be taken into account, but also the dendritic activity. Only this enables to compare simulation results to results from imaging experiments. Additionally, it would be interesting to model the synapses between the mitral and the granule cells explicitly when neurons with spatial expansion are considered.

**F**rom a mathematical point of view, there is one main question arising from the investigations of the traveling waves: is it possible to prove the existence of a traveling wave solution for the OB network model analytically? Due to delays in the dynamics of the network and not continuous spiking activities of the single neurons, this question is not expected to be very simple to answer.

**F**urthermore, the results of this work give rise to several biological questions that may be answered by new experiments. First, we saw hysteresis effects after relatively long periods of odor presentation. These effects, if they are actually present in nature, should be found in imaging experiments with relatively long input times, where the presented odors are changed slightly during the experiment. To our knowledge such experiments are not done yet.

Second, we saw that anesthesia and anatomy could both give explanations why traveling waves emerge only in zebrafish. Experiments with anesthetized fish could approve or exclude anesthesia as reason why traveling waves are not present in mammals.



# Appendix A

## LIST OF SYMBOLS & PARAMETERS

- GENERAL ABBREVIATIONS

OB	olfactory bulb
MC	mitral cells
GC	granule cells

- SPIKE RESPONSE MODEL

$n$	number of neurons in the network
$t, \Delta t$	simulation time, basic time-step
$S_i(t), S(t)$	spiking variable for neuron $i \in \{1, \dots, n\}$ , spiking matrix for the complete network
$\Delta_{ij}^{den}$	delay for signal propagation between cell $i$ and cell $j, i, j \in \{1, \dots, n\}$
$J = (J_{ij})$	synaptic strength matrix
$h_i$	membrane potential of neuron $i \in \{1, \dots, n\}$
$h_i^{syn}$	synaptic contribution to membrane potential of neuron $i \in \{1, \dots, n\}$
$h_i^{s-inh}$	self-inhibitory contribution to membrane potential of neuron $i \in \{1, \dots, n\}$
$\Delta_i^{s-inh}$	delay for activation of self-inhibition of neuron $i \in \{1, \dots, n\}$
$h_i^{ext}$	external input of neuron $i \in \{1, \dots, n\}$
$h_i^{ref}$	refractory part to membrane potential of neuron $i \in \{1, \dots, n\}$

- HODGKIN-HUXLEY MODEL

$\Omega$	area of neuron
$\partial\Omega, \Gamma_D, \Gamma_N$	boundary of $\Omega$ , Dirichlet boundary points, Neuman boundary points
$c_{Na}$	sodium concentration
$c_K$	potassium concentration
$c_{Na}$	leakage current
$C_M$	capacity of neuron membrane
$R_i$	intercellular resistivity
$R_M$	membrane resistivity

- OLFACTORY BULB NETWORK MODEL

$n_m$	number of MCs in the network
$n_g$	number of GCs in the network
$r_{exc}$	radius of excitation, i.e. length of secondary dendrites of MCs
$r_{inh}$	inhibitory radius, i.e. conductivity of the MC's secondary dendrites
$J_{exc}$	strength of excitatory synapses
$J_{inh}$	strength of inhibitory synapses

- ADAPTIVE GRID CONTROL

$H^n(\Omega),$ $H_0^1(\Omega),$ $L^2(\Omega)$	usual Sobolev, Lesbesguespaces
$S_n$	finite-dimensional subspace of $H_0^1(\Omega)$
$I_n$	nodal interpolation in $S_n$
$v_n$	space discrete membrane potential
$v_n^k$	fully discrete membrane potential
$v_n^\tau$	piecewise affine interpolation of $v_n^k$
$e^s$	spatial error
$E_n^t$	temporal error
$TOL$	user tolerance for grid control



- EQUATION-FREE SIMULATIONS

$u$	fine, microscopic variable, $u \in \mathbb{R}^m$ , $m \gg 1$
$U$	coarse. macroscopic variable, $U \in \mathbb{R}^M$ , $m \gg M$
$\Phi^f, \Phi^c$	operation functions of fine/coarse time-stepper
$l$	lifting routine
$r$	restricting routine

- SIMULATIONS OF THE OB NETWORK

$\Delta_{ce}$	measure of contrast enhancement properties
$c_1, c_2$	input strength for binary odor mixtures
$t_d$	discrimination time
$\delta_d$	threshold for discrimination
$\Delta_s$	spiking rate difference

## A.1 PARAMETERS USED IN ADAPTIVE SIMULATIONS

- ADAPTIVE SIMULATIONS

Name	Meaning	Value
$\tau_{fine}$	number of refined elements	30%
$\tau_{coarse}$	number of coarsened elements	30%
$\max_{level}$	maximum level of grid refinement	7 – 9
$\min_{level}$	minimal level of grid refinement	1
$dt^{min}$	minimal stepsize	0.1ms
$dt^{max}$	maximal stepsize	2ms

## A.2 PARAMETERS USED IN EQUATION-FREE SIMULATIONS

- GENERAL QUANTITIES

$n_m$	number of MCs in the network	900
$n_g$	number of GCs in the network	8100

- SPIKE RESPONSE MODEL

Name	Meaning	Value	Ref.
$\theta$	firing threshold	0.12	[41]
$d_{ij}$	euclidean distance between neuron $i$ and $j$	in $\mu m$	<i>comp.</i>
$d_{MC}$	distance between two neighboring MCs	$10 - 15\mu m$	
$\Delta_{ij}^{syn}$	delay of synapses	2ms	[64]
$v_{den}$	velocity of signal propagation in dendrites	$0.3m/s$	[122]
$\Delta_{ij}^{den}$	$= \frac{d_{ij}}{v_{den}} + \Delta_{ij}^{syn}$		<i>comp.</i>
$\Delta_i^{s-inh}$	delay for activation of self-inhibition	0	[41]
$\tau_{ref_m}$	refractory time of MCs	$20ms$	
$\tau_{ref_g}$	refractory time of GCs	$20ms$	
$R$	refractoriness of the MCs & GCs	10	[41]
$\tau_\eta$	constant in rate function	6	[41]
$\tau_\epsilon$	constant in rate function	2	[41]
$\eta_{inh}$	constant in rate function	-2	[41]

# List of Figures

1.1	Inhibition causes contrast enhancement. . . . .	2
2.1	Nerves of septum of the human nose and olfactory bulb. . . . .	8
2.2	Layer structure of the OB network. . . . .	10
2.3	Mitral cell and granule cell morphology. . . . .	12
2.4	Olfactory bulb: main building blocks and activity. . . . .	13
3.1	Geometry of the neuron with synaptic in- and output. . . . .	25
3.2	Hierarchical grid refinement. . . . .	27
4.1	The coarse time-stepper. . . . .	43
4.2	Convergence to the inertial manifold. . . . .	48
4.3	Traveling wave and homoclinic orbit. . . . .	52
4.4	Hysteresis. . . . .	57
4.5	(Pseudo-arclength) continuation. . . . .	60
5.1	Dynamics of a mitral cell computed with adaptive grid control. . . . .	64
5.2	Performance of error estimator in space. . . . .	65
5.3	Computation time for uniform and adaptive simulations. . . . .	66
5.4	Computation time for uniform and adaptive time step size control. . . . .	67
5.5	Synapses inhibit the signal processing. . . . .	68
5.6	Time course of firing and synaptic activity. . . . .	69
6.1	Equation-free simulation of OB modes. . . . .	73
6.2	Disturbed equation-free simulation: convergence to slow manifold. . . . .	74
6.3	Equation-free simulation with several ensembles. . . . .	75
6.4	Limits of the equation-free simulation technique. . . . .	76
6.5	Lateral inhibition. . . . .	78
6.6	Equation-free investigations of contrast enhancement – introduction. . . . .	79
6.7	Equation-free investigations of contrast enhancement – result. . . . .	81
7.1	Odor discrimination for two square inputs. . . . .	85

7.2	Odor discrimination for amyl acetate and ethyl butyrate. . . . .	87
7.3	Behavior of $t_d$ depending on different parameters. . . . .	88
7.4	Equation-free time-stepping for spiking rate difference. . . . .	90
7.5	Hysteresis and adaptation effect in a system with prehistory. . . . .	91
8.1	Traveling waves in the OB network for different boundary shapes. . . . .	96
8.2	Traveling waves in a cell chain . . . . .	97
8.3	Convergence of equation-free simulations of traveling waves. . . . .	98
8.4	Influence of the parameters on the amplitude of traveling waves. . . . .	99
8.5	Influence of connectivity parameters on traveling wave velocity. . . . .	101

# Bibliography

- [1] Abraham, N.M., Sprors, H., Carleton, A., Margie, T.W., Kuner, T., Schäfer, A. Maintaining Accuracy at the Expense of Speed: Stimulus Similarity Defines Odor Discrimination Time in Mice. *Neuron*, 34:301–315, 2002.
- [2] Abramson, G., Kenkre, V.M. Traveling Waves of Infection in the Hantavirus Epidemics. *Bulletin of Math. Biology*, 65:519–534, 2003.
- [3] Aegerter, C.M., Surko, C.M. Effects of Lateral Boundaries on Traveling-Wave Dynamics in Binary Fluid Convection. *Phys. Rev. E*, 63:046301:1–12, 2001.
- [4] Ainsworth, M., Oden, J.T. *A Posteriori Error Estimation in Finite Element Analysis*. Wiley-Interscience, 2000.
- [5] Alt, H.W. *Lineare Funktionalanalysis*. Springer, 1990.
- [6] Arevian, A.C, Kapoor, V. Urban, N.N. Activity-dependent Gating of Lateral Inhibition in the Mouse Olfactory Bulb. *Nature Neuroscience*, 11:80–87, 2007.
- [7] Aungst, J.L, Heyward, P.M., Puche, A.C., Karnup, S.V., Hayer, A., Szabo, G., Shipley, M.T. Centre-Surround Inhibition Among Olfactory Bulb Glomeruli. *Nature*, 426:623–629, 2003.
- [8] Baier, H., Korsching, S. Olfactory Glomeruli in the Zebrafish Form an Invariant Pattern and Are Identifiable Across Animals. *J. of Neuroscience*, 14:219–230, 1994.
- [9] Bangerth, W., Rannacher, R. *Adaptive Finite Element Methods for Differential Equations*. Birkhäuser, 2006.
- [10] Barak O., Tsodyks M. Persistent Activity in Neural Networks with Dynamic Synapses. *PLoS Computational Biology*, 3:323–332, 2007.
- [11] Bastian, P., Blatt, M., Dedner, A. , Engwer C., Klöfkorn, R., Kornhuber, R., Ohlberger, M., Sander, O. A Generic Grid Interface for Parallel and Adaptive Scientific Computing. Part II: implementation and tests in DUNE. *Computing, Online First*, 2008.

- [12] Bastian, P., Blatt, M., Dedner, A., Engwer C., Klöfkorn, R., Ohlberger, M., Sander, O. A Generic Grid Interface for Parallel and Adaptive Scientific Computing. Part I: Abstract Framework . *Computing, Online First*, 2008.
- [13] Bastian, P., Droske M., Engwer C., Klöfkorn, R., Neubauer T., Ohlberger, M., Rumpf, M. Towards a Unified Framework for Scientific Computing. *Proc. of the 15th International Conference on Domain Decomposition Methods*, 2004.
- [14] Bastian, P., Lang, S. Accurate and Efficient Numerical Methods for Branched Nerve Equations. *unpublished*, 2006.
- [15] Bastian, P., Wieners, C. Multigrid Methods on Adaptivly Refined Grids. *Comp. in Science and Engineering*, pages 50–60, 2006.
- [16] Bathellier, B., Buhl, D.L., Accolla, R. and Carleton, A. Dynamic Ensemble Odor Coding in the Mammalian Olfactory Bulb: Sensory Information at Different Timescales. *Neuron*, 57:586–598, 2008.
- [17] Bhalla, U.S., Bower, J.M. Exploring Parameter Space in Detailed Single Neuron Models: Simulations of the Mitral and Granule Cells of the Olfactory Bulb. *Journal of Neurophysiology*, 69(6):1948–1965, 1993.
- [18] Bhatnagar, P.L., Gross, E.P., and Krook, M. A Model for Collision Processes in Gases. I. Small Amplitude Processes in Charged and Neutral One-Component Systems. *Phys. Rev.*, 94:511–525, 1954.
- [19] Borisyuk, A., Ermentrout, G.B., Friedmann, A., and Terman, D. *Tutorials in Mathematical Bioscience I*. Springer, 2004.
- [20] Buck, L., Axel, R. A Novel Multigene Family may Encode Odorant Receptors: a Molecular Basis for Odor Recognition. *Cell*, 65:175–187, 1991.
- [21] Burlisch, R. and Stoer, J. Numerical Treatment of Ordinary Differential Equations by Extrapolation Methods. *Numer. Math.*, 8:1–13, 1966.
- [22] Byrd, C.A., Brunjes, P.C. Organization of the Olfactory System in the Adult Zebrafish: Historical, Immunohistochemical, and Quantitative Analysis. *J. Comparative Neurology*, 358:247–259, 1995.
- [23] Champneys, A. *Numerical Methods for Nonlinear Dynamics*. Lecturenotes, DCAMM Summerschool, Mathematical Tools for Complex Systems in Science and Technology, June 2007.
- [24] Chorin, A.J., Kast, A.P., Kupfermann, R. Optimal Prediction of Underresolved Dynamics. *Proc. Natl. Acad. Sci.*, 95:4094–4098, 1998.

- [25] Chueshov, I.D. *Introduction to the Theory of Infinite-Dimensional Dissipative Systems*. ACTA, 2002.
- [26] Cleland, T.A., Linster, C. Computation in the Olfactory System. *Chem. Senses*, 30:801–813, 2005.
- [27] Cleland, T.A., Sethupathy, P. Non-topographical Contrast Enhancement in the Olfactory Bulb. *BMCNeuroscience*, 7(7), 2006.
- [28] Davison, A.P., Feng, J., Brown, D. A Reduced Compartmental Model of the Mitral Cell for Use in Network Models of the Olfactory Bulb. *Brain Research Bulletin*, 51(5):393–399, 2000.
- [29] Davison, A.P., Feng, J., Brown, D. Spike Synchronization in a Biophysically-detailed Model of the Olfactory Bulb. *Neurocomputing*, 90:1921–1935, 2000.
- [30] Davison, A.P., Feng, J., Brown, D. Dendrodendritic Inhibition and Simulated Odor Responses in a Detailed Olfactory Bulb Network Model. *J. Neurophysiol.*, 90:1921–1935, 2003.
- [31] de Souza, F.M.S., Antunes, G. Biophysics of Olfaction. *Reg. Prog. Phys*, 79:451–491, 2007.
- [32] Destexhe, A., Meinen, Z.F., Sejnowski, T.J. Kinetic Models of Synaptic Transmission. In: *Methods in Neuronal Modeling: From Ions to Networks (2nd ed.)*, edited by C. Koch and I. Segev, MIT Press, 1998.
- [33] Deufelhard, P., Heroth, J., Maas, U. Towards Dynamic Dimension Reduction in Reactive Flow Problems. *Preprint, Konrad-Zuse-Zentrum für Informationstechnik Berlin*, SC 96-27:1, 1996.
- [34] Deuffhard, P., Heroth, J. Dynamic Dimension Reduction in ODE Models. *Preprint, Konrad-Zuse-Zentrum für Informationstechnik Berlin*, SC 96-29:1, 1996.
- [35] Dryer, L, Graziadei, P.P.C. Mitral Cell Dendrites: a Comparative Approach. *Anatomy and Embryology*, 189:91–106, 1994.
- [36] Edelstein-Keshet, L. *Mathematical Models in Biology*. SIAM, 2005.
- [37] Erdi, P., Gröbler, T., Barna, G., Kaski, K. Dynamics of the Olfactory Bulb: Bifurcations, Learning, and Memory. *Bio. Cybern.*, 69:57–66, 1993.
- [38] Eriksson, K, Estep, D., Hansbo, P., Johnson, C. *Computational Differential Equations*. Cambridge University Press, 1996.

- [39] Feng, J. Is the Integrate-and-Fire Model good enough? - a Review. *Neural Networks*, 4, 2001.
- [40] Firestein, S. How the Olfactory System Makes Sense of Scents. *Nature*, 413:211–218, 2001.
- [41] Fohlmeister, C., Gerstner, W., Ritz, R., van Hemmen, J.L. Spontaneous Excitations in the Visual Cortex: Stripes, Spirals, Rings, and Collective Bursts. *Neural Computation*, 7:905–914, 1995.
- [42] Foias, C., Jolly, M.S., Kevrekidis, I.G., Sell, G.R., Titi, E.S. On the Computation of Inertial Manifolds. *Physics Letters A*, 131(7,8):433–436, 1988.
- [43] Freeman, W.J. Olfaction: What’s New in the Nose. *J. Neurobio.*, 1978.
- [44] Friedrich, R.W., Habermann, C.J., Laurent, G. Multiplexing using Synchrony in the Zebrafish Olfactory Bulb. *Nature Neuroscience*, 7(8):862–871, 2004.
- [45] Friedrich, R.W., Laurent, G. Dynamic Optimization of Odor Representations by Slow Temporal Patterning of Mitral Cell Activity. *Science*, 291:889–894, 2001.
- [46] Fuller, C.L., Yettaw, H.K., Byrd, C.A. Mitral Cells in the Olfactory Bulb of Adult Zebrafish (*Danio rerio*): Morphology and Distribution. *J. Comparative Neurobio.*, 499:218–230, 2006.
- [47] Gear, C.W. *Numerical Initial Value Problems in Ordinary Differential Equations*. Prentice-Hall, Englewood Cliffs, NJ, 1971.
- [48] Gear, C.W., Kevrekidis, I.G. Projective Methods for Stiff Differential Equations: Problems with Gaps in their Eigenvalue Spectrum. *SIAM J. Sci. Comp.*, 24(04):1091–1106, 2003.
- [49] Gear, C.W., Kevrekidis, I.G., Theodoropoulos, C. “Coarse” Integration/Bifurcation Analysis via Microscopic Simulators: Micro-Galerkin Methods. *Comp. Chem. Eng.*, 26(02):941–963, 2002.
- [50] Gerstner, W. Time Structure of the Activity in Neural Network Models. *Phys. Rev. E*, 51:738–758, 1995.
- [51] Gerstner, W., van Hemmen, J.L. Associative Memory in a Network of ‘Spiking’ Neurons. *Network*, 3:139–164, 1992.
- [52] Gerstner, W., van Hemmen, J.L., Cowan, J.D. What matters in neuronal locking. *Neural Computation*, 8:1689–1712, 1996.
- [53] Gray, H. <http://en.wikipedia.org/wiki/Image:Gray858.png>. 2007.



- [54] Hamdi et al. Method of Lines. *Scholarpedia*, 2(7):2859, 2007.
- [55] Handwerker, H.O. *Allgemeine Sinnesphysiologie*. Neuro- und Sinnesphysiologie, Springer, 2006.
- [56] Hodgkin, A.L. and Huxley, A.F. A Quantitative Description of Membrane Current and its Application to Conduction and Excitation in Nerve. *Journal of Physiology*, 117:500–544, 1952.
- [57] Hummel, N. *Sorting as a Process of Self-organization, Application to the Axonal Pathfinding in the Olfactory System*. Diplomarbeit, University Heidelberg, 2007.
- [58] Hummer, G., Kevrekidis, I.G. Coarse Molecular Dynamics of a Peptide Fragment: Free Energy, Kinetics and Long Time Dynamics Computations. *J. Chem. Phys.*, 118(23):10762, 2002.
- [59] Jacob, T. Smell (Olfaction) - A tutorial on the sense of smell . <http://www.cf.ac.uk/biosi/staffinfo/jacob/teaching/sensory/olfact1.html>, 2008.
- [60] Keeler, J.D., Pichler, E.E., Ross, J. Noise in Neural Networks: Thresholds, Hysteresis, and Neuromodulation of Signal-to-noise. *PNAS*, 86:1712–1716, 1989.
- [61] Kevrekidis, I.G., Gear, C.W., Hummer, G. Equation-Free: The Computer-Aides Analysis of Complex Multiscale Systems. *AICHE Journal*, 50(07):1346–1355, 2004.
- [62] Kevrekidis, I.G., Gear, C.W., Hyman, J.M., Kevrekidis, P.G., Runborg O., Theodoropoulos, K. Equation-free coarse-grained multiscale computation: Enabling microscopic simulators to perform system-level tasks. *Comm. Math. Sciences*, 1:715–762, 2003.
- [63] Kuffler, S.W. Neurons in the Retina: Organization, Inhibition, and Excitation Problems. *Cold Spring Harbor Symp. Quant. Biol.*, 17:281–292, 1952.
- [64] Kuner, T. Personal correspondence. *Heidelberg*, 2007.
- [65] Kuznetsov, Y.A. *Elements Of Applied Bifurcation Theory*. Springer, 2004.
- [66] Laing, C.R. On the Application of “Equation-Free Modelling” to Neural Systems. *J. Comput. Neurosci.*, 20(01):5–23, 2006.
- [67] Lang, S. Simulation of Neurons on Network Grids with NeuroDUNE. *unpublished*, 2008.
- [68] Laurent, G., Stopfer, M., Friedrich, R.W., Rabinovich, M.I., Volkovskii, A., Abarbanel, H.D. Odor Encoding as an Active, Dynamical Process: Experiments, Computation, and Theory. *Ann. Rev. Neurosci.*, 24:263–297, 2001.

- [69] Li, Z., Hertz, J. Odor Recognition and Segmentation by a Model Olfactory Bulb and Cortex. *Comput. Neural Syst.*, 11:83–102, 2000.
- [70] Li, Z., Hopfield, J. Odor Recognition and Segmentation by a Model Olfactory Bulb and Cortex: A Model of the Olfactory Bulb and its Oscillatory Processing. *Biol. Cybern.*, 61:379–392, 1989.
- [71] Lowe, G. Inhibition of Backpropagating Action Potentials in Mitral Cell Secondary Dendrites. *J Neurophysiol*, 88:64–85, 2002.
- [72] Maas, U., Pope, S.B. Implementation of Simplified Chemical Kinetics Based on Intrinsic Low-Dimensional Manifolds. *24th Symposium on Combustion, The Combustion Institute*, pages 103–112, 1992.
- [73] Maas, U., Pope, S.B. Simplifying Chemical Kinetics: Intrinsic Low-Dimensional Manifolds in Composition Space. *Combustion and Flame*, 88:239–264, 1992.
- [74] Makeev, A.G, Kevrekidis, I.G. Equation-Free Multiscale Computations for a Lattice-Gas Model: Coarse-Grained Bifurcation Analysis of the NOCO Reaction on Pt(100). *Chem. Eng. Sci.*, 59:1733, 2004.
- [75] Makeev, A.G., Maroudas, D., and Kevrekidis, I.G. Coarse Stability and Bifurcation Analysis Using Stochastic Simulators: Kinetic Monte Carlo Examples. *J. Chem. Phys*, 116:10083, 2002.
- [76] Makeev, A.G., Maroudas, D., Panagiotopoulos, A.Z., and Kevrekidis, I.G. Coarse Bifurcation Analysis of Kinetic Monte Carlo Simulations: a Lattice Gas Model with Lateral Interactions. *J. Chem. Phys.*, 117(18):8229, 2002.
- [77] Mallet-Paret, J., Sell, G.R. Inertial Manifolds for Reaction Diffusion Equations in Higher Space Dimensions. *J. American Math. Society*, 1(4):805–866, 1988.
- [78] Moeller, J., Runborg, O., Kevrekidis, P.G., Lust, K., and Kevrekidis, I.G. Effective Equations for Discrete Systems: A Time Stepper Based Approach. *Int. J. Bif. and Chaos*, submitted (Can be found as physics/0307153 at arXiv.org), 2003.
- [79] Mori, K. Grouping of Odorant Receptors: Odor Maps in the Mammalian Olfactory Bulb. *Biochem. Soc. Trans.* , 31:134–136, 2003.
- [80] Mori, K., Nagao, H., Yoshihara, Y. The Olfactory Bulb: Coding and Processing of Odor Molecule Information. *Science*, 286:711–715, 1999.
- [81] Nagata, H. High Voltage Electron Microscopic Studies on Mitral, Tufted, and Granule Cells in the Mouse Olfactory Bulb. *J. Electron Microsc.*, 38(2):111–125, 1989.

- [82] Nagayama, S. Takahashi, Y.K, Yoshihara, Y., Mori, K. Mitral and Tufted Cells Differ in the Decoding Manner of Odor Maps in the Rat Olfactory Bulb. *J. Neurophysiol.*, 91:2532–2540, 2004.
- [83] Nagumo J., Arimoto S., and Yoshizawa S. An Active Pulse Transmission Line Simulating Nerve Axon. *Proc IRE*, 50:2061–2070, 1962.
- [84] Nicholls, J.G., Martin, A.R., Wallace, B.G. *From Neuron to Brain: A Cellular Approach to the Function of the Nervous System*. Palgrave Macmillan, 2001.
- [85] Pahle, J., Valova, I., Georgiev, G., Georgieva, N. Oscillatory Simulations of Mitral and Granule Cell Behavior in the Olfactory Bulb. *International Conference on Artificial Intelligence (IC-AI'2000), Las Vegas, Nevada, USA*, pages 483–489, 2000.
- [86] Panhuber, H., Laing, D.G., Willox, M.E., Eagleson, G.K., Pittman, E.A. The Distribution of the Size and Number of Mitral Cells in the Olfactory Bulb of the Rat. *J. Anat.*, 140(2):297–308, 1985.
- [87] Phillips R. *Crystals, Defects and Microstructures*. Cambridge University Press, 2001.
- [88] Pomerening, J.R., Sontag, E.D., Ferrell Jr., J.E. Building a Cell Cycle Oscillator: Hysteresis and Bistability in the Activation of Cdc2. *Nature Cell Biology*, 5:346–352, 2003.
- [89] Price, J.L., Powell, T.P.S. The Mitral and Short Axon Cells of the Olfactory Bulb. *J. Cell. Sci.*, 7:631–651, 1970.
- [90] Price, J.L., Powell, T.P.S. The Morphology of the Granule Cells of the Olfactory Bulb. *J. Cell. Sci.*, 7:91–123, 1970.
- [91] Price, J.L., Powell, T.P.S. The Synaptology of the Granule Cells of the Olfactory Bulb. *J. Cell. Sci.*, 7:125–155, 1970.
- [92] Rannacher, R. *Numerische Mathematik 2, Numerik partieller Differentialgleichungen*. Lecturenote, University of Heidelberg, 2006.
- [93] Rannacher, R. *Numerische Mathematik 1, Numerik gewöhnlicher Differentialgleichungen*. Lecturenote, University of Heidelberg, 2007.
- [94] Reidl, J., Borowski, P., Sensse, A., Starke, J., Zapotocky, M., and Eiswirth, M. Model of Ca Oscillations Due to Negative Feedback in Olfactory cilia. *Biophys J*, 90:1147–1155, 2006.
- [95] Reidl, J., Omer-Backlash, D.B., Grinvald, A., Starke, J., and Spors, H. Independent Component Analysis Identifies Functionally Related Neuronal Populations in High Resolution Imaging. *NeuroImage*, 34(1):94–108, 2007.

- [96] Rico-Martinez, R., Gear, C.W., and Kevrekidis, I.G. Coarse Projective KMC Integration: Forward/Reverse Initial and Boundary Value Problems. *J. Comp. Phys.*, 196:474, 2004.
- [97] Robinson, J.C. Inertial Manifolds and the Cone Condition. *Dyn. Systems and Appl.*, 2:311–330, 1993.
- [98] Rowley, C.W., Marsden, J.E. Reconstruction Equations and the Karhunen-Loeve Expansion for Systems with Symmetry. *Physica D*, 142:1–19, 2000.
- [99] Rubin, B.D., Katz, L.C. Optical Imaging of Odorant Representations in the Mammalian Olfactory Bulb. *Neuron*, 23:499–511, 1999.
- [100] Runborg, O., Theodoropoulos, C., Kevrekidis, I.G. Effective Bifurcation Analysis: a Time-Stepper-Based Approach. *Nonlinearity*, 15:491–511, 2002.
- [101] Sachse, S., Galizia, C.G. Role of Inhibition for Temporal and Spatial Odor Representation in Olfactory Output Neurons: A Calcium Imaging Study. *J Neurophysiol*, 87:1106–1117, 2002.
- [102] Schäfer, A.T., Margie, T.W. Spatiotemporal Representations in the Olfactory System. *TRENDS in Neurosciences*, 30(3):92–100, 2007.
- [103] Schoppa, N.E. and Westbrook, G.L. Glomerulus-Specific Synchronization of Mitral Cells in the Olfactory Bulb. *Neuron*, 21:639–651, 2001.
- [104] Schoppa, N.E., Kinzie, J.M., Sahara, Y., Segerson, T.P., Westbrook, G.L. Dendrodendritic Inhibition in the Olfactory Bulb is Driven by NMDA Receptors. *J. Neuroscience*, 18:6790–6802, 1998.
- [105] Shelley, M., McLaughlin, D. Coarse-grained Reduction and Analysis of a Network Model of Cortical Response: I. Drifting Grating Stimuli. *Journal of Computational Neuroscience*, 12(02):97–122, 2002.
- [106] Shepherd, G.M. *The Synaptic Organization of the Brain*. Oxford University Press, 2004.
- [107] Shipley, M.T., Ennis, M. Functional Organization of Olfactory System. *Journal of Neurobiology*, 30(1):123–176, 1996.
- [108] Siettos, C., Graham, M.D., and Kevrekidis, I.G. Coarse Brownian Dynamics for Nematic Liquid Crystals: Bifurcation, Projective Integration and Control via Stochastic Simulation. *J. Chem. Phys.*, 118(22):10149, 2003.
- [109] Starke, J. *Gewöhnliche Differentialgleichungen und Dynamische Systeme*. Lecture notes, University Heidelberg, 2004.

- [110] Sterrat, D.C. Locust Olfaction, Synchronous Oscillations in Excitatory and Inhibitory Groups of Spiking Neurons. *Wermter, S. et al. (Eds.), Emergent Neural Computational Architectures, Springer*, pages 270–284, 2001.
- [111] Stoer, J. and Bulirsch, R. *Numerische Mathematik 2*. Springer, 2000.
- [112] Sullivan, S.L., Dryer, L. Information Processing in Mammalian Olfactory System. *J. of Neurobiology*, 30(1):20–36, 1996.
- [113] Temann, R. *Infinite-Dimensional Dynamical Systems in Mechanics and Physics*. Springer, 1988.
- [114] The Mathworks, Inc. <http://www.mathworks.com/>. 2007.
- [115] Theodoropoulos, C., Qian, Y.-H., Kevrekidis, I.G. “Coarse” Stability and Bifurcation Analysis using Time-Steppers: A Reaction-Diffusion Example. *PNAS*, 97(18):9840–9843, 2000.
- [116] Theodoropoulos, C., Sankaranarayanan, K., Sundaresan, S., and Kevrekidis, I.G. Coarse Bifurcation Studies of Bubble Flow Lattice Boltzmann Simulations. *Chem. Eng. Sci.*, 59:2357, 2004.
- [117] Urban, N.N. Lateral Inhibition in the Olfactory Bulb and in Olfaction. *Physiology & Behavior*, 77:607–612, 2002.
- [118] Urban, N.N., Sackmann, B. Reciprocal Intraglomerular Excitation and Intra-Interglomerular Lateral Inhibition Between Mouse Olfactory Bulb Mitral Cells. *J. Physiol.*, 542:355–367, 2002.
- [119] Uschida, N., Mainen, Z.F. Speed and Accuracy of Olfactory Discrimination in the Rat. *Nature Neuroscience*, 6:1224–1229, 2003.
- [120] Valley, M. [http://en.wikipedia.org/wiki/Image:Mouse\\_MOB\\_three\\_color.jpg](http://en.wikipedia.org/wiki/Image:Mouse_MOB_three_color.jpg). 2006.
- [121] Verfürth, R. A posteriori error estimates for finite element discretizations of the heat equation. [citeseer.ist.psu.edu/604162.html](http://citeseer.ist.psu.edu/604162.html), 2003.
- [122] Xiong, W., Chen, W.R. Dynamic Gating of Spike Propagation in the Mitral Cell Lateral Dendrites. *Neuron*, 34(1):115–126, 2002.
- [123] Xu, K., Prendergast, K.H. Numerical Navier-Stokes Solutions from Gas Kinetic Theory. *J. Comp. Phys.*, 114:9–17, 1994.

- [124] Yokoi, M., Mori, K., Nakanishi, S. Refinement of Oodor Molecule Tuning by Dendrodendritic Synaptic Inhibition in the Olfactory Bulb. *Proc. Natl. Acad. Sci. USA*, 92:3371–3375, 1995.